Exploring Human Respiratory Information through a Design of a Wearable e-Health Monitoring System

Atena Roshan Fekr

Department of Electrical and Computer Engineering
McGill University, Montréal, Québec

A Thesis submitted to McGill University in partial fulfillment of the requirements for the degree of Doctor of Philosophy in Electrical Engineering

December 2015

ACKNOWLEDGEMENTS

First and foremost, I would like to express my sincere appreciation to Prof. Zeljko Zilic and Katarzyna Radecka for their commitment and worth advising. They shared the support and enthusiasm in my work and provided unlimited assistance throughout my research toward my Ph.D. degree.

I wish to especially thank Majid Janidarmian for his insightful and inspirational discussions and helps during my research. I would also like to thank my friends who have been a source of friendships as well as good advice and collaboration in Integrated Microsystems Laboratory (IML). Particular thanks go to Omid Sarbishei and Benjamin Nahill for their contributions and helps specifically for chapter 3 of my thesis. I am also grateful to Louis Ross, CEO of Motion Engine Company, for his support, encouragement and being a great source of inspiration in getting the most out of sensors. I would like to acknowledge Prof. Ghyslaine McClure for her professional French translation of the abstract.

Lastly, I would like to thank my family for all their love and encouragement. For my parents who raised me with a love of science and supported me in all my pursuits. And most of all I would like express appreciation to my loving and supportive husband who spent sleepless nights with and helped me to keep things in perspective. Without your support and love, this would not have become true. Thank you.

ABSTRACT

The measurements of human respiration signal caused by the actions of the chest wall respiratory muscles can help predict health crises. As technology matures, there exists a large potential for effective techniques that can develop the capabilities of health care systems in diagnostics and treatment of respiratory disorders. One recent area of interest is applying wearable Micro-Electro-Mechanical Systems (MEMS) to detect small movements of the body that occur during expansion and contraction of the lungs in each respiration cycle. This thesis presents a newly developed experimental system via wearable sensing technology and wireless communication.

In this dissertation, we make use of accelerometer sensors to model the interior and posterior movements of the chest wall during breathing function at rest positions. These motions are analyzed in order to explore different respiratory parameters with high accuracy versus the medical references. To do so, first the problems of self-recalibration of multi-sensory systems as well as fault-tolerant multi-sensor data fusion are considered.

Next, an accelerometer-based approach is developed to accurately estimate the breathing signal, respiratory timing variables and the phase shift between chest wall compartments, which is used for paradoxical breathing detection. Since it is essential to determine the critical events caused by sudden rise or fall in per breath tidal volume of the people, a technique is provided to automatically find accurate threshold values according to each individual's breath characteristics. Moreover, we integrate the use of inertial sensors with machine learning techniques to model a wide range of human respiratory patterns for the goal of cloud-based recognition of respiratory problems. Novel approaches are discussed for extracting information-rich features from the respiration signal to improve the performance of the classifiers. Furthermore, a hierarchical tree model is proposed based on multiobjective Evolutionary Algorithm (EA) to optimize two performance metrics of classification, simultaneously.

Finally, an innovative biofeedback mechanism is introduced based on Dynamic Time Warping with a fast segmentation method to provide a real-time quantitative feedback during breathing therapy. So that, the proposed platform potentially lifts the people's motivation up towards treatment while precisely tracks their practice quality improvement at low cost.

Abrégé

La prédiction de crises respiratoires chez les patients peut être facilitée ou assistée par des mesures du mouvement des muscles respiratoires de la paroi thoracique. Avec les avancées technologiques, plusieurs nouvelles techniques de détection et d'analyse de signaux s'avèrent efficaces et offrent un bon potentiel d'aide au diagnostic des désordres respiratoires et au suivi de leur traitement. Une avenue intéressante est l'utilisation de microsystèmes électromécaniques (MEMS) non intrusifs et facilement portables par le sujet, qui permettent de détecter les mouvements d'expansion et de contraction de la cage thoracique et des muscles respiratoires durant chaque cycle respiratoire.

Cette thèse présente un nouveau système expérimental basé sur cette nouvelle technologie de détection par MEMS combinée au téléchargement des données à distance par télécommunication sans fil. La recherche utilise des capteurs d'accélération afin de modéliser les mouvements antérieurs et postérieurs de la région thoracique du sujet au repos. Ces signaux sont ensuite traités et analysés afin d'identifier avec haute précision les caractéristiques des paramètres respiratoires par rapport aux conditions médicales de référence. À cette fin la thèse traite d'abord des questions d'auto-calibration des systèmes de détection à canaux multiples ainsi que la fusion des données collectées par de tels systèmes.

Par la suite, l'auteure présente son approche basée sur la mesure des accélérations afin de caractériser avec précision le signal respiratoire en termes de variables temporelles et du déphasage entre les compartiments du thorax, dans le but de détecter des conditions respiratoires paradoxales. La détermination des événements respiratoires critiques causés par les fluctuations soudaines du volume respiratoire du sujet étant essentielle, une technique est proposée qui permet d'établir automatiquement les valeurs limites précises associées au profil respiratoire caractéristique de chaque individu testé. De plus, l'auteure a intégré des techniques d'apprentissage machine aux systèmes de détection afin de modéliser une large gamme de profils respiratoires humains. Cette base de données pourrait mener au développement d'un outil de reconnaissance de problèmes respiratoires en ligne associée à la technologie de stockage de données en nuage. La thèse discute d'approches nouvelles pour l'extraction des caractéristiques saillantes du signal respiratoire afin d'améliorer la performance des critères de classification retenus. Pour ce faire, l'auteure propose un modèle hiérarchique en arborescence basé sur l'Algorithme évolutionnaire polyvalent afin d'optimiser simultanément les indicateurs de performance par paire.

Enfin, la recherche utilise un système de biofeedback innovant basé sur la distorsion dynamique temporelle du signal par segmentation rapide et qui permet le feedback quantitatif en temps réel en cours de thérapie respiratoire. La plate-forme de détection et monitorage proposée dans cette recherche encourage la motivation des sujets au traitement et suit précisément l'amélioration de leur condition à faible coût.

CONTENTS

LIST OF FIGURES

LIST OF TABLES

LIST OF ACRONYMS

AB:	Abdomen
ADC:	Analogue to Digital Convertor
AHI:	Apnea-Hypopnea Index
ANN:	Artificial Neural Network
ARIB:	Association of Radio Industries and Business
BBT:	Buteyko Breathing Technique
BLE:	Bluetooth Low Energy
bpm:	breath per minute
CF:	Cystic Fibrosis
CGM:	Continuous Glucose Monitor
CLIC:	Closed-Loop Insulin Control
COPD:	Chronic Obstructive Pulmonary Disease
CSAS:	Central Sleep Apnea Syndrome
DTW:	Dynamic Time Warping
EA:	Evolutionary Algorithms
ECG:	Electrocardiogram
ECOC:	Error-Correcting Output Codes
EDR:	ECG-Derived Respiration
EEG:	Electroencephalogram
ETSI:	European Telecommunications Standards Institute
FCC:	Federal Communications Commission
FIR:	Finite Impulse Response
FNAR:	False Negative Alarm Rate
FPAR:	False Positive Alarm Rate
GA:	Genetic Algorithm
GERD:	Gastroesophageal Reflux Disease
HMM:	Hidden Markov Model
HRV:	Heart Rate Variability
IAR:	Ingenjörsfirman Anders Rundgren
IC:	Industry Canada
IDE:	Integrated Development Environment
IIR:	Infinite Impulse Response
IMU:	Inertial Measurement Units
LS:	Least Squares
MAE:	Mean Absolute Error
MI:	Myocardial Infarction

MSE:	Mean-Square-Error
NHLBI:	National Heart, Lung, and Blood Institute
NPA:	Negative Predictive Alarm
OEP:	Optoelectronic Plethysmography
OSAS:	Obstructive Sleep Apnea Syndrome
OVO:	One Versus One
PAA:	Piecewise Aggregate Approximation
PE:	Pulmonary Emphysema
PPA:	Positive Predictive Alarm
PPS:	Patient Personal Server
R&TTE:	Radio and telecommunications terminal equipment
RBF:	Radial Basis Function
RC:	Rib Cage
RF:	Radio frequency
RMB:	Respiration Monitor Belt
rpm:	respiration per minute
SAX:	Symbolic Aggregate approximation
SG:	Savitzky-Golay
SIDS:	Sudden Infant Dead Syndrome
SMD:	Surface-Mounted Device
SSE:	Sum of Square Error
SSP:	Secondary Spontaneous Pneumothorax
SVM:	Support Vector Machine
TEDS:	Transducer Electronic Data Sheets
TELEC:	Telecom Engineering Center
TV_{var}:	Tidal Volume variability
VCG:	Vectorcardiographic

Chapter 1

INTRODUCTION

This chapter includes an overview of the thesis, along with a description of the problem definition. A summary is also given on contributions that were brought forth into this thesis.

1.1 Research Problem and Scope

Recent technological advances in wearable sensors and wireless communications make it possible to design low-cost, intelligent, and lightweight monitoring system [1]. As technology matures, there exists a large potential for effective techniques, which can develop the capabilities of health care systems in order to improve diagnostics and monitoring while maximizing the individual's independence. The measurement of human respiratory signal is crucial in cyber-biological systems, since a disordered breathing pattern can be the first symptom of different physiological, mechanical, or psychological dysfunctions. Thus, a real-time monitoring of respiratory parameters such as inspiratory/expiratory time, total time of the respiratory cycle as well as respiration rate is an important diagnostic method in planning of medical care. The process of discerning valuable respiratory information from motion sensors data is a non-trivial task and is an on-going research area. Additionally, the current medical sensing system specifications require high accuracies, as well as tolerance to external noise and potential faults. There might be different methods and devices, which are able to partially satisfy these domains, however the following have to be taken in to account when dealing with medical applications.

- *Accuracy:* Concerns about the estimation accuracy is a considerable challenge to the development of respiration monitoring systems in e-health applications. The monitoring systems constructed based on sensory systems may suffer from large calibration shifts resulted from inherent deficiency or aging. Calibration, which is defined as the process of mapping raw sensor readings into corrected values can be used to compensate the systematic offset and gain. This can help to increase the accuracy in the single-sensor systems; however, fusion techniques are efficient approach, which combines data from multiple sensors to achieve more accurate readouts compared to single-sensor systems.
- *Fault-Tolerance:* It is essential for any medical systems to be able to continue operating properly in the event of the failure since the technology trends indicate that sensing has by far the highest fault rates [2]. The health applications are included in the life-critical system category, which failure or breakdown may result in death or serious injury to patients. To support this criterion, the platform should be able to first detect the fault, quickly, and then discard the impact of faulty sensors in the final result.
- *Multi-Functional:* The ability of performing different tasks with high accuracy and quality in a single platform gives more credit to a monitoring system and is stated as a principle of the design.
- *Computation Power and Storage Capacity:* Deployment of low-power and high-speed algorithms and architecture that are suitable and well-aligned with health care monitoring systems is critical. Buffer size, storage capacity and battery lifespan are some limitations of the on-board sensor data processing, especially when dealing with a large population and round-the-clock monitoring systems.
- *Convenience:* Generally, remote monitoring system brings more convenience to the patients with less frequent visits to the hospital for the therapy. However, it is worth noting that, making the integrated nodes low-weight, wireless, and low-power will guarantee the patients and physicians satisfactions. The sensor placement is also another factor, which has to be taken into account when designing a convenient system. For example, in polysomnogaphy, the electrodes are taped on the skin. Therefore, removing the adhesive bonding caused the skin tissue injury as shown in Figure 1-1 [3].

Figure 1-1: Skin tissue injury caused by electrodes with adhesive bonding [3][4]

- *Easy setup:* There is a growing recognition that simple setup with a user-friendly platform is important to achieve interoperability among e-health solutions. Indeed, easy setup allows the users to apply the device without the need of medical experts.
- *Cost:* Although remote monitoring systems are decreasing the expenses by reducing the use of emergency department and hospitalization, the cost of the system should also be considered. The affordable design of a portable breathing monitoring system makes it suitable to be used by individuals of different socioeconomic statuses.
- *Safety and Privacy:* The safety of e-health products must be addressed in a similar way as for medical devices especially when the system is designed for critical community such as infants, elderly people, pregnant and parturient women. The privacy concern is less while employing on-body sensors compared to ambient sensors such as cameras or microphones since the recorded data is not understandable to the general users.

Given the importance and the challenges of designing a real-time monitoring and detection system, this thesis will focus on proposing a wireless and low-power respiration monitoring system in which different critical respiratory information are extracted by means of MEMS sensors while providing a comprehensive analysis and evaluations based on the described design criteria. The motivations behind the design of such a system are described in the next section.

1.2 Motivations behind the Research

During the last years, many research areas have focused on sensor-based applications to better understand and meet people's needs and demands. Population ageing is widespread across the world and it is most advanced in the developed countries. A majority of older adults are challenged by chronic and acute illnesses which follow a rise in costs of health care [5]. Due to the fact that increasing health care and nursing costs place a tremendous stress on the society and the government, assistive smart technology that promotes independent living amongst elderly and individuals with cognitive impairment is a major motivating factor for sensor-based systems. The U.S. health care system reports a cost reduction of nearly $200 billion during the next 25 years if remote monitoring tools were utilized in congestive heart failure, diabetes, Chronic Obstructive Pulmonary Disease (COPD), and chronic wounds or skin ulcers [5]. It is estimated that, about 7% of the population of the developed countries suffers from COPD and it is a growing problem in developing countries. The COPD is a progressive lung disease that makes it difficult to breathe. An estimate of 3.7 million people live with COPD in UK, predicted to increase by one-third by 2030, costing £1.2 billion/year [6]. As stated by the National Pressure Ulcer Advisory Panel [7], one of the ulcer prevention methods is to reposition the patients at least every two hours. Because people such as nurses, caregivers or medical staffs are usually immersed in busy and often trivial duties, a position monitoring system would be a good solution to inform them about the patients' body positions. It also helps to increase their awareness of pressure ulcers without increasing their memory loads when a multitasking schedule is arranged for them.

In addition to elderly people, it is also required to monitor the babies at sleep for Sudden Infant Dead Syndrome (SIDS) prevention. SIDS is the unexpected, sudden death of a child under age 1. This syndrome continues to be the major reason of death for infants in developed countries [8]. To avoid SIDS, sleeping on the back has been suggested by the American Academy of Pediatrics in 1992. SIDS decreased dramatically in some countries where the "Back to Sleep" recommendation has been widely adopted, such as the U.S. and New Zealand [9]. Therefore, providing a monitoring system, which is able to transmit the respiration signal and body positions, is one of the main interests in this thesis. Furthermore, while monitoring the baby's respiration signal, one must avoid using wiring in such devices since not only the baby might play with the wiring which resulted in failure of the system, but also he has been exposed to the risk of choking [10].

One of the famous breathing disorders is sleep apnea characterized by pause in breathing or infrequent breathing during sleep [11]. There are three types of sleep apnea: obstructive, central, and mixed. Obstructive Sleep Apnea Syndrome (OSAS) is the most common form of cessation of breathing (apnea) which repeated by complete or partial blockage of the upper airway during sleep.

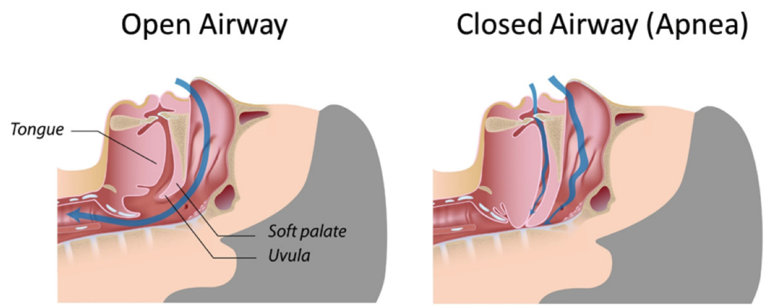

Figure 1-2: The apnea mechanism [12]

After about 10 seconds, the brain reacts with a loud gasp when the oxygen level gets too low. The apnea mechanism is shown in Figure 1-2. This pattern might occur 30 times per hour in the night without any recollection in the morning. It may also cause irregular heart rhythms due to the lack of oxygen to vital organs. According to the National Heart, Lung, and Blood Institute (NHLBI), about 18 million people in the U.S. have sleep apnea; however, most of them remain undiagnosed. Undiagnosed OSAS may increase the risk of developing cardiovascular diseases such as stroke and heart failure [13]. Central sleep apnea is a less common type of sleep apnea. In contrast with OSA, in central sleep apnea, breathing is disrupted regularly during sleep because of brain dysfunction. Although the airway is not close as happen in OSA, the brain doesn't have control on muscles to breathe [14]. OSA can be also diagnosed by analyzing the movements of the Rib Cage (RC) and Abdomen (AB) at the same time. Based on [15], OSA was characterized by paradoxical motion of the RC and AB in 91% of patients; however, in central sleep apnea there is a synchronic movement on the chest compartments. In patients with OSA, it is also believed that body position effects on apnea frequency. Sleeping on the side often results in significantly fewer apneas. However, as illustrated in Figure 1-3, based on the American Sleep Apnea Association, the positional therapy generally helps the patients with mild OSA and snoring [16]. The diagnosis of sleep apnea is based on the results of a formal sleep study using Polysomnography (PSG). PSG is a comprehensive recording of the biophysiological changes that occur during sleep. Although PSG remains as the de facto gold standard technique for diagnosis of respiration problems at sleep, it is complicated, expensive, time consuming and has to be conducted in a sleep laboratory [17]. Moreover, it is unavailable for everyone since there are very few hospitals which provide PSG test especially in rural areas [18]. Therefore, a need has arisen for an affordable real-time portable

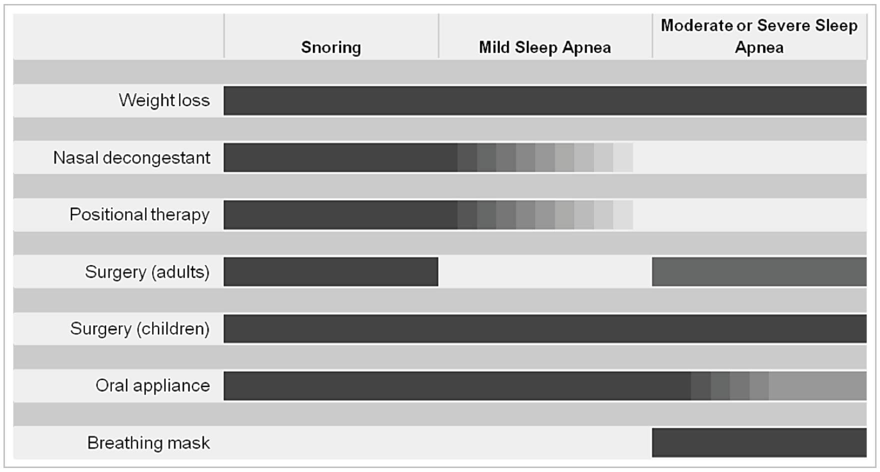

Figure 1-3: OSA Treatment Options [16]

system with acceptable accuracy and simple setup to be used as a diagnosis system for breathing disorders. Additionally, it will help people to change their sleep style according to the positional therapy in case of mild sleep apnea.

There are different types of breath disorders, which are characterized by different respiration patterns. These abnormal breathings are defined as follows:

- *Bradypnea* is regular in rhythm but slower than normal in rate. It may cause by OSA, which resulted in continuous disruption of breathing during sleep or from heart attack. It is an age-dependant breathing disorder and defines as follows [19]:

  Age 0–1 year < 30 breaths per minute (bpm)

  Age 1–3 years < 25 bpm

  Age 3–12 years < 20 bpm

  Age 12–50 years < 12 bpm

  Age 50 and up < 13 bpm

- *Tachypnea* is the condition of rapid breathing, with respiration rate higher than 20 respirations per minute (rpm) at rest. Tachypnea may occur due to physiological or pathological problems [20].
- *Cheyn-stokes* breathing pattern is determined by gradually increasing, then decreasing the lung volume with a period of apnea. Therefore, this type of breath disorder is characterized by a high oscillatory tidal volume. This type of respiration problem is seen in people with

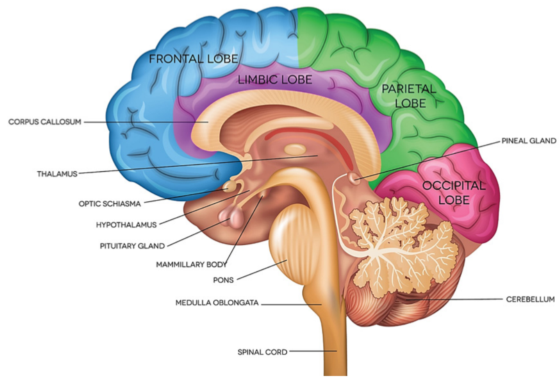

Figure 1-4: The Brainstem and Pons [25]

heart failure, strokes [21], traumatic brain injuries and brain tumors. People suffering from Central Sleep Apnea Syndrome (CSAS) have the same breathing pattern at sleep [22].

- *Kussmaul* that is defined as a rapid, deep and labored breathing type usually occurs in diabetic ketoacidosis. It is known as a type of hyperventilation, which reduces carbon dioxide in the blood due to the increased rate and depth of respiration [23].
- *Biot's* breathing is characterized by periods of rapid respirations followed by regular periods of apnea. There are different reasons which cause Biot's breathing, such as damage to the medulla oblongata by stroke or trauma, or pressure on the medulla due to uncal or tentorial herniation and prolonged opioid abuse [24].
- *Apneustic* respiration is an abnormal pattern of breathing characterized by a prolonged inspiration phase with each breath, followed by an expanded expiratory phase. It is usually caused by damage to the upper part of the pons, which is the uppermost section of the brain stem as depicted in Figure 1-4. According to [26] the pons can be considered as one of the "respiratory center" parts of the brain.
- *Sighing* breathing, known as hyperventilation syndrome, is characterized by high irregular breathing punctuated by deep periodic inspirations. Sighing breathing is observed in people suffering from anxiety with no apparent organic disease [27].

1.3 System Configuration and Thesis Contributions

The main contribution behind this research comes from the interest in using inertial wearable sensor technology to remotely estimate and monitor respiratory parameters of human beings precisely, as well as providing quantifying and qualifying biofeedback. For this purpose, first the system configuration is described in which different elements are selected based on the design criteria described in the previous section. Then, the major contributions that were made from this research are summarized. These contributions are organized by the presented topics within this thesis.

1.3.1 System Configuration

In the proposed hardware setup, we have integrated the use of wearable sensors, Bluetooth Low Energy (BLE) and cloud, which surpasses the traditional methods in accuracy, hardware cost, and convenience.

- Wearable sensors

In this thesis, the sensory node is referred as a complete system which is capable of sensing, measuring, transducing and delivering the data associated to the motion experienced by a given body part. Accelerometer sensors are among cheap, small and low-power nodes, which deliver rich information especially in movement analysis applications. Accelerometers produce voltage signals that are proportional to the experienced acceleration in different dimensions. In our system, we start with SensorTag shown in Figure 1.5 from Texas Instruments as our sensory node, which is the first Bluetooth Low Energy development kit on the market focusing on wireless sensor applications. In addition, its design has passed FCC (US), ETSI (Europe), IC (Canada) and ARIB (Japan) RF certifications [28]. It includes 6 low-power MEMS sensors (TMP006 infrared temperature, SHT21 digital humidity, T5400 barometric pressure, KXTJ9 tri-axis accelerometer, IMU-3000 tri-axis gyroscope and MAG3110 3D magnetic sensors). SensorTag is equipped with the Bluetooth Smart radio powered by a single CR2032 coin cell battery and Texas Instruments released its SDK for developers. The sensor and the battery supply are presented in Figure 1-5 (a). After SensorTag, the second sensory node is the OLP425 that is a stand-alone product with no additional hardware required [29]. It also includes Bluetooth Smart, temperature sensor, an ultra-low-power LIS3DH 3-axis accelerometer with 12-bit resolution and LEDs. Compared to SensorTag, OLP425 has become smaller in size (15×22 ×3mm) which makes it more convenient to be worn on body. The sensory node

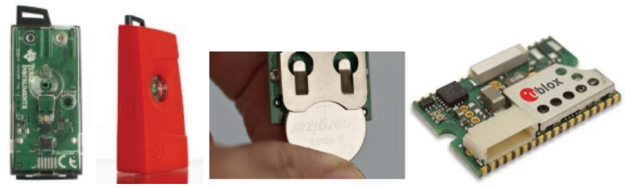

(a) (b)

Figure 1-5: (a) SensorTag [28], (b) ConnectBlue OLP425 [29]

is shown in Figure 1-5 (b). The module is using an internal Surface-Mounted Device (SMD) antenna with a range of 50m, which is included in FCC, IC, R&TTE and TELEC radio tests. The IDE from IAR Systems is used to configure the sampling rate of accelerometer sensor to suit our application. Both sensory nodes can communicate with any BLE enabled devices, for instance a smart phone or a tablet. In our specific configuration, sensor data are sent to the smartphone every 20ms (50Hz). The iOS software module on the iPhone is the modified version of the source code provided by connectBlue for developers. It is worth noting that, CC2540 USB dongle can also be used to record the data from computer and as a packet sniffer for analyzing the BLE protocol.

- Data Transmission

Bluetooth Low Energy or Bluetooth Smart, is a wireless technology designed for novel applications in the health care, fitness, security, and home entertainment industries which consumes only a fraction of the classic Bluetooth power [30]. The power-efficiency of Bluetooth Smart makes it ideal for round-the-clock monitoring applications in order to run off a tiny battery for long periods. BLE can form connection and data transfer in less than 3ms, letting an application to make a connection and then transfer authenticated data in few milliseconds. Therefore, in our application where a single data plays an important role either in diagnosis, treatment or emergency actions, applying a fast communication technique is essential. Bluetooth Smart technology provides strong encryption and authentication of data packets resulted from a full AES-128 encryption. In this thesis, we used the standard BLE services and device specific services such as device information, battery, LED, and accelerometer services.

- Cloud

Another issue for respiration monitoring systems is the limited on-board storage space and signal processing. Logging the data on the cloud makes it possible for the physicians to track their patients wherever they are with devices such as an iPhone, iPad or the web regardless of their proximity to the patients. Therefore, in the proposed system we use cloud database, which can offer significant advantages over traditional methods, including increased online accessibility, scalability, automatic failover and fast automated recovery from failures. In our configuration, the new raw data are sent to the cloud every 5 sec (250 samples) and then it can be manipulated and processed by the authorized people. There are different types of cloud backend such as Dropbox [31], Parse [32], and IBM Bluemix [33]. For the baseline prototype, we used Dropbox as a cloud option in the iOS application. Therefore, each subject has its own account with unique username and password. The users' data will be shared with authorized people, and finally the proposed algorithms are run on data receiving from Dropbox on either desktop computer, smartphone or tablet. It is worth mentioning that in case of network disconnection, the data is saved on the local data store of the intermediate interface, so any changes can be kept up-to-date while offline. In some cases, the online monitoring is also done in a cloud [34]. For example, recently, cloud providers like Amazon and Microsoft have attracted developers' attention by offering cloud-enabled machine learning as an easy way to integrate the power of machine learning into our applications. In this thesis, the proposed signal processing and algorithms are kept computationally unexpansive and are also implemented on cloud due to the flexible capacity

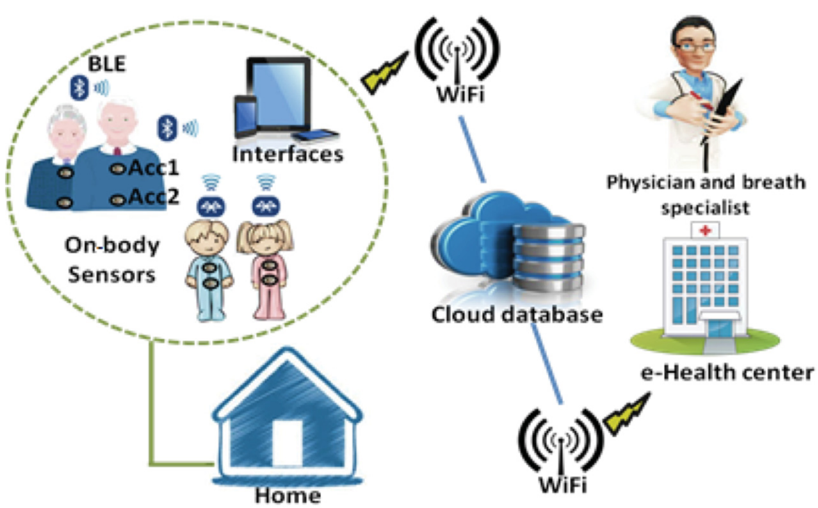

Figure 1-6: Overall view of the proposed cloud-based respiration

for both storage and computation. The overall view of the used configuration is summarized in Figure 1-6.

1.3.2 Thesis Contributions

The main contributions in this thesis are summarized as follows:

- A new data fusion algorithm is introduced for tolerating multiple faults in an arbitrary central multi-sensor system with measurable post-calibration statistical characteristics. The results are compared with previous work and show that it is suitable for real-time health care applications, where it is crucial to keep the overall precision and accuracy of the system high, and where sensor failures of even short duration could be fatal. This work has been addressed in [35]-[38]. Moreover, for the calibration of multi-sensory systems, a user may have no access to special calibration hardware or expert data analysis, therefore the need of automatic methods for jointly calibrating medical multi-sensor systems have been discussed in [39][40].
- A signal processing procedure is proposed by the author to extract the respiration signal, respiration rate, respiratory time parameters such as inspiration time, expiration time and total time of a breath cycle as well as the body angles during rest positions with a single accelerometer sensor mounted on the subjects' chest wall. Additionally, an accelerometer-based approach is developed to accurately estimate the phase shift between the chest wall compartments for paradoxical breathing diagnosis as well as Hi-Lo breathing test. The results are evaluated based on medical references including spirometer and respiration monitoring belt. This work has been addressed in [41][42][1].
- A new algorithm is proposed to calculate the Tidal Volume variability (TV_{var}) from modeling the anterior-posterior motions of the chest wall during breathing function. This has been addressed in [43][2]. This work is extended for including an emergency

[1] This publication was among finalists for **BIBE'14** Best Paper Awards
[2] This publication was awarded **Mobihealth'14** Best Paper Award

alarm detection system proposed in [44]. Since it is essential to detect the critical events caused by sudden rise or fall in per breath tidal volume of the patients, we provide a technique to automatically find the accurate threshold values based on each individual breath characteristics to be used in an emergency alert system.

- A hierarchical classification technique is proposed to distinguish among six different breathing models associated with normal and pathological respiration patterns. Different evaluations on performance parameters are reported in [41] considering both multi-class and binary classifications [45]. Further enhancement is achieved through applying two accelerometer sensors with a new informative feature set. These novel time domain features are computed based on individual set of tests and subjects in order to distinguish among nine different breathing patterns brought in [46]. The proposed classification method is extended to develop a multi-objective hierarchical classification architecture based on pareto-based multi-objective optimization methodology. The new configuration is built to improve two conflict objectives of multi-class classification: classification rate and classification rate for each class. The second objective is considered to guarantee a high precision in each class in real problems. This work has been addressed in [47].
- To complete our platform, we propose a new real-time biofeedback during "Breathing Therapy" as an advance way to assist people to learn the science of breath and help the patients successfully restore their health in a systematic way. This section of the thesis introduces the use of Dynamic Time Warping (DTW) with a new segmentation technique to provide the quality biofeedback, properly. Graphical signs are used to provide feedback on the quality of each breath taken in real-time. The performance of the system is evaluated based on five well-known yogic breathing patterns. This work has been addressed in [48].

As part of the work of this thesis, ethical approval was received from McGill University Ethics Committee. All the participants were informed about the experimental procedures before starting the trial sessions.

The rest of this thesis is organized as follows. Chapter 2 discusses the background and related work. Chapter 3 introduces our fault-tolerant data fusion as well as self-recalibration techniques for multi-sensor applications. Chapter 4, proposed a procedure to estimate an accelerometer-derived respiration signal, respiration rate as well as respiratory timing parameters. The body angles and positions have been also investigated while the synchronous and paradoxical breathing patterns are analyzed based on the proposed system, as well. Chapter 5 introduces a new algorithm to design an intelligent remote tidal volume variability monitoring system. Chapter 6 presents a comprehensive description of novel machine learning techniques for breath disorders classification. Chapter 7 addresses our proposed methodical breathing therapy framework based on wearable technology. Finally, the future works and conclusion are drawn in Chapter 8[3].

[3] Majid Janidarmian contributed to the experimental setup, collection of the data, discussion of results and final papers structures. The experimental measurements on temperature sensors and technical modifications (Chapter 3) have been done by Omid Sarbishei, Benjamin Nahill and Majid Janidarmian at the Integrated Microsystems Lab (IML), McGill.

Chapter 2

Background and Related Work

This chapter begins with describing the background and previous work on accuracy analysis, calibration, and fault-tolerant designs in the multi-sensor systems. A brief background is given on exploring respiratory parameters with medical devices. Then, some discussions on previous accelerometer-based approaches to obtain the respiration signal and body positions are provided. Since, up to our knowledge, there have been seldom investigations in using wearable motion sensors for estimating different respiration parameters discussed in this thesis, we also illustrate the related studies, which applied other types of sensors and devices. Subsequently, different previous classification techniques for breathing disorders recognition are described. This chapter ends with a survey of the health-related research, work on the impact of breathing therapy on various health conditions.

2.1 Calibration and Fault-Tolerant Data Fusion

In this section, we address the related work on accuracy analysis, calibration, and fault-tolerant data fusion techniques in multi-sensor systems. Calibration is a crucial step in improving the accuracy of individual sensors exist in a multi-sensor system. Certain systems might require dedicated calibration procedures, which in general can be categorized under online or offline methods. Offline methods are mostly based on curve fitting, such as, the Least-Square (LS) method, to map raw sensor readings into corrected values [49] and compensate the systematic offset and gain. On the other hand, online methods are based on time series and prediction in real-time, such as Kalman filters [50]. In [51], Bychkovskiy *et al.* suggests a methodology for localized calibration of the light sensors. It first considered the physically close sensors and used temporal correlation of signals received from neighboring sensors to derive a function relating their bias in amplitude. Then in the next part, it obtained the most consistent way to provide all pairwise relationships by modeling the system as an optimization problem. Feng *et.al* [49], have focused on both offline and online calibration of light sensors. The calibration problem is formulated as a nonlinear minimization function which solved by the standard conjugate gradient approach. The results are shown on a set of photovoltaic optical sensors considering the point-lights model. In offline calibration of the light sensors, they make use of linear Least Square (LS) method on two separate sets of recorded data versus the reference data captured by high-quality and high-cost light meters. [52] presents two methods for smart temperature sensors calibration that are based on voltage measurements rather than temperature values. In the first method, the sensor's measurements after calibration report the error of $\pm 0.15°\text{C}$ over the temperature range from -55°C to 125°C. However, due to the use of small voltages, the implementation of such a method might be infeasible in a production environment. To overcome this problem, their second method uses larger external reference voltage to the chip during calibration and the chip's temperature is determined via the Analogue to Digital Convertor (ADC). Therefore, any errors caused by ADC would effect on the quality of their calibration. Although, this technique obtains an error of ±0.25 $°C$ over the same range of temperature, its specs compared favorably to the current commercial temperature sensors [53]. The approach described in [54] introduces a system of temperature sensors, which adopts ARM processor LM3S1138 as its controlling core. The LS method is applied to fit the temperature sampling values in connection with the readouts from the temperature sensors. In this method, the maximum and minimum readouts of ten measured data at each sampling point are extracted, and then the average of the remaining eight readouts is used as the reference model for the purpose of calibration. They use polynomial of degree three for each range of temperature, independently.

In general, faults at sensor level can be categorized as either complete sensor failure (permanent faults), such as stuck-at faults, or transient faults, which might happen over only a limited period of time. There exist in the literature approaches that aim to detect the faults in sensor readouts based on the typical fault models in [55]-[57]. Such approaches are based on first capturing the sensor readouts for a reasonably long amount of time, and then comparing the results with the given statistical characteristics of the sensors in their normal operation mode. Next, if the results of a sensor deviate from the expected characteristics by a particular threshold, then the sensor is assumed to be faulty. The approach in [55] also proposes a technique to find the optimal threshold value for such a purpose. Albeit useful, these techniques are not applicable to the applications, where it is required to detect the faulty sensors in a short amount of time, e.g., in health systems [58]. In fact, sensor failures may occur within relatively short intervals. Hence, it is a must to provide data fusion techniques to detect faults periodically within a relatively short amount of time. The approach provided in [58] is more suitable for such purposes. However, they can only handle single fault and are not efficient when multiple faults occur. It presents a fault-tolerant technique for glucose sensor readouts based on an average computation over multiple sensor readouts. The basic idea is to throw away the sensor readout, which is furthest from the average. That way, faults caused by the complete failure of a sensor, body rejection, etc, can be detected relatively fast to increase the robustness of the average computation. The major inefficiency of this approach is that, it is unable to detect multiple failures that lead to a specific adverse outcome. Multiple faults are usually hard to detect and tolerate. Some approaches such as [59] focus on diagnosing multiple faults in a multi-sensor system using a conventional fuzzy soft clustering. This method contains of two phases, first, a fused signal is generated by the sensor readouts by the c-means algorithm [60] and next, the information provided by the sensors and the fused signal are used to detect the faulty sensors. This approach is computationally expensive to be performed in real-time due to the potential convergence issues of the c-means algorithm. From an accuracy point of view, a basic data fusion approach to increase the accuracy of sensor readouts in a multi-sensor system is to perform a simple average computation over the results [61]. This technique improves the Mean-Square-Error (MSE) by factor of n, if all sensors are identical in terms of the statistical characteristics, where n is the number of sensors measuring the same data. However, the normal average computation is not robust enough against faults. A weighted average computation can be performed to minimize MSE. The solution in [62] uses a neural-network-based training heuristic to optimize the weights for the purpose of average computations.

We propose a new self-calibration and data fusion algorithms in Chapter 3, which are applicable to a central multi-sensor architecture, for which the post-calibration statistical characteristics of sensors can be experimentally measured. In a central multi-sensor architecture, the sensors communicate through a central processor and they capture the same reference data.

2.2 Respiration Signal, Parameters, and Body Positions

There have been a variety of direct and indirect methods for estimating respiratory parameters [63][64]. For instance, the flow meters including pressure transducers, thermal flow meters, and ultrasonic flow meters are known as the direct methods. The method based on the blood oxygen level [65] is an example of indirect technique. This technique does not provide a reliable indication of changes in breathing pattern while has slow reaction to breath disturbance. This time lag depends on the complexity of the algorithms and might exceed 15 to 20 seconds [65]. The pulse oximetry has several limitations including ambient lighting, skin pigmentation, tissue perfusion, and hemoglobin concentration [66]. It is shown that, this device is more likely to overestimate the oxygen concentration at low saturations in individuals with darker skin. The work presented in [67] also shows that the monitoring respiration signal based on pulse oximetry has the restriction of electromagnetic interference caused by electrosurgical cauterization units or cellular phones. In addition, in case of perfusion reduction and small pulse amplitude, the device will be prone to error and be unable to obtain a reading resulted in generating false alarms [67]. The light emitted from the device is harmful to the eyes, so the users should not stare at the light. The pulse oximeters are not recommended for long time monitoring since painful feeling might appear if using the device ceaselessly, especially for the children. Another indirect method is based on the measurements of tracheal breath sounds. Although it is an efficient method for detecting deep and low breathing sound amplitude, it does not exceed the background noise whereas the relationship between the sound amplitude and air flow is very difficult to detect [68]. Respiratory waveform was obtained by using a piezoelectric respiration transducer in [69]. The sensor, placed around the thorax, generates a high-level linear signal in response to changes in thoracic circumference, associated with respiration. They also proposed a Patient Personal Server (PPS) to collect the data from the breathing module, processing the signal and then transmit it to a database stored on a telemonitoring server. Recently, [70] proposed a non-contact system based on the COTS TX-RX Pair. The results are investigated on three types of experiments for one person in lying position and different postures. The mean absolute error of 0.12 respiration per minute (rpm) is obtained for the respiration rate estimation. Nepal *et al.* [71] applied an abdominal strain gauge transducer for classifying the breath signal into apnea, normal respiration or respiration with motion categories. They used second order autoregressive modelling and zero-cross algorithm in which

the square root of energy index is considered as the baseline for respiration rate calculation.
Another monitoring method is the vision-based system. [72] proposed a camera-based technique for real-time respiration signal and breath rate extractions. Their method includes image and signal processing techniques to extract chest and abdominal movements' information from a sequence of video recorded by a single video camera. Their assessments indicated an estimation error of 3% for respiration rate considering a 3-10 minutes test on a single subject in sitting position. Such a monitoring system not only demands high cost, but also may be considered to be an invasion of patients' privacy. Furthermore, the accuracy directly depends on the patients' cloths patterns as well as their distance from the camera. There are medical mattresses which can calculate the patient's respiration and pressure distribution [73]. When using a transducer under the mattress, the changes of pressure produced by the respiration movements are partially absorbed by the mattress, therefore it is subject to error and inaccurate results. Watson *et al.* [74], proposed a method for monitoring respiration signal by measuring the inductance of an extensible electrical conductor closely looped around the body to calculate the variations in the patient's chest and abdomen areas.
An ECG-based technique for calculating the respiration frequency on both simulated and real data during stress testing is discussed in [75]. The respiration error rate of 0.5% ± 0.2% is reported for simulated signal while this error increases to 5.9% ± 4% considering 12 leads worn by 34 subjects in a real test. Likewise, [76] described a method for respiration rate estimation based on the ECG signal. They tried different combination of 12-lead ECG, which was digitalized, with a sampling rate of 1 kHz, and an airflow-thermistor-based technique was used with sampling rate 50Hz as the reference device. The best error in respiration rate estimation with normal breathing pattern is achieved 1.07% ± 8.86% based on using 3 Vectorcardiographic leads (VCG). The solution in [77] makes use of a combination of information from several ECG-Derived Respiration (EDR) signals to provide an estimation of respiration rate. A relative error of 0.50% ± 4.11% for tilt test and 0.52% ± 8.99% for stress test are computed from VCG leads. The issue with ECG is that the electrodes are taped directly on the skin. Therefore, removing the adhesive bonding will cause the skin tissue injury and contact skin dermatitis if they are in use for long time [78]. Due to this fact, they are not recommended to be used for round-the-clock monitoring applications. In the proposed framework, there is no need to connect the sensory node directly on the skin, which may cause sweating or irritations for sensitive skins such as for newborn infants or children. Furthermore, the

previous studies are mostly based on recording the ECG data from the laboratories or hospital facilities.

One recent area of interest is applying motion sensors to detect the small movements of the body that occur during expansion and contraction of the lungs in each respiration cycle. In [79], an accelerometer and pressure sensors are worn on the body to obtain the respiratory rate. In this work, the data were collected by the data acquisition card, and then the processing has been run in LabVIEW software. In this assessment, respiratory rates deviating less than 0.5 bpm from Finapres as the reference signal. An oximeter combined with an accelerometer sensor is used in [17] to diagnose sleep apnea, COPD and asthma. They investigated the impact of body posture in analyzing the respiratory movements. They also proposed a method to detect the apnea and hypopnea events in real-time and then Apnea/Hypopnea Index (AHI) is calculated. The analyzed data are recorded on a PC or cellphone to be sent to the remote center or physicians. However, the limited data storage might bring problem especially for daily monitoring applications. A validation of respiratory signal derived from suprasternal notch acceleration has been investigated by [80] for different body positions. They show that the respiration rate from the accelerometer has 1.55% error with respect to the spirometer. Their data storage and processing are performed on a computer with their custom build LabVIEW Virtual Instrument. Moreover, the respiration rate is estimated by strain gauge transducer and the error rate of 4.9% is achieved with respect to the spirometer signal. In [81], the respiratory component is also extracted from the accelerometer mounted on the suprasternal notch of the subjects. The vibrations are recorded with a Transducer Electronic Data Sheets (TEDS) lightweight piezoelectric accelerometer. The results are evaluated versus the sleep laboratory polysomnography as the reference. The data acquisition is done with a compact system and a laptop where data were stored to be used later. Their results represent the feasibility of implementing an accelerometer-based portable device for respiration recording. Electrocardiography, 3-axis accelerometer, and respiration belt data were used and analyzed in [82] from ten healthy volunteers. Respiration rate and flow waveform are also estimated in [83] from a tri-axial accelerometer data attached on the left lower costal margin under the ribs of the subject. The estimations are calculated through utilizing the angular rates of breathing motion. The assessments are based on cannula measurements as their reference device. The respiration signal and heart rate are extracted offline from the accelerometer sensor and compared with the reference. The data is collected in a memory stick and analyzed later in a computer. Silva *et al.* [10] evaluated a system comprised of a microprocessor with an accelerometer sensor for breath study in both animals and humans. This method is based on on-board signal processing and alarm means. The authors in [84] introduced a fusion algorithm for accelerometer and gyroscope signals to calculate the respiration rate. They considered two types of exercises, and the respiration rate errors are calculated as 4.6% and 9.54% versus the piezoelectric respiratory belt for the treadmill and leg press, respectively. Table 2-1 summarizes the previous methods that have been used for respiratory parameters estimation.

In addition to obtaining an accurate respiration signal, several methods and approaches investigate the impacts of body positions for different breath disorder problems. For example, Fernandes *et al.* investigates the effect of the body position in Obstructive Sleep Apnea for children. They conclude that, unlike adults, children with OSA breathe best when in the supine position [85]. After the "Safe to Sleep" campaign was introduced in 1994, the SIDS rates have been decreased sharply. Recently, [86] reposts that, the rate of putting infants in prone position at sleep has decreased 50-90%, which resulted in reduction of 50-90% of infant mortality caused by SIDS. Different studies have shown the effectiveness of "positional therapy" for mild to moderate positional OSA [87][88]. In [89], sixteen patients with positional OSA were considered and instructed how to perform the treatment for a test night and for three months' duration. The mean Apnea-Hypopnea Index (AHI)—the number of apnea and hypopnea events per hour of sleep—decreased from 26.7 ± 17.5 to 6.0 ± 3.4 during the test night. At three months test, the improvement persists the same in AHI compared to the night test. Therefore, the selected volunteers could be effectively treated by a positional therapy for 73.7%. Lee *et al.* has also examined the body position in patients suffering from sleep apnea and reported the effectiveness of the lateral position in reducing sleep disorder symptoms particularly in mild and moderate sleep apnea [90]. In addition, 40° rotation from the supine position with slightly more than 20mm elevation of the upper trunk levels were recommended to reduce the OSA events of more than 80%. Gastro Esophageal Reflux Disease (GERD) is a condition in which the stomach contents leak backwards from the stomach into the esophagus. This can irritate the esophagus and cause heartburn and other symptoms. According to [91] and Dr. David A. Johnson, Professor of Medicine and Chief of Gastroenterology at Eastern Virginia School of Medicine, for people suffering from GERD, the left lateral position is preferable. In Chapter 4, we make use of an accelerometer sensor to remotely calculate the body angles associated with different body positions in terms of pitch and roll angles.

Table 2-1: Previous methods in respiratory parameters estimation

REF #	Sensor Type	# of Sensors	Sensor's Location	Wireless	Privacy Problem	# of Subjects	Portable	Technique	Outcome
[69]	Piezoelectric belt	1	Around the thorax	Yes	No	0	Yes	Described a wireless system to be applied for breathing monitoring	Display respiration signal for patients as well as sending to a telemonitoring system
[68]	Microphone	1	Trachea at the level of the thyroid cartilage	No	No	11	Yes	Respiratory waveform was obtained by using a piezoelectric respiration transducer vs. pneumotach	Estimating the tidal volume in different positions with error of 13.2% ± 8%
[70]	Single COTS TX-RX pair	1	Attached on the bed	Yes	No	1	No	Profiltering is applied to increase the SNR of noisy signals, it uses real-time spectrum analyser as the reference	Respiration rate estimation error of 0.12 bpm
[80]	Stain gauge	1	Around the thorax	No	No	9	Yes	Calculating respiration rate and correlation vs. spirometer	Respiration rate estimated by error 4.9% with correlation coefficient 0.68 ± 0.21
[72]	Camera	1	In different angles in front of subject with different distances	Yes	Yes	2	No	Technique to extract chest and abdominal movements' information from a sequence of video recorded applying a single video camera	An estimation error of 3% for respiration rate considering a 3-10 minutes test

REF #	Sensor Type	# of Sensors	Sensor's Location	Wireless	Privacy Problem	# of Subjects	Portable	Technique	Outcome
[75]	ECG	12 leads	Different places of the body	No	No	34	No	Exploits the oscillatory pattern of the rotation angles of the heart's electrical axis as induced by respiration	The respiration error rate 5.9% ± 4% in real test
[77]	ECG	3 VCG leads	NA	No	No	29	No	The proposed method is based on QRS slopes	Estimation relative error of 0.5% ± 4.11% for tilt test and 0.52 ± 8.99% for stress test
[76]	ECG	3 VCG leads	NA	No	No	29	No	The slope between the peak of Q and R waves, the peak of R and S waves, and the R-wave angle were combined for respiration rate estimation	The respiration error rate 1.07% ± 8.86% with normal breathing pattern
[17]	Accelerometer+ Micro respiratory sensor+ Pulse oximetry	3	Upper body+ Nasal cannula+ on fingertip	Yes (Bluetooth)	No	1	Yes	Investigates the impact of body posture in analyzing the respiratory movement	Respiration airflow/ blood oxygen/ body position
[80]	Accelerometer	1	Suprasternal notch	No	No	9	Yes	Calculating respiration rate and correlation vs. spirometer	Respiration rate estimated by error 1.55% with correlation coefficient 0.88 ± 0.09

REF #	Sensor Type	# of Sensors	Sensor's Location	Wireless	Privacy Problem	# of Subjects	Portable	Technique	Outcome
[79]	Accelerometer+ Pressure sensors	3	Chest	No	No	1	Yes	Constructs a special respiratory rate sensor belt, data were collected by the data acquisition card	Respiration rate with less than 0.5 bpm deviation from Finapres as the reference signal
[81]	Accelerometer	1	Suprasternal notch	No	No	15	Yes	Estimating respiration rate w.r.t. 12 PSG sensors (exclusive focus in the case of the PSG thermistor as the reference)	The precision oscillates around ±3 breathings/min
[82]	Accelerometer+ ECG+ Respiration belt	3	Sternum region	No	No	10	Yes	The respiration signal and heart rate are extracted offline from the accelerometer sensor	The mean correlation coefficient of 0.99 considering normal, slow and fast breathing patterns
[84]	Accelerometer+ Gyroscope	2	Around the thorax	Yes	No	10	Yes	Introduced a fusion algorithm for accelerometer and gyroscope signals to calculate the respiration rate	Respiration rate errors of 4.6% and 9.54% vs. piezoelectric respiratory belt for the treadmill and leg press, respectively
[83]	Accelerometer	1	Left lower costal margin below the ribs	Yes	No	1 healthy and Patients	Yes	Estimating respiration rate by angular rates of breathing motion vs. nasal cannula as the baseline	Respiration rate estimated by error 0.38 bpm with correlation coefficient 0.98

2.3 Rib Cage and Abdomen Synchrony Analysis

The other factor, which might help for diagnosis and treatment of breath problems, is the analysis of the rib cage and abdominal synchrony during breathing function. Based on [92][93], asynchronous breathing is defined as the difference in time of expansion or retraction between the compartments of the chest wall. However, in case of extreme phase difference, the movement among the compartments becomes opposite, and then the paradoxical movement occurs [93]. Paradoxical behavior of the chest wall in COPD patients is recognized for many years [94][95]. Recently, [96] provides a literature review on OptoElectronic Plethysmography (OEP) as an indirect measurement of pulmonary ventilation. They applied 89 passive markers, which were placed on different parts of upper body with a sampling frequency of 50Hz. Four CCD cameras are used to capture the 3D coordinates of each marker. The cameras operate at up to 120Hz and are synchronized with axial diodes that emit infrared light. The system showed good intra – and inter-rater reliability, with intra-class correlation coefficients above 0.75 for most of the analyzed variables. OEP is also used for movement analysis of the rib cage and abdomen. Even though OEP is a new reliable method for breath analysis, it is impossible to use it for remote monitoring of respiratory parameters since the use of OEP requires laborious and complex calibration procedures.

Paradoxical motion of the chest compartments could alter the normal pressure relationships between the thoracic and abdomen during inhalation and exhalation [97] .This probably affects the amplitude of rhythmic fluctuations of blood volume, which activates homeostatic reflexes involved in maximizing optimal cardiorespiratory interaction and regulating blood pressure [98][99]. Therefore, habitual existence of pathological breathing such as paradoxical pattern may damage the function of homeostatic reflexes. Despite their critical significance, the abnormal respiration patterns are often overlooked resulted from a lack of diagnostic and therapeutic tools. Therefore, to address this problem, in Chapter 4, a novel solution that takes in this idea and leverages the potential of the wearable motion sensors is presented.

2.4 Tidal Volume Variability

Based on study in [100] for patients suffering from breath disorders, the destruction of lung capacity occurs over an initial period of two to four days. Thus, continuous monitoring of the tidal volume variability plays an important role in respiratory disorder diagnosis. According to [101] for a fixed set of patient conditions, the alveolar ventilation depends on tidal volume variability. Alveolar ventilation refers to the amount of air reaches the alveoli for gas exchange with blood per unit time. At normal rates of positive pressure ventilation, if the tidal volume goes less than or close to total dead space (about 26% of the resting normal tidal volume [102]), it will cause the lack of alveolar gases, regardless of the respiratory rate and minute volume. This would cause carbon dioxide retention in the bloodstream rapidly as well as progressive lung disease, deteriorating ventilation-perfusion matching and eventually, impaired oxygenation. Pneumothorax is another respiration disorder known as "air in the pleural cavity" which has two major signs including shortness of breath (low breath volume) and Tachypnea [102]. According to Chang and Mukherji [103], the incidence of primary pneumothorax in the USA is 7.4-18 cases and 1.2-6 cases per 100,000 persons per year for men and women, respectively. Without continuous monitoring, people often do not seek medical attention after their symptoms develop more serious due to comorbidity causing Secondary Spontaneous Pneumothorax (SSP). Furthermore, emphysema known as a common cause of SSP is a Chronic Obstructive Pulmonary Disease (COPD) where there is over-inflation of the alveoli in the lungs, resulted in breathlessness. Therefore, the symptoms associated with pneumothorax, emphysema and COPD are most likely diagnosed through analyzing respiration patterns, such as Tachypnea and shallow breathing pattern.

At the opposite side, too large tidal volume may produce alveolar and airway over distension which may lead to lung injury such as over-expansion, pulmonary interstitial emphysema and pneumothoraces. Dreyfuss *et al.* has shown that breathing with large tidal volumes causes the fluid accumulation in the air spaces and parenchyma of the lungs resulted in pulmonary edema [104]. Hernandez *et al.* [105] explored the effects of high tidal volume on immature rabbits and demonstrated the major role of volume distension of the lung in the progress of lung injury. In Chapter 5 of this thesis, we focus on proposing a remote monitoring system which will enable proactive home monitoring with estimating the tidal volume variability as well as triggering an alarm signal to a health care center or caregiver in case of any unexpected event. These are essential features especially for an aging population and can result in lowering the cost of health care by moving some of the eligible patients from hospital to home.

2.5 Breathing Disorders Recognition

Different machine learning techniques, such as linear and quadratic discriminant model [106], regression tree method [107], Bayesian hierarchical [108] and Support Vector Machine (SVM) [109] have been used for automatic recognition of Obstructive Sleep Apnea (OSA) based on the features extracted from Heart Rate Variability (HRV) and ECG-derived respiration (EDR) signals. In [110], the authors applied the wavelet transform and an Artificial Neural Network (ANN) algorithm to the electroencephalogram (EEG) signal in order to identify sleep apnea episodes. The EEG signals are classified into four frequency bands of basis waves: delta (δ), theta (θ), alpha (α) and beta (β). In case of apnea the EEG signal shifts above the delta frequency band. Then, sleep EEG activity shifts from a delta wave to theta and alpha waves frequency bands in the range of 4~14Hz once episode of apnea ends. The system's identification achieved a sensitivity of approximately 69.64% and a specificity of approximately 44.44%. In 2013, Koley *et al.* [111] presented a real-time portable apnea and hypoapnea detection system based on SVM with Gaussian Radial Basis Function (GRBF) kernel and oronasal airflow signal. They achieved the detection accuracy of 93.4% and 91.8% on 8 different subjects in the offline and online tests, respectively. Although useful, all these methods require signals, which are only available in hospitals or laboratories and could not provide automated wireless remote detection.

There exist in the literature approaches that aim to classify the abnormal breathing from normal respiratory conditions [112]-[114]. For instance, [112] used a multi-layer perceptron neural network classifier applied on spirometry data. The total accuracy, sensitivity and specificity of 97.6%, 97.5% and 98.8% are achieved, respectively. Mahesh *et al.* [113] discussed the problem of binary classification with 92% accuracy through pulmonary function test and neural network. A Radial Basis Function neural network is described in [114] with flow-meter spirometer to differentiate between normal and obstructive abnormality. The validity of their result was tested with the accuracy 90%. In [115], the authors provide a combined two sequential binary neural network classifiers to detect normal, obstructive and restrictive breathing models. The first classifier separates the normal and abnormal patterns followed by the second binary classification between obstructive and restrictive breathing models. They could obtain an average accuracy of 92.5%.

Breath sound has been widely used in diagnosing of respiratory diseases, such as flu, pneumonia and bronchitis. Palaniappan *et al.* [116], proposed a method which used MelFrequency Cepstral Coefficients (MFCC) as features extracted from respiratory sounds. They applied SVM classifier to distinguish normal, obstruction pathology airway and parenchymal pathology. They achieve an average classification accuracy of 90.77%. Recently, [117] proposed a binary classification technique based on the maximum likelihood approach by using Hidden Markov Models (HMMs). They include the impacts of both lung and heart sounds in their feature extraction phase. The classification rate of 81.3% is reported for distinguishing between healthy people and patients when the classifier is trained only by the lung sound (Baseline) [118]. However, this rate increases to 83% with both lung and heart sound parameters. The lung sound classification is also used for Pulmonary Emphysema (PE) diagnosis in [119]. The accuracy of 83.9% between healthy subjects and patients is achieved. All these techniques are based on classification of breath sounds either alone or combined with heart sound. Breath sound is often considered as a band-limited or broadband noise [120] and needs enhanced signal processing to be integrated in a reliable breath disorders diagnosis. In this way, this work seeks to contribute to a better understanding of the requirements of remote detection systems and aims to help paving the path to a new generation of accelerometer-based respiration monitoring approaches for their use in the real world.

2.6 Breathing Therapy

Breathing therapy has been proven itself to be an effective, drug free remedy for a host of various health conditions. Indeed, this reduces symptoms and improves the health of patients suffering from asthma, anxiety, speech disorders, chronic muscular skeletal dysfunction and medically unexplained physical symptoms [121].

Various studies have shown the effectiveness of yoga-based breathing techniques in asthma [122][123], hypertension [124], diabetes, and ischemic heart disease [125]. A research study [126] also showed a positive outcome in the application of yoga-derived breathing as a therapeutic method for patients suffering from COPD. [127] compares the patients who received standard cardiac rehabilitation with those getting additional training in breathing therapy after Myocardial Infarction (MI). It was concluded that the group with breathing therapy had about 30% decrease in cardiac events at 5-year follow-up. Dixhoorn *et al.* showed that exercise training in patients with MI was not always successful in avoiding future cardiac events; however, the risk of treatment failure is decreased by half when breathing therapy was added to exercise training [128]. The breathing therapy has been discussed based on yoga breathing patterns. It also found to be useful to improve hemodynamic and various cardio respiratory risk factors in cardiac patients [129]. The Buteyko breathing is a technique, which aims to correct the acute and chronic hypocapnia. It includes a unique set of breathing exercises that uses breath control and breath-holding to treat a wide range of health conditions related to hyperventilation and low carbon dioxide .The BBT exercises try to augment the CO_2 level while may also be useful in reducing hyperinflation [130]. According to Australian Department of Health, the quality of Buteyko is known stronger than any other supplementary medicine treatment of asthma [131]. Concretely, it is very important for patients to follow exact instructions since otherwise it may cause lung problems such as over-expansion. Therefore, Chapter 7 aims at providing a system that helps people evaluate their progress during practicing the prescribed breathing exercises, quantitatively.

Chapter 3

Fault-Tolerant Data Fusion and Self-Recalibration of Multi-Sensor Systems

Multi-sensor data fusion is an efficient method to provide both accurate and fault-tolerant sensor readouts. Furthermore, detection of faults in a reasonably short amount of time is crucial for applications dealing with high risks. In order to deliver high accuracies for the sensor measurements, it is required to perform a calibration for each sensor. This chapter considers the problem of self-recalibration of multi-sensor systems for health applications after detecting the decalibrated sensors using a real-time screening technique. The least squares method is applied to calibrate each sensor using a linear curve fitting function. Three methods are introduced for jointly calibrating the system and finally an analytical technique is proposed to carry out a fault-tolerant multi-sensor data fusion, while minimizing the Mean-Square-Error (MSE) for the final sensor readout. Although all these approaches are generic and applicable to different systems, the experimental results are evaluated on digital temperature sensors due to their simple and reliable setup.

3.1 Motivation

The last decade has witnessed vast biomedical applications for sensing and monitoring devices. The current medical sensing systems specifications require high accuracies, as well as tolerance to faults which could be produced by decalibration or external noise [132]. Hence, numerous researches are dedicated to improve such parameters [133]-[134]. The error occurring at a single sensor's readout can be distinguished as a systematic offset and gain as well as a random noise [49]. The systematic offset and gain are deterministic values. However, the random noise, which is often caused by environmental conditions and hardware noise, is time-variant, and is mostly assumed to have a Gaussian distribution [133]. Calibration, which is defined as the process of mapping raw sensor readings into corrected values [135], can be used to compensate the systematic offset and gain. Note that when the gain and offset are both constant values and independent from the sensor measurements, then the calibration is translated into a linear curve-fitting function.

In the cyber-biological systems due to inherent deficiency or aging, the sensors can suffer from large calibration shifts. For example, the current push for Closed-Loop Insulin Control (CLIC) systems must guarantee the continuous supply of insulin to the patient without causing the possibly dangerous state of hypoglycemia. This task is not possible to achieve without multi-sensor platform. Meanwhile, for the recalibration of the sensory systems, a patient will have no access to special calibration hardware or expert data analysis. Therefore, a blind sensor recalibration method is required with high accuracy coupled with reasonable complexity for multi-sensor devices. Manual calibration of every sensor is an unfeasible task, as a typical multi-sensor system can incorporate even tens of sensing devices [134]. Blind-recalibration requires no user intervention, but were demonstrated only for specific cases. Since health care applications need more accurate measurements than these provided by uncalibrated low-cost sensors, the need of automatic methods for jointly calibrating the medical multi-sensor systems has to be considered.

Data fusion is another efficient approach, which combines data from multiple sensors to achieve more accurate readouts compared to the case where a single sensor is used alone [136]-[139]. A straightforward approach to increase the accuracy of sensor readouts in terms of the error measure Mean-Square-Error (MSE) is to perform an average computation over the results [61]. This technique can improve the MSE by the factor of n, where n is the total number of sensors. Data fusion methods can also be used to detect faulty sensors [58] and deliver fault-tolerant measurements. This is crucial, since the technology trends indicate that sensing has by far the highest fault rates [2]. Furthermore, fault tolerant sensor readout in a reasonably short amount of time is a critical task for applications dealing with high risks such as medical cases.

This chapter considers the problems of both non-blind and blind calibration of multi-sensor systems. In addition, we focus on designing a fault-tolerant system with tolerance to multiple faults. While all these approaches are generic and applicable to different systems, the experimental results are evaluated on temperature sensors due to their simple and reliable setup. Note that in a central multi-sensor architecture, the sensors communicate through a central processor, and they capture the same reference data. Certain applications such as wireless systems often make use of a distributed architecture [140], where each sensor is capable of communicating with all or some of the other sensors. Such applications are not considered in this chapter.

3.2 Calibration

The least squares method is applied to calibrate each sensor using a linear curve fitting function with respect to a reference system. Linear curve fitting is the most commonly used approach, which approximates the output y as a polynomial with respect to the input x, i.e. $y = a_0 + a_1x + a_2x^2 + \cdots a_nx^n$. Note that the output y is linear with respect to the coefficients $a_0, \ldots, a_n$. The first-degree polynomial, i.e., $y = a + bx$ is mostly sufficient to approximate the output-input characteristics, where y is the reference data, and x is the raw sensor readout. This is due to the fact that the raw sensor readout mostly involves a constant offset and gain, which can be compensated using least squares method. The coefficients a and b must be set to minimize the Sum of Square Error (SSE) function, which is defined as follows:

$$SSE = \sum_{i=1}^{N} \left(y_i^{ref} - y_i^{calib}\right)^2 \tag{3-1}$$

Where y_i^{ref} and $y_i^{calib} = a + bx_i$, are the reference and calibrated values at the i_{th} measurement, and the value of x_i is the i_{th} raw sensor readout.

3.2.1.1 Self-Recalibration Techniques

All medical equipment needs to be periodically calibrated to guarantee accurate measurements. Automatic recalibration at the point of use is generally quicker and if the device can self-calibrate, even for just the most important points, then it will be more effective than if it must be moved to other place for calibration. In this section, first, the proposed screening process is explained which quickly detects the potentially faulty sensors online. The following notations are used in this section in Algorithm 3-1:

$x_{readout,i}$: The i_{th} sensor readout ($i = 1, \dots, n$), where n is the total number of sensors,

x_r: The reference data to be measured,

e_i: The error of the i_{th} sensor readout after non-blind calibration, that is: $e_i = x_r - x_{readout,i}$,

M_i: The maximum absolute error of the i_{th} sensor readout after non-blind calibration, that is, $M_i = max\ (|e_i|)$. Note that M_i is obtained through experimental measurements,

f_i: The indices of the decalibrated sensors,

A_i: The Minimum Mean Square Error (MMSE) coefficients for sensor i,

a_i, b_i: The gain and offset values for recalibrating sensor i, respectively,

$x_{ref,i}^{1:t}$: The reference readout of i_{th} sensor in the dataset with t samples,

$x_{est,i}$: The estimated reference value for self-recalibration of i_{th}sensor,

$x_{recalib,i}$: The recalibrated value of sensor i,

ID_i: The identity number of i_{th} sensor.

The initial phase in the recalibration process performs a screening of all the sensors in the system in order to exclude faulty or decalibrated sensors. The screening process is addressed in Algorithm 3-1. The *for* loop in step 1 is executed k times, where $k < n$ is the number of potentially decalibrated sensors, which deviate from the average of other sensor readouts by a distance higher than M_i (step 8). The list of the decalibrated sensors is returned in $f_{1:k}$. The primary idea for self-recalibration is to consider the average of sensors readouts as a reference to be fitted linearly using the method of least squares while excluding the decalibrated nodes. The acquired gain and offset are to be used for further readouts. The algorithm for self-recalibration of a single decalibrated sensor $(k = 1, f_{1=}f)$ with index f is presented in Algorithm 3-2. This solution has a low complexity, which makes it suitable for real-time blind calibration. However, the quality of recalibration suffers, and has to be improved especially in the critical areas such as health monitoring devices. For that purpose, in Algorithm 3-3, we propose a second method of recalibration. In this method, first a dataset is generated during the operation of the multi-sensor platform when all sensors are work properly. For each sensor i, all combinations of other sensors

Algorithm 3-1

$\boldsymbol{faultScreening}\ (M_{1:n}, x_{readout,1:n}, ID_{1:n}, f_{1:k})$ {
// ***Inputs***: $M_{1:n}, x_{readout,1:n}, ID_{1:n}$ ***Output***: $f_{1:k}$

$\boldsymbol{for}\ (m = 1; m \leq n; m++)\{$
    $sum = \sum_{j=1}^{n} x_{readout,j};$
    $\boldsymbol{for}\ (i = 1; i \leq n; i++)\{$
        $c_i = \frac{sum - x_{readout,i}}{n-1}$; /*Average computation excluding $x_{readout,i}$*/
        $d_i = |x_i - c_i|;$ } /*Deviation from the average of others*/
    $\boldsymbol{for}\ (i = 1; i \leq n; i{+}{+})\{$
        $\boldsymbol{if}\ d_i = \boldsymbol{max}(d_{1:n})\ \boldsymbol{break};\}$ /*Find the furthest from average of others*/
    $\boldsymbol{if}\ d_i > M_i$ {
        $f_m = ID_i;$
        Throw away $x_{readout,i}, ID_i, M_i;$
        $n = n - 1;$ }
    $\boldsymbol{else\ return}\ f_{1:k};\}\}$/*Return the identity number of decalibrated sensors*/

Algorithm 3-2

$\boldsymbol{averageRecalibration}\ (x_{readout,1:n}, f, a_f, b_f)\{$
// ***Inputs***: $x_{readout,1:n}, f$ ***Output***: a_f, b_f

$x_{est,f} = \frac{\sum_{i=1,i\neq f}^{n} x_{readout,i}}{n-1};$
$[a_f\ \ b_f] = \boldsymbol{fit}(x_{readout,f}, x_{est,f});$
$\boldsymbol{return}\ a_f, b_f;\}$

are obtained and in each combination, the average of sensors readouts is compared with sensor readouts i using the correlation as the criteria. The sensor set with the maximum correlation with the decalibrated sensor is stored in SS.

For example, in our experiment, sensor readouts 8 have the best correlation with the average of sensors readouts 1, 2, and 6. Therefore, the average of these three sensors is used to estimate the 8th sensor behavior for recalibration purpose. This approach leverages the correlation in the subset of

Algorithm 3-3

$\boldsymbol{correlationRecalibration}\ (x_{readout,1:n}, f, SS, a_f, b_f)\{$
// ***Inputs***:$x_{readout,1:n}$, f, SS ***Output***: a_f, b_f

1- $x_{est,f} = \frac{\sum_{i \epsilon SS} x_{readout,i}}{size(SS)}$; /*$SS$ is the Sensors Subset having the maximum correlation with sensor f obtained from offline experimental measurements*/
2- $[a_f \ \ b_f] = \boldsymbol{fit}(x_{readout,f}, x_{est,f})$;
3- $\boldsymbol{return}\ a_f, b_f;\}$

sensors without requiring a dense deployment. For each sensor, there are maximum $2^{n-1} - 1$ combinations, which have to be checked in order to find the maximum correlation. . This procedure is performed offline and only once to compute the best correlations. This method improves the accuracy of the recalibration comparing to the simple average method.

A weighted average computation can be performed to minimize MSE in order to obtain the reference of the recalibration. In Algorithm 3-4, the Minimum Mean Square Error (MMSE) estimator [141] is used to linearly find the optimum reference for recalibration. The Mean Square (MS) estimator of $x_{ref,f}^{1:t}$ given the set of non-decalibrated sensors readouts (X) is defined as:

$$x_{est,f} = E\left(x_{ref,f}^{1:t} \middle| X\right) \tag{3-2}$$

Here, the formal definitions for a single error is presented, however it could be expanded for multiple errors, as well. The homogenous linear MS estimator of $x_{est,f}$ given X= $[x_{ref,1}^{1:t} \dots x_{ref,f-1}^{1:t} x_{ref,f+1}^{1:t} \dots x_{ref,n}^{1:t}]^T$ is:

$$x_{est,f} = A_f^T X = \sum_{i=1, i\neq f}^{n} \alpha_i . x_{ref,i}^{1:t} \tag{3-3}$$

$$Objective: Min\ \{E\left(x_{est,f} - x_{ref,f}^{1:t}\right)^2\} \tag{3-4}$$

This means that the error must be orthogonal to each of the data in X. After solving this problem, we obtain:

Algorithm 3-4

$\boldsymbol{MMSE\_Recalibration}\ (x_{readout,1:n}, x^{1:t}_{ref,1:n}, f, X, a_f, b_f)\{$
// ***Inputs***: $x_{readout,1:n}, x^{1:t}_{ref,1:n}, f, X$ ***Output***: a_f, b_f

1- $A_f = MMSE(x^{1:t}_{ref,1:n}, f)$; /*procedures of equation (3-5)*/
2- $x_{est,f} = A_f \times X$;
3- $[a_f\ \ b_f] = \boldsymbol{fit}(x_{readout,f}, x_{est,f})$;
4- $\boldsymbol{return}\ a_f, b_f;\}$

$$A_f = R^{-1}P \tag{3-5}$$

Where: $R = \begin{bmatrix} r_{1,1} & \cdots & r_{f-1,1} & r_{f+1,1} & \cdots & r_{n,1} \\ & & \vdots & & & \\ r_{1,f-1} & \cdots & r_{f-1,f-1} & r_{f+1,f-1} & \cdots & r_{n,f-1} \\ r_{1,f+1} & \cdots & r_{f-1,f+1} & r_{f+1,f+1} & \cdots & r_{n,f+1} \\ & & \vdots & & & \\ r_{1,n} & \cdots & r_{f-1,n} & r_{f+1,n} & \cdots & r_{n,n} \end{bmatrix}_{n-1\times n-1}$, $r_{i,j} = E\{x^{1:t}_{ref,i} x^{1:t}_{ref,j}\}$; $i,j \neq f$.

$$P = [p_1, \dots, p_{f-1}, p_{f+1}, \dots, p_n], \qquad p_i = E\{x^{1:t}_{ref,f} x^{1:t}_{ref,i}\}\ i \neq f$$

$$A_f = [\alpha_1, \dots, \alpha_{f-1}, \alpha_{f+1}, \dots, \alpha_n]^T$$

After calculating the coefficients in step 1 in Algorithm 3-4, the recalibration reference is generated in step 2. It is then used for calculating the appropriate gain and offset. The evaluation of each method is discussed on a real dataset in details in section 3.4.2.1. The final recalibrated value of sensor f is calculated as: $x_{recalib,f} = a_f \times x_{readout,f} + b_f$.

3.3 Fault-Tolerant Data Fusion

In this section, we present a fault-tolerant data fusion technique for the multi-sensor system.

3.3.1 Statistical Distributions and Assumptions

For the purpose of this analysis, we make use of a number of assumptions, which are discussed below:

Sensor Normal Operation Mode: The proposed data fusion approach is based on average computations as well as computing the difference between sensor readouts and the average value. Hence, we have derived the statistical characteristics of the error between the calibrated sensor readout and the average of all readouts from all sensors when they are operating in their normal operation mode, i.e., the sensor is not faulty. The experimental measurements have shown that such an error fits student's t-distribution (See Figure 3-1). The t-distribution is useful when estimating the mean of a normally distributed population, where the sample size is small and population standard deviation is unknown. It is symmetric and bell-shaped, like the normal distribution. However, it has heavier tail, which makes it more inclined to producing values that fall far from its mean. As depicted in Figure 3-1, the t-distribution is a better fit to our measurements compared to the normal distribution.

- *Sensor Failure Probability:* Each sensor has a probability of complete failure, e.g., p, where p is a very small value, e.g., $p < 0.01$. Note that since p is a small value, we assume in this section that only one sensor is probable to completely fail at a time (no multiple faults).
- *Sensor Failure Readout Distribution:* When a sensor completely fails, the sensor readout could be anything. We make use of the fault model in [134] to assume that the sensor readout has a uniform distribution among the effective range of the sensor readouts, i.e., $[10^{\mathrm{o}}, 30^{\mathrm{o}}]$ for the temperature sensors in this section. In fact, it is assumed that the temperature readout is stuck at a particular temperature. Furthermore, the fault model in [134] requires adding a Gaussian noise to the sensor readout. Therefore, we make use of the Gaussian noise model obtained by our experimental measurements (See Figure 3-2) to add to the fault model.
- *Sensor Failure Original Data Distribution*: The original data that the failed temperature sensor is supposed to read could be anything in the range of $[10^{\mathrm{o}}, 30^{\mathrm{o}}]$ as well. In this section, we assume a uniform distribution for the original data among the full-scale. However, other distributions can be chosen for the original data as well. In fact, it might be possible that in some particular cases, specific original values are more probable to be read by the sensor.
- *Sensor Failure Error Distribution:* Based on the uniform distributions of the original data and the sensor readout in the failure mode, the sensor error has a triangular distribution in its failure mode within the range of $[20^{\mathrm{o}}, 40^{\mathrm{o}}]$, added by a Gaussian noise.

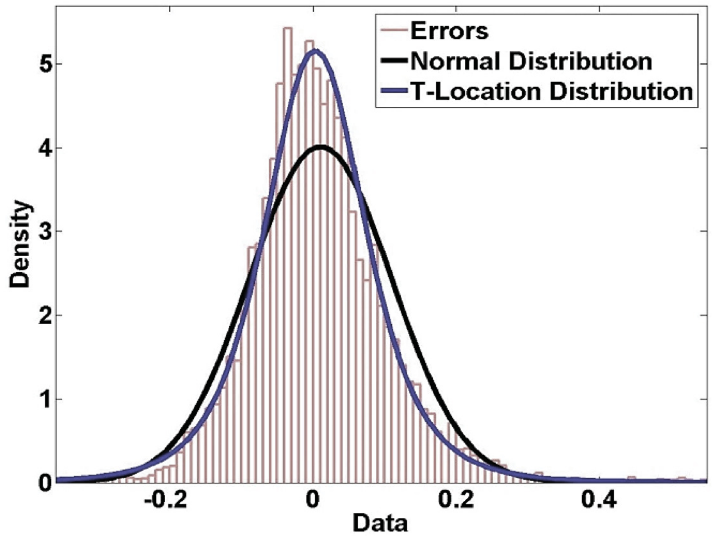

Figure 3-1: T-distribution and normal fitting of the error between each calibrated sensor and the average of all measurements

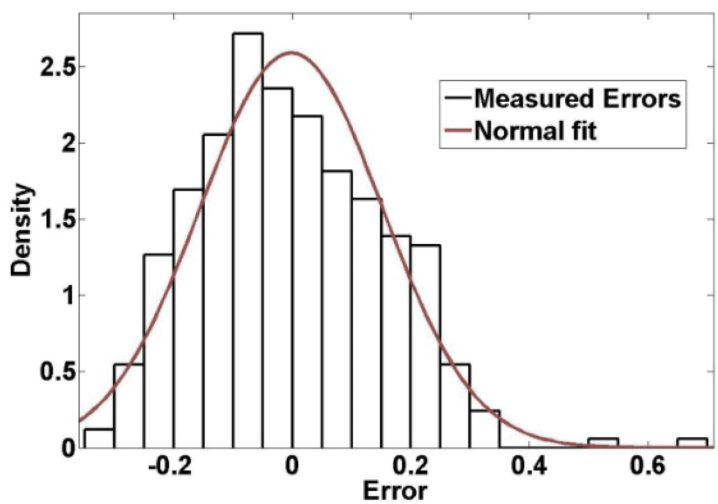

Figure 3-2: Fitting the error of 16 calibrated sensors to a normal distribution

It is notable that any other statistical distributions considered for the above variables, can also be handled by the proposed analytical framework and MSE optimization in this section.

3.3.1 Proposed Data Fusion

The proposed fault-tolerant data fusion approach, which is based on an average computation, is presented in this section. We assume that n multiple-sensor readouts, i.e., $x_1,\ldots,x_n$, measuring the same thing, are available at a time, and the goal is to return a single readout, $\hat{x}$, such that MSE is minimized and sensor failures are also handled.

The proposed data fusion algorithm is outlined in Algorithm 3-5. First, corresponding to each sensor readout x_i, an average computation excluding the variable x_i is performed in steps 1 and 2. Furthermore, the variable d_i computed at step 3 shows the absolute difference (deviation) of x_i from the average of others. Next, we find the sensor readout resulting in the maximum deviation, i.e., d_i, in steps 4 and 5. Finally, if the deviation is higher than a given threshold T, then we exclude x_i within the final average computation in step 8, since it is most likely that the sensor is faulty. Otherwise, a normal average computation is performed (when $u_i = 1$). Note that through the rest of this section we aim to find the most suitable value of T to minimize the MSE at the terminal output (single measurement $\hat{x}$). The error occurring at the final measurement $\hat{x}$ in Algorithm 3-5, as well as MSE can be computed as follows:

$$e_{\hat{x}} = \frac{e_i u_i + \sum_{j=1, j\neq i}^{n} e_j}{n - 1 + u_i} \tag{3-6}$$

Where e_j $(j = 1, \dots, n)$ is the error of the calibrated j_{th} sensor readout, e_i is the error of the sensor readout, which is furthest from the average of the rest of the sensor readouts (See step 5 in Algorithm 3-5). Hence, MSE can be obtained as follows:

$$\begin{aligned}
\Rightarrow MSE = E({e_{\hat{x}}}^2) &= E\left(\left(\frac{e_i u_i + \sum_{j=1, j\neq i}^{n} e_j}{n - 1 + u_i}\right)^2\right) \\
&= E\left(\frac{{e_i}^2 {u_i}^2 + \left(\sum_{j=1, j\neq i}^{n} e_j\right)^2 + 2 e_i u_i \left(\sum_{j=1, j\neq i}^{n} e_j\right)}{(n - 1 + u_i)^2}\right)
\end{aligned} \tag{3-7}$$

$$\xrightarrow{u_i = 0,1} = E\left(\frac{{e_i}^2 u_i}{(n-1)^2 + u_i(2n-1)}\right) + E\left(\frac{\left(\sum_{j=1, j\neq i}^{n} e_j\right)^2}{(n-1)^2 + u_i(2n-1)}\right) + 2E\left(\frac{e_i u_i (\sum_{j=1, j\neq i}^{n} e_j)}{(n-1)^2 + u_i(2n-1)}\right)$$

Algorithm 3-5

$\boldsymbol{singleMeasurement}$ $(x_{1:n}, T, \hat{x})\{$
// ***Inputs***: $x_{1:n}$, T, ***Output***: $\hat{x}$

1- $\boldsymbol{for}$ $(i = 1; i \leq n; i++)\{$
2- $a_i = \frac{\sum_{j=1, j\neq i}^{n} x_j}{n-1}$; /*Average computation excluding x_i*/
3- $d_i = |x_i - a_i|;\}$ /*Deviation from the average of others*/
4- $\boldsymbol{for}$ $(i = 1; i \leq n; i++)\{$
5- $\boldsymbol{if}$ $d_i = \boldsymbol{max}(d_{1:n})$ $\boldsymbol{break}$;}
6- $\boldsymbol{if}$ $d_i > T$ $u_i = 0$; /*Throw away x_i*/
7- $\boldsymbol{else}$ $u_i = 1$; /*Do not throw away x_i*/
8- $\boldsymbol{return}$ $\hat{x} = \frac{x_i u_i + \sum_{j=1, j\neq i}^{n} x_j}{n-1+u_i}$;} /*Final average computation*/

Algorithm 3-6

$\boldsymbol{thresholdOpt}$ $(d_{failure_1}, \dots, d_{failure_n}, d_{normal_1}, \dots, d_{normal_n}, MSE\_no\_fault,$
$MSE\_fault, T)$
//***Inputs***$d_{failure\_1}, \dots, d_{failure\_n}$,$d_{normal\_1}, \dots, d_{normal\_n}$
//***Output***: $MSE\_no\_fault, MSE\_fault, T$
/* MSE_no_fault is the value of MSE when: $p_{1:n} = 0$, and MSE_ fault is MSE when: $p_{j=1,\dots,n, j\neq k} = 0$, $p_k = 1$*/

1- Set an initial T;
2- Find the optimal T, such that:
3- MSE_no_fault ≈ MSE_avg,
4- MSE_fault = minimized,

/*MSE_avg is the MSE of normal average computation when $p_{i\in\{1,\dots,n\}} = 0$ */

Where $E(.)$ is the expectation function. Furthermore, based on the code in Algorithm 3-5 we have:

$$u_i = \begin{cases} 1 & d_i \leq T \\ 0 & otherwise \end{cases} \tag{3-8}$$

Where,

$$d_i = \left| x_i - \frac{\sum_{j=1, j\neq i}^{n} x_j}{n-1} \right|$$

The statistical characteristics of d_i depends on whether the i_{th} sensor is faulty or not. Hence, we re-write d_i as:

$$d_i = p_i d_{failure\_i} + (1 - p_i) d_{normal\_i} \tag{3-9}$$

Where p_i is the probability of Sensor#i to completely fail, while d_{normal_i} and $d_{failure\_i}$ are the values of errors d_i in the normal and complete failure modes, respectively. According to the discussion in subsection 3.3.1, d_{normal_i} has a student's t-distribution (See Figure 3-1), while $d_{failure\_i}$ has a triangle-like distribution over the range of $[20^{o}, 40^{o}]$, which is also added by the Gaussian noise in Figure 3-2. Equations (3-6) to (3-9) indicate that there is a complex correlation between u_i, d_i and e_j $(j = 1, \dots, n)$. Hence, computing the MSE in Eq. (3-7) analytically requires knowing the value of p_j in Eq. (3-9) and then solving a complicated n-dimensional joint probability distribution integral corresponding to d_j $(j = 1, \dots, n)$, which becomes hard as n increases. However, as typically the value of n (number of multiple sensor readouts) is small, we aim to compute an almost accurate value of MSE in Eq. (3-7) by making use of a numerical method. Particularly, we divide the input intervals into a number of smaller ones and then compute the integral by doing the summation instead. We then gradually increase the number of intervals, e.g., by multiplying it by two after each iteration, until the computed value of MSE converges. Please note that the run-time is not an issue, since these computations unlike the data fusion algorithm in Algorithm 3-5 are performed offline and only once to compute MSE. Next, on the top of the MSE computation using the Newton method, we aim to find the optimal threshold T to minimize the MSE in Eq. (3-7).

The proposed algorithm to set the threshold value T is shown in Algorithm 3-6. The inputs to the algorithm are the statistical characteristics of $d_{failure\_1}, \dots, d_{failure\_n}, d_{normal\_1}, \dots, d_{normal\_n}$, while the outputs are the optimal threshold T, MSE_no_fault, which is the MSE in Eq. (3-7) when no fault occurs, i.e., when $p_j = 0$ in Eq. (3-9) $(j = 1, \dots, n)$, as well as MSE_fault, which is the MSE in Eq. (3-7) when only one sensor, e.g., l_{th} sensor $(l \in \{1, \dots, n\})$, fails $(p_l = 1, p_{j=1,\dots,n, j \neq l} = 0)$. Note that other heuristics could be used instead of the Newton method to find the optimal threshold T as well.

3.4 Experimental Results

In this section, we present the results on calibration, self-calibration and the MSE minimization using Algorithm 3-5 and Algorithm 3-6 compared to the normal average computation [61], and the fault-tolerant data fusion technique in [58]. The algorithms have been implemented in MATLAB and executed on an Intel 2.1 GHz Core 2 and 2 GByte running under Windows XP.

3.4.1 Test Setup

Although all the proposed approaches are generic and applicable to different medical multi-sensor systems, the experimental results are evaluated on temperature sensors due to their simple and reliable setup. First, the temperature sensors are calibrated with respect to Temptronic TP4500 environmental thermal chamber as the reference model. The Temptronic TP4500 temperature environmental thermal chamber (shown in Figure 3-3) is ideal for lab testing and failure analysis of micro-systems due to its fast temperature transitions and high airflow over its wide operating range between -45°C and +225°C. It is also capable of traversing the full range within 12 seconds [142]. The TP4500 works by placing a thermal shroud around a device under test, and directing a flow of air over the sample at a controlled temperature. After collecting raw data from sensors, the least squares method is applied to obtain the offset and gain. We use STTS751, a 6-pin digital temperature sensor that supports different slave addresses. The STTS751 communicates over a 2-wire serial interface compatible with the SMBus 2.0 standard. The STTS751 is available in two versions. Each version has 4 slave addresses determined by the pull-up resistor value connected to the Addr/Therm pin. In our experiments, the configurable temperature reading precision is set to 12 bits, or 0.0625°C per LSB. The data of eight temperature sensors is collected by an STM32F407 microcontroller, which uses an ARM Cortex-M4 32-bit core [54], as the $\mathrm{I}^2\mathrm{C}$ master. To accommodate eight sensors with only four distinct addresses, a second $\mathrm{I}^2\mathrm{C}$ bus is used. The schematic of the proposed design is shown in Figure 3-4. In order to have more data for calibration and experiments, two systems with the mentioned design characteristics are considered.

3.4.2 Calibration Results

In our experiment 16 sensors are placed on two 5.2×4.7cm boards. We assume that after some periods of time the sensor readings become relatively stable in order to conduct the calibration.

Twelve minutes for each set point of the Temptronic is considered in order to obtain stable temperature values. In our experiment, we generate a dual-slope temperature ramp with Temptronic TP4500. The temperatures are changed in 4°C steps between 10°C and 30°C with start points 10°C and 12°C. It is worth noting that after calibration most of the data converges to the reference temperature as shown in Figure 3-5. The results of independently calibrating sixteen STTS751 temperature sensors within the temperature range from 10°C to 30°C are addressed in Table 3-1.

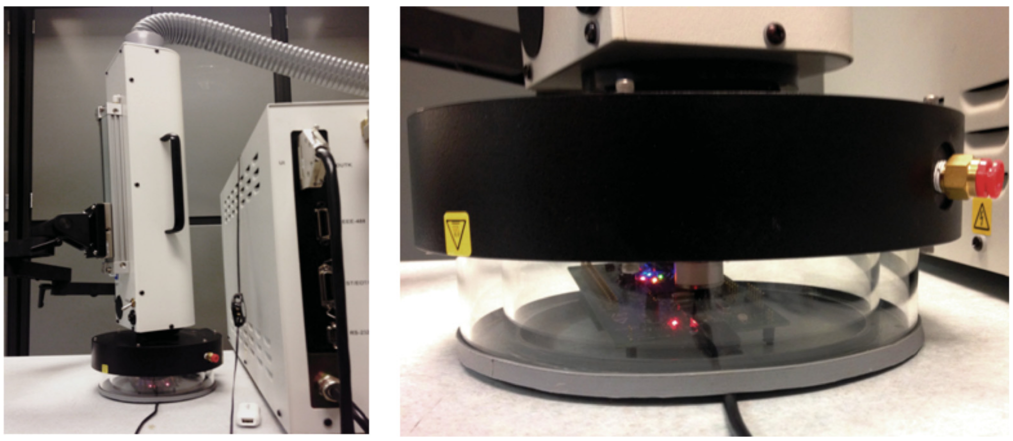

Figure 3-3: The Temptronic TP4500 with STTS751 temperature sensors under test

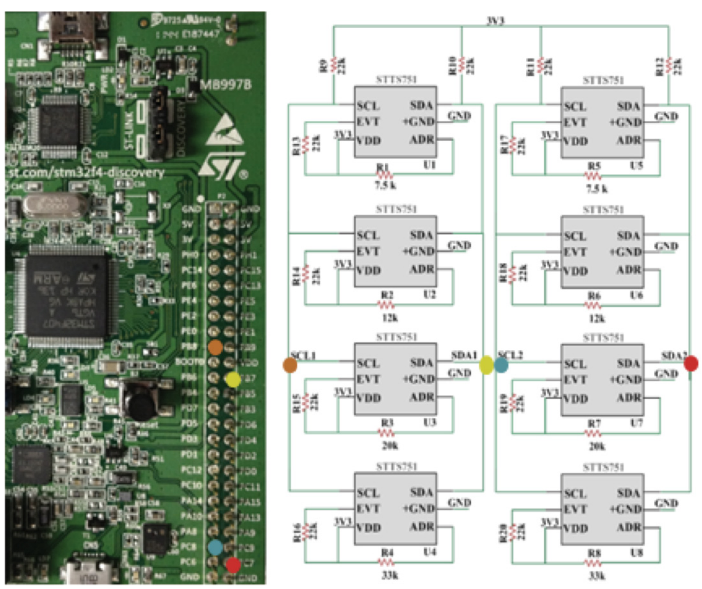

Figure 3-4: Schematic of the proposed multi-sensor system on the STMF432 board

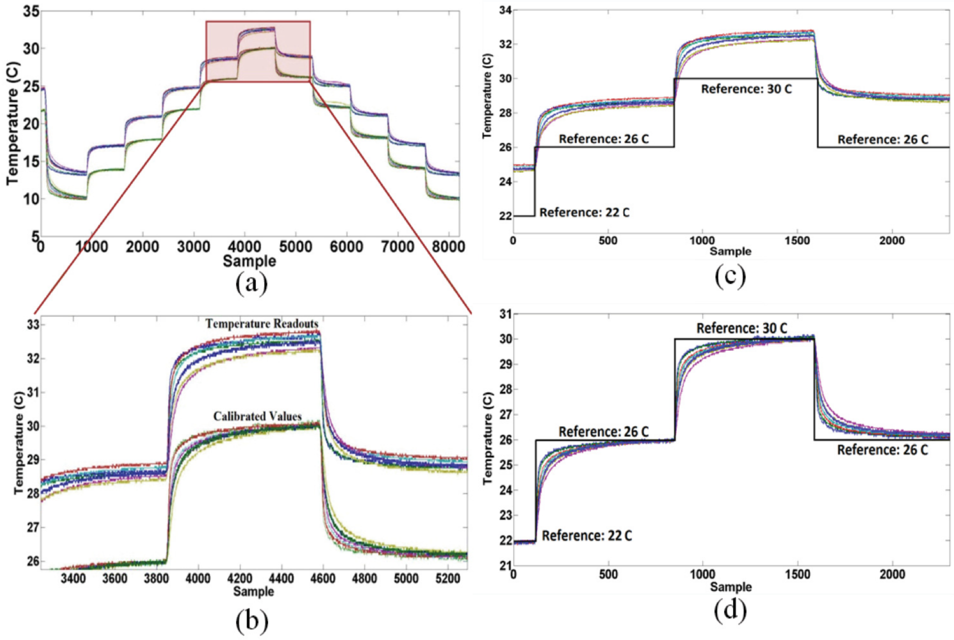

Figure 3-5: (a) Temperature readouts and calibrated values for eight sensors, when using a dual-slope ramp for the reference temperatures and start point $10^{o}C$, (b) zooming a portion of (a) for temperature readouts and calibrated values, (c) temperature readouts and references, (d) calibrated and reference values

Table 3-1: Optimal coefficients to calibrate our sensors.

	Sensors on board #1							
	1	2	3	4	5	6	7	8
Offset	-3.684	-3.829	-3.906	-3.901	-4.068	-4.029	-3.701	-3.901
Gain	1.034	1.042	1.034	1.038	1.053	1.055	1.037	1.044
	Sensors on board #2							
	9	10	11	12	13	14	15	16
Offset	-4.439	-4.610	-4.400	-4.729	-4.691	-4.672	-4.450	-4.685
Gain	1.074	1.076	1.063	1.068	1.070	1.074	1.070	1.076

Table 3-2: Confidence level of the error of 16 calibrated sensors w.r.t. the reference chamber over different intervals

Confidence Interval (^{o}C)	Confidence Level (%)
[-0.1,0.1]	45.32
[-0.2,0.2]	79.15
[-0.3,0.3]	97.58
[-0.4,0.4]	99.4
[-0.5,0.5]	99.4
[-0.6,0.6]	99.7
[-0.6535,0.6535]	100

We have also evaluated the confidence level of the calibrated results with respect to different confidence intervals as addressed in Table 3-2. As can be seen the confidence interval of $[-0.3^o, 0.3^o]$ covers most of the measurements, i.e., 97.58% of the data. Note that the calibration can be performed similarly for other temperature ranges as well. The maximum and minimum absolute values of error before and after calibration are also shown in Table 3-3.

To provide an acceptable fault-mode for the purpose of fault-tolerant data fusion, we require the statistical characteristics of noise. The results indicate that we can distinguish between the systematic bias/gain error and the random noise component of the error. It is observed that within the temperature range of 10°C to 30°C, there exists a small difference between the reference temperature and the calibrated data, which corresponds to the random noise. We expect the random noise to have a normal distribution. Hence, we have evaluated the difference between reference and calibrated temperatures for as many measurements as we can to get the distribution of this error. Namely, more than 100,000 reference temperature samples have been evaluated for all the 16 temperature sensors. The results have shown that such an error can be fitted into a normal distribution as depicted in Figure 3-2. In this figure, the fitted normal distribution corresponds to the log-likelihood value of 150.067, which indicates a good fit. We apply this normal distribution to represent noise in the fault-model of the proposed fault-tolerant data fusion approach, which is discussed in section 3.4.3.

3.4.2.1 Self-Calibration Results

The proposed blind recalibration methods have been applied on eight post-calibrated digital temperature sensors. Based on the uniform distributions of the original data, the sensor errors uniformly distributed in interval $[-20^{\text{o}}, 20^{\text{o}}]$, have been injected to simulate the decalibrated behaviors of sensors which is also added by the Gaussian noise in Figure 3-2.

The accuracy comparisons of three proposed methods are depicted in Table 3-4. As can be seen Algorithm 3-3 improves sum of mean square error by 23.44% comparing to the simple average method in Algorithm 3-2. Further, the proposed MMSE recalibration method delivers the superior precision compared to the other methods. The impact of the size of the dataset has been also evaluated in Figure 3-6. In particular, we have swept the number of samples (t) from 3000 to 9. As expected, experiments show that by decreasing the size of dataset, the accuracy of the recalibration will suffer.

Table 3-3: Maximum and minimum absolute values of error before and after calibration

Parameters	**Before Calibration**	**After Calibration**
Maximum Absolute Error (°C)	3.6	0.6535
Minimum Absolute Error (°C)	2.2	0.0015

Table 3-4: Error comparison of different recalibration algorithms on 8 temperature sensors

Number of decalibrated sensors	**Sum of Mean Square Errors**		
	Algorithm 3-2	Algorithm 3-3	Algorithm 3-4
1	0.0319	0.0098	**0.0094**
2	0.4561	0.3681	**0.1407**
3	2.111	2.0401	**0.7068**
4	4.8859	4.9768	**1.8748**
Average Improvement w.r.t. average		**23.44%**	**61.63%**
Average Improvement w.r.t. average based on correlation			**48.57%**

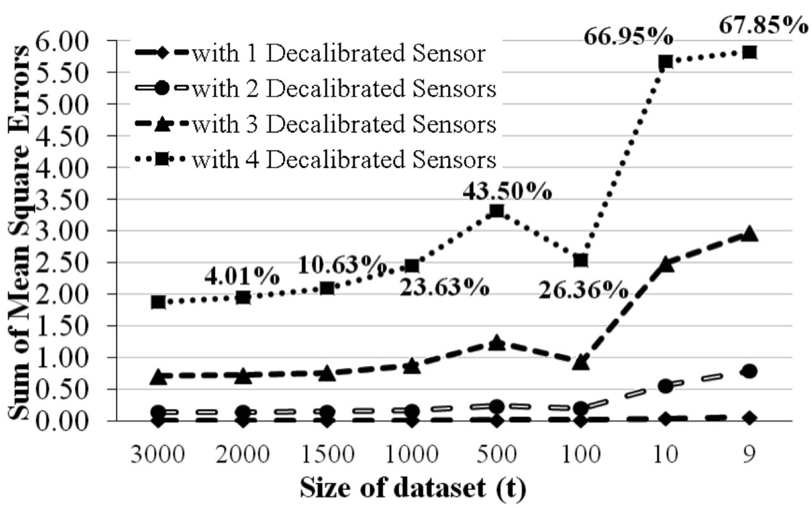

Figure 3-6: The impact of the dataset size (*t*) on errors in MMSE method

The percentages on Figure 3-6 show the accuracy reduction compared to the case where 3000 samples are used and there are four decalibrated sensors in the system. Therefore, it is important to choose an appropriate dataset according to the required accuracy for a given specific application. For example, when we reduce the number of samples in MMSE estimation, from 3000 to 1500, we need to tolerate the error of 10.63% where there are four decalibrated sensors. The presented methods make it possible to recalibrate multiple sensors fast. The run time of either Algorithm 3-2 or Algorithm 3-3 is about 0.7ms for single and multiple recalibrations. The MMSE method (Algorithm 3-4) takes about 1.8ms to estimate the reference, therefore, it is not only suitable to recalibrate sensors in real time, but also it can provide high accuracy. The proposed algorithms can be applied to maintain the correct operability of other sensors such as CGM, which current frequent recalibrations from blood reference are a tedious task.

3.4.3 Fault-Tolerant and Data Fusion Evaluation

In the first experiment we look into the MSE of the proposed data fusion compared to the normal average computation and the approach in [58] over different probabilities for a sensor to completely fail, i.e., the value of p_j in Eq. (3-9).

We have swept the value of p_j from 0 to 0.01, and the results are shown in Figure 3-7, where the number of sensors is set to 3. It is also notable that while the Algorithm 3-6 is performed only once and offline to find the MSE and the optimal threshold T, the data fusion technique in Algorithm 3-5 has to be performed online and periodically. As shown in Figure 3-7 the proposed fault-tolerant data fusion technique improves the MSE obtained by the approach in [58] by 34% in average. Furthermore, the optimal threshold in Algorithm 3-6 is obtained as T=0.235°C.

Observation: If the sensors are identical in terms of probability distributions and statistical characteristics, the optimal threshold obtained by the Algorithm 3-6 is independent from the number of sensors.

Hence, if the statistical characteristics of the sensors are identical to each other, which is mostly the case, e.g., in our system configuration, the optimal threshold obtained for the case with $n = 3$ (which can be obtained relatively fast according to the reduced dimensions for the computation of the integrals and MSE), can be used as the optimal threshold for the cases with $n > 3$ as well.

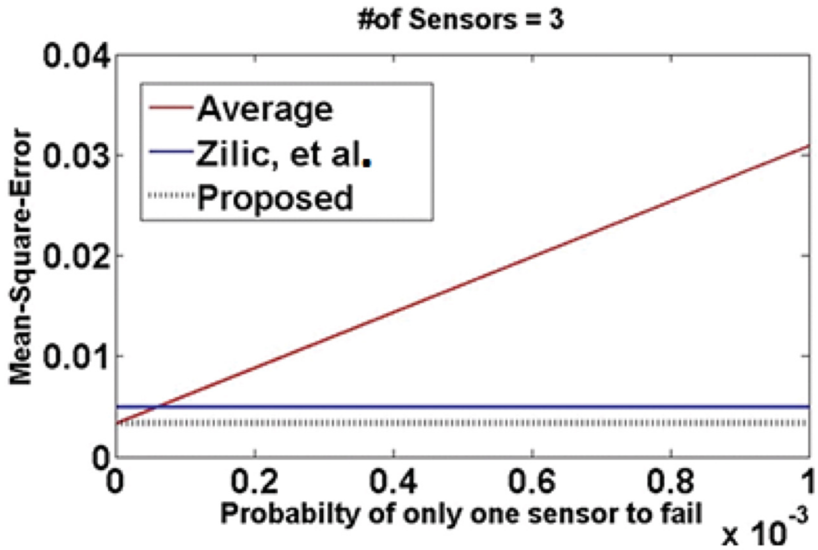

Figure 3-7: MSE analysis of three data fusion techniques versus different complete failure probabilities

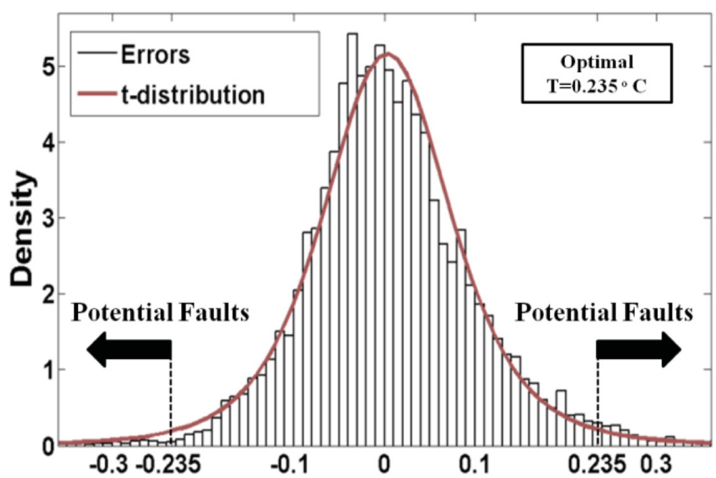

Figure 3-8: Finding the potential faulty sensors using the t-distribution derived from experimental measurements as well as the optimal threshold of $T = 0.235^oC$

Table 3-5: Wrong fault detection probability w.r.t. p_j for the system of 16 temperature sensors

p_j	**Probability of wrong fault detections**
0	0.1038×10^{-5}
0.001	0.1037×10^{-5}
0.01	0.1027×10^{-5}
0.1	0.0934×10^{-5}

An example is our multi-sensor system, which involves 16 temperature sensors. In the second experiment, we address the probabilities for a wrong fault detection using the proposed data fusion. Note that regarding the normal average computation, since faults are not being detected, there is no wrong detection. Furthermore, the approach in [58] is based on throwing away the sensor readout that is furthest from the average of others. Hence, the probability of wrong detections is equal to 1, when all the sensors are working fine. Even when the probability of a sensor to completely fail is relatively high, e.g., $p_j = 0.1$, the probability of a wrong fault detection for the approach in [58] is still high (more than 80% when $p_j = 0.1$).

We evaluate the probability of a wrong fault-detection for the proposed method, when the number of sensors n is set to 16, which corresponds to our system of 16 temperature sensors. The t-distribution derived from the experimental measurements, which is shown in Figure 3-1, is used for this purpose. Figure 3-8 highlights the wrong decisions when the sensors are in their normal operation mode (no faults) with $T = 0.235^oC$. Table 3-5 tabulates the final results including the probability of a wrong fault-detection with respect to the probability of a single sensor to fail, i.e. p_j. Note that since the proposed data fusion approach is performed periodically, it can resolve its previous wrong decisions within the next measurements.

3.5 Summary

In this chapter, the problems of non-blind calibration as well as jointly recalibrating the multi-sensor systems were addressed. In fact, early identification of faulty sensors through such technique and timely recalibrating the sensors can decrease the risk and cost in applications that deal with high risks such as patients' health. For instance, regarding closed-loop insulin control systems for managing glucose levels, sensor readouts should not only have a high accuracy, but also must be robust enough to recalibrate the sensors, quickly. The proposed generic self-recalibration approaches are particularly evaluated on a system of 8 temperature sensors. Among three analyzed methods, the MMSE resulted in the best accuracy in a reasonable short amount of time. We also presented a fault-tolerant data fusion technique aiming to minimize the MSE of sensor measurements in a calibrated multi-sensor system. The approach makes it possible to detect the potentially faulty sensors fast, while improving the accuracy of the final measurement. The statistical characteristics of the calibrated sensors are computed using thousands of measurements and finally, the proposed data fusion algorithm is implemented for the system to deliver both low MSE (high accuracy) as well as high fault-tolerance. The experiments compared the efficiency of the proposed data fusion technique in terms of MSE with the normal average computation [61] and the data fusion technique presented in [58].

Chapter 4

Analysis of the Chest Wall Compartments Movements

In the last decades, wearable technology appears to provide new services to empower people in every age to better manage their health concerns in a transparent manner. However, transparency is not only obtained through concealing technology in the design, physically, but when an accurate calculations and algorithms on the medical parameters are attained. In this chapter, a procedure is suggested to extract the respiratory parameters from modeling the anterior/posterior movements of the chest wall compartments during respiration function. Respiration rate, respiratory timing variables such as inhalation time (T_i) and exhalation time (T_e) are obtained via wearable sensing technology. In addition, the goal is to obtain an accurate technique based on motion sensors for calculating the phase shift between chest wall compartments to be used in remote detection of breathing problems. In the following, different body positions at rest are also determined by means of tilt measurement using a low-power 3-axis accelerometer.

4.1 Motivation

A reliable long-term monitoring of respiratory parameters and diagnosis of breath disorders at an early stage provides an improvement of medical act, life expectancy and quality of life while decreasing the costs of treatment and medical services. Therefore, a real-time unobtrusive monitoring of respiration patterns, as well as breath parameters is a critical need in medical researches.

There are different conventional methods for respiration signal and breath frequency measurements including spirometer, nasal thermocouples, impedance plethysmography, strain gauge for measurements of thoracic circumference, whole-body plethysmography [143], pneumatic respiration transducers, the fiber-optic sensor method [144], and ECG-based derived respiration measurements [145]-[147]. In spite of their accuracy, these methods are expensive and inflexible, which may bring discomfort to the patients and physicians. There is also Doppler radar [148] for respiration signal extraction; however, one major disadvantage of this method is the amount of DC offset introduced by the system that causes difficult demodulation. It is due to the low frequency of the vital signal, which is very close to the DC value of the signal [149]. In addition, most of the conventional methods are infeasible to be integrated in a wireless body sensor network. In a study comparing the accuracy of nurses' breathe rate measurements who were not aware of being tested, the accuracy was found to be poor, and nurses typically counted breathing for only 15 seconds [150]. Hence, it shows the problem of manual measurement that may cause due to constrained usage of respiratory rate monitoring where not specifically mandated. Applying motion sensors is of special interest to detect the small movements of the chest wall that occur during expansion and contraction of the lungs. In preliminary trials on hospital, it has been shown that with proper signal processing; this approach can produce results that match closely to the measurements of nasal cannula pressure [83]. Therefore, in this dissertation, we make use of 3-axis accelerometers which outstand among other types of Inertial Measurement Units (IMU) due to their stability characteristics, low energy consumption, robustness to environmental changes, as well as low cost. In addition, these miniaturized sensors are truly embeddable in different type of devices and items.

4.2 Accelerometer-derived Respiration Parameters

Discovering most frequent vital signs remotely, such as respiration rate has been in the interest of the medical research community in recent years. In this section, a procedure is described to estimate the respiration rate with accelerometer signal at rest positions considering the spirometer as our medical reference. In order to deliver high accuracies for the sensor measurements, we first perform a calibration technique using Least Square method proposed by [151].

4.2.1 3-axis Accelerometer Calibration

There exit different types of technological or hardware anomalies which may happen to occur on electronic devices. Due to decalibration or battery failures, wearable inertial sensors are subject to changes in the offset, scale factors, non-linearity or electronic noise among others [152]. Calibration, as a means of mapping raw sensor readings into the corrected values, can be used to compensate the systematic offset and gain. Note that when the gain and offset are both constant values and independent from the sensor measurements, then the calibration is translated into a linear curve-fitting function.

Generally, different special tools with specialists' experience are required for sensors calibration; however, a straightforward method to calibrate an accelerometer is performed at 6 stationary positions. We need to collect a few seconds of accelerometer raw data at each position. The misalignment of the sensor in these stationary positions will influence the calibration procedure. Therefore, to minimize the impact of misalignment, two boxes were used to help fix the module in different positions to obtain stable acceleration measures. In our setting, the boxes are put on a flat surface and the module was placed between two boxes where it faces of one box, and the other box was used to stop the module from gliding. The two boxes keep the module in a stationary position for at least 10 seconds. Then the least square method is applied to obtain the 12 calibration parameters. The sensor quality and criticality of the application determine the calibration frequency that can be manually performed. The calibration procedure can be formalized as follows:

$$[a_{x'}, a_{y'}, a_{z'}] = [a_x \; a_y \; a_z \; 1].\begin{bmatrix} acc_{11} & acc_{21} & acc_{31} \\ acc_{12} & acc_{22} & acc_{32} \\ acc_{13} & acc_{23} & acc_{33} \\ acc_{10} & acc_{20} & acc_{30} \end{bmatrix} \tag{4-1}$$

$$y = w.X \tag{4-2}$$

Where:

- Vector w is accelerator sensor raw data collected at 6 stationary positions,

- Vector y is the known normalized Earth gravity vector,
- Matrix X is the calibration parameters that is determined as below:

$$X = [w^T . w]^{-1} . w^T . y \tag{4-3}$$

The calibration matrix is calculated once, and after that, all samples of data will be multiplied by X to output the calibrated values. Our analysis is based on the acceleration signals recorded with a 3-axis accelerometer mounted on the subject's chest. The place of wearable sensor on the body has a direct effect on the accuracy of the algorithms, because different positions provide different signal patterns. In fact, in each breathing cycle the volume of the thoracic cavity is changed, caused by the displacements of the rib cage and diaphragm, therefore, in our experiments the sensor is worn on the chest, where can also provide more convenience compared to other locations such as suprasternal notch. In addition, it is among the top four selected placements derived from statistics on patient's perspective [153]. Accordingly, this location has practical benefits in our platform, since different estimated parameters such as tidal volume variability or quantitative feedback in our breathing therapy framework are closely depend on the chest wall motions during respiration cycle.

4.2.2 Respiration Rate and Time Parameters Estimation

Indeed, the normal breathing rate for a human being is usually between 0.2-0.3Hz and the maximum frequency is not likely to go over 0.7-0.8Hz [71]. Therefore, the breathing signal can be considered as a low-frequency signal, which must be filtered using a low-pass filter to remove the unnecessary and unwanted high-frequency components. To eliminate the disruption movements, the raw sensor data is filtered through a 10^{th} order Butterworth low-pass filter with cutoff frequency 1Hz. In order to estimate the respiration signal, first the estimated parameters are evaluated based on the airflow signal obtained from the spirometer. There was a negligible difference in calculating respiration rate via volume instead of flow signal. The signal characteristics of volume is much closer to acceleration signal. For example, when a subject holds his breathing, the flow signal drops to zero, while the accelerometer signal stays in the maximum inspiration point exactly the same as the volume waveform from the spirometer. In this way, we apply a numeric integration algorithm in which the trapezoidal rule was used to estimate the area under the flow curve shown

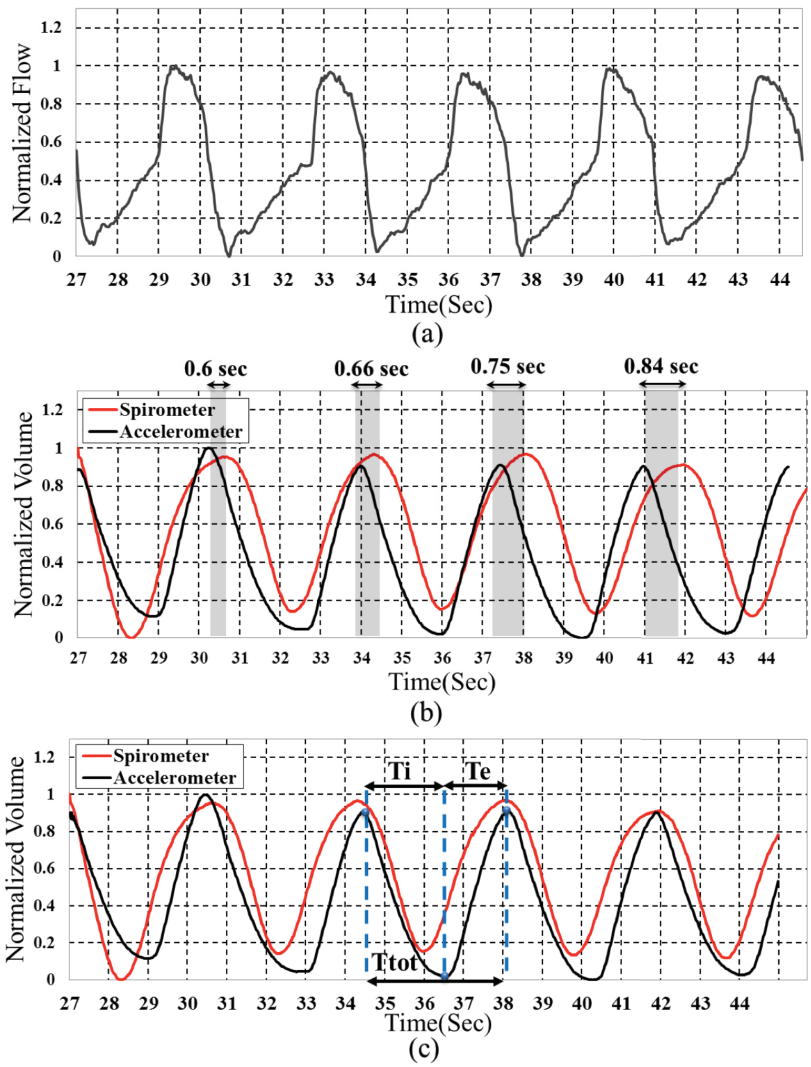

Figure 4-1: (a) The normalized flow of spirometer, (b) The cumulative error of accelerometer and spirometer normalized volume signals over time before resampling (c) Two signals after resampling procedure

in Figure 4-1 (a) and obtain the respiratory volume from the spirometer signal drawn in red in Figure 4-1 (b). These figures illustrate a part of volume signal for the normal breathing pattern of a 29 years old man. As can be seen, even though two signals seem similar, there is a cumulative error [84] over time affected on their synchronization. Indeed, this type of error on signals is due to different sampling frequencies. Although, the sampling rates of accelerometer and spirometer are both set to 50Hz, due to the architecture of the Inertial Measurement Unit (IMU), there might be a small difference between the sampling rate and measured frequency. Thus, to compare the respiration rate, it is essential to ensure that both signals have identical frequencies. For this purpose, after rational fraction estimation, we resample our data by an anti-aliasing low-pass FIR filter during the resampling process. In our experiments, the sampling rate of the accelerometer sensor was set to 50Hz, however; the data was logged with about 51Hz (measured frequency). With resampling process explained above, we could compensate the time lead about 0.02 per second. The solid black line in Figure 4-1 (c) represents the final signal after resampling procedure. Note that the system automatically checks the number of samples in each analysis window to find the measured frequency of the sensor. Now, the respiration rate can be computed based on the number of local maxima in the breathing signals per minute. In order to compare the correlation of respiration waves of accelerometer and spirometer as well as the respiration rate, the best starting points of two signals are obtained based on the peak value of their cross correlation. The Pearson correlation between the accelerometer and spirometer signals is calculated from the following equation.

$$R_{A,S} = \frac{x(\sum_{i=1}^{x} A_i S_i) - (\sum_{i=1}^{x} A_i)(\sum_{i=1}^{x} S_i)}{\sqrt{[x\sum_{i=1}^{x} {A_i}^2 - (\sum_{i=1}^{x} A_i)^2][x\sum_{i=1}^{x} {S_i}^2 - (\sum_{i=1}^{x} S_i)^2]}} \tag{4-4}$$

Where A and S denote the accelerometer and spirometer data with x samples, correspondingly. We have also calculated per breath inspiratory time (T_i), expiratory time (T_e), and total time of the respiratory cycle (T_{tot}) from the accelerometer-derived respiration waveform by peak and valley detections, described in Figure 4-1 (c). The applied peak/valley detector defined a customized threshold to decide whether each peak (or valley) is significantly larger (or smaller) than the local data. In fact, these time parameters are used to calculate the $I{:}E$ ratio defined as a ratio of the inspiration time to the duration of expiration ($I{:}E = T_i/T_e$). In healthy people, the expiration is about two to three times longer than inspiration resulted in the $I{:}E$ ratio from 1:2 to 1:3 [154]. In patients with breath problems e.g., COPD, the expiratory time is typically prolonged. This cause lower $I{:}E$ ratio, such as 1:4 or 1:5. A prolonged T_e or low $I{:}E$ ratio is a major sign of expiratory airflow obstruction [154]. This ventilation parameter is considered as an important feature in hyperinflation treatment [155]. Respiration rate and tidal volume are respiratory variables typically known to modulate Respiratory Sinus Arrhythmia (RSA). The impact of $I{:}E$ is studied in [156] which indicates that RSA can also be modulated by inspiratory/expiratory time ratio.

4.2.3 Body Position and Angle Calculation

Body position is an important parameter that must be considered for several breathing disorder problems. The method used in this chapter helps to identify the rest and sleeping positions with the representation of roll and pitch angles. For a stationary object, the pitch and roll angles can be obtained with 3-axis accelerometer [157]. We measure the tilt angles with trigonometric formulas as follows [151] (see Figure 4-2):

$$Pitch = \alpha = arctan\,(\frac{a_{x\prime}}{\sqrt{{a_{y\prime}}^2 + {a_{z\prime}}^2}}) \tag{4-5}$$

$$Roll = \beta = arctan\,(\frac{a_{y\prime}}{\sqrt{{a_{x\prime}}^2 + {a_{z\prime}}^2}}) \tag{4-6}$$

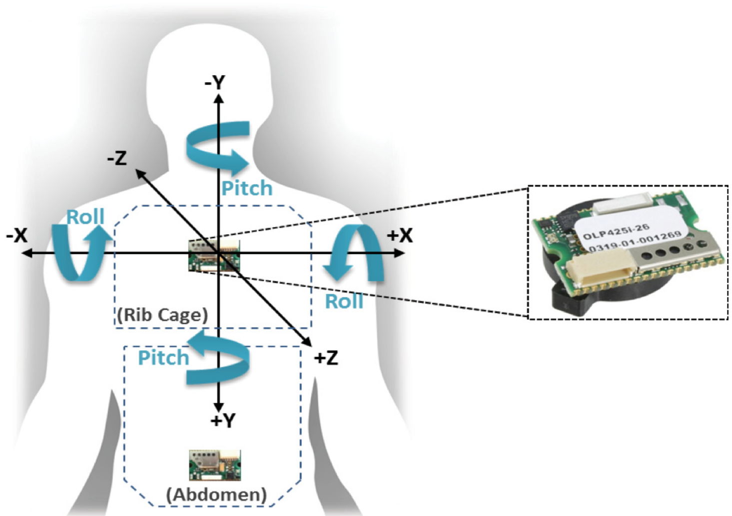

Figure 4-2: The accelerometer sensors' placements on the body and tilt angles

Table 4-1: pitch and roll angles for five different positions based on the sensor location

Postures	Angles	
	Pitch (Degree)	Roll (Degree)
Sitting	0°	-90°
Resting	0°	-45°
Supine	0°	0°
Left side	+90°	0°
Right side	-90°	0°

Where $a_{x'}$, $a_{y'}$ and $a_{z'}$ are calibrated data of 3-axis accelerometer. In this chapter, five different body positions are evaluated and the corresponding body angles are defined in Table 4-1.

4.2.4 Breath Synchronization Analysis

In this section, we analyze the synchronous and asynchronous breathing patterns with our accelerometer sensors. For this goal, the chest wall is modelled in two compartments: Rib Cage (RC) and Abdomen (AB) shown in Figure 4-2. Indeed, in healthy people, the inspiration occurs by cause of systematic actions of the diaphragm and intercostal muscles, which resulted in RC and AB expansion synchronously during spontaneous breathing, at rest. Asynchronous breathing, in contrast, is defined as the difference in time of expansion or retraction between the compartments of the chest wall [92][93]. However, in case of extreme phase difference, the movement among the compartments becomes opposite, and then the paradoxical movement occurs [93].

In this section, the phase shift between RC ($Acc1$) and AB ($Acc2$) is calculated based on the degree of opening of Lissajous figure or Konno-Mead loop on accelerometer-derived respiration signals [96]. The phase angle (θ) is measured in degrees (º), changing from 0º to 180º. 0º and 180º represent the perfect synchronous pattern and paradoxical movement of the chest wall compartments, respectively. In Lissajous figure, the movements of one compartment are plotted versus the excursion of the second compartment in an X-Y graph during a single respiratory cycle [158][159]. θ is defined in Eq. (4-7).

$$\theta = sin^{-1}\frac{m}{s} \tag{4-7}$$

Where s represents the per breath normalized volume of the signal on the X-axis and m is the distance between the two intercepts of the loop with the ordinate at abscissa equal to 50% of the volume of the signal on the Y-axis [160]. If the slope of the main diagonal of the loop is negative e.g. in paradox breathing (Figure 4-3 (c)), the phase angle is greater than 90 º, thus:

$$\theta = 180 - \vartheta, sin\,\vartheta = m/s \tag{4-8}$$

Here, after signal processing described earlier, the respiration signals derived from both sensors are normalized by $\frac{y_i - Min\,(y_{1:x})}{Max(y_{1:x}) - Min(y_{1:x})}$, where $i = 1,2, \dots, x$ and $y = Acc1$ or $Acc2$. Then the phase

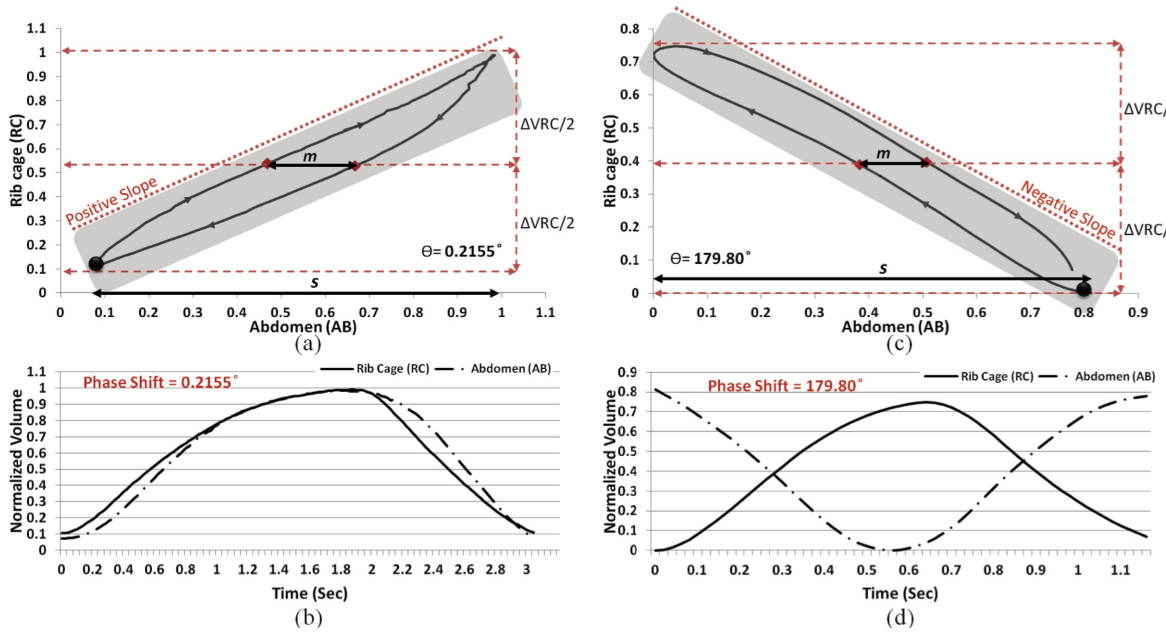

Figure 4-3: (a) The Lissajous figure of normal breathing of one subject, (b) The normalized volume derived from the accelerometer sensors mounted on the chest and abdomen in normal pattern, (c) The Lissajous figure of paradoxical breathing and (d) The normalized volume derived from the accelerometer sensors in paradoxical pattern

angles are calculated from their Lissajous figures as depicted in Figure 4-3. The figure shows the Lissajous figures of one of our subjects in resting position during his normal and paradoxical breathing. The solid dot corresponds to the onset of inspiration and arrows denote the direction of the loop. The phase shift between his RC and AB in this breath cycle for normal breathing is calculated as 0.2155º while in his paradoxical breathing shown in Figure 4-3 (c) and (d) it is calculated as 179.80º, which indicates a significant increase in the degree of rib cage and abdomen asynchrony. We have also investigated the impacts of posture and body angle on the synchronization of RC and AB in both normal and paradoxical breathing maneuvers in the experimental results section.

4.3 Experimental Results

To verify the effectiveness of our proposed techniques, the results are evaluated on different groups of subjects explained in the next section.

4.3.1 Test Setup

The experiments were conducted on two different groups, one with 10 healthy volunteers (5 males and 5 females) aged from 18 to 46 with (Mean ± SD) 30.70 ± 8.87 and second group with 8 healthy subjects (4 males and 4 females) aged from 18 to 46 with (Mean ± SD) 30.70 ± 8.29. They were instructed how to perform each breath exercise before their recording sessions. The experimental trials lasted for about 100 minutes per subject (4 breathing signals in 5 positions plus 5 breathing signals in one position) resulted in a total of about 800 different signals including accelerometers, spirometer and respiration monitor belts. We asked the first group to perform normal, fast, slow and paradoxical patterns, each for 1 minute (3000 samples), in five different body positions: sitting, resting, supine, left and right sides. We assigned a 3-minute rest interval after performing each pattern. Based on the definitions, for normal breathing we consider 12 to 20 respiration per minute (rpm), in slow pattern less than 12 rpm and for fast breathing, the subjects are asked to breathe more than 20 respirations per minute. For simulating paradoxical breathing, we instructed the subjects to reverse their abdomen movement in inhalation and exhalation. There was no limitation in the number of respiration for paradoxical breathing maneuver. In addition, the second group are coached on performing Bradypnea, Tachypnea, and Kussmaul patterns, each for 1 minute, Cheyn-stokes and Biot's each for 2 minutes in lying position. These patterns are associated with breathing problems explained in Chapter 2. For simulating apnea in Cheyn-stokes and Biot's breathing exercises, according to definition of apnea, we requested the participants to pause breathing for more than 10 sec. In our system, we used a 22.3×14.8mm, cB-OLP425 Bluetooth low energy module, which includes an ultra-low-power LIS3DH 3-axis accelerometer with 12-bit resolution. The sensor was mounted on the subject's chest in the middle of sternum region and secured by a soft and elastic strap, which is easy to use and comfortable to wear. The SPR-BTA spirometer shown in Figure 4-4 (a) is used as our reference, which measures the oral breathing. A nose clip was used to prevent nasal breathing during recordings. The removable flow head (22 mm ID/30 mm OD) makes it easy to clean and sterilize. The Go!Link USB sensor interface (bottom figure in Figure 4-4 (b)) is used as the data logger of our spirometer. In paradoxical and normal breathing experiments, our second sensor is attached on the subjects' umbilical region. In our tests, both sensors are sampling with 50Hz. Two Vernier Respiration Monitor Belts (RMB) are worn in the same locations of the body for breath synchrony validation. The belt is used with the Honeywell

(a) (b) (c)

Figure 4-4: (a) SPR-BTA spirometer with nose clip and flow heads [161], (b) Gas pressure sensor [162], and Go!Link [163], (c) Respiration Monitor Belt [164]

SSCMRNN030PAAA5 Gas Pressure Sensor (top figure in Figure 4-4 (b) and (c)) to measure human respiration. The belt simply strap around the chest and pumping air into the belt with the hand bulb provides pressure signals associated with the expansion and contraction of the chest during breathing. To summarize it up, we investigated four different breath models including normal, fast, slow and paradoxical patterns in five different positions in addition to five respiration patterns associated with breathing disorder problems resulted in total of 800 recording signals with accelerometers, spirometer and Respiration Monitor Belts.

4.3.2 Accelerometer-derived Respiration Signal Validation

In this section, first the correlation between the spirometer and accelerometer signal is calculated on 10 different subjects with various ages, each for three types of respiration listed in Figure 4-5 conducted in 5 different body positions. The assessments are repeated on another group of 8 subjects with five more types of breathing models in lying position shown in Figure 4-6. The results are brought in Table 4-2 and Table 4-3. It is worth noting that, based on the body movement mechanism in different positions; the major axes could be chosen either Z or Y depending on the postures. The mean value of the correlation coefficient between accelerometer and spirometer for all subjects and three respiration maneuvers in five positions is obtained 0.84 ± 0.03 summarized in Table 4-2. In other experiments with five breathing models in lying position, the average correlation is achieved 0.84 ± 0.06 and 0.84 ± 0.04 based on spirometer volume signal depicted in Table 4-3 and flow signal, correspondingly. The results demonstrate a very close correspondence between accelerometer and spirometer signals. The error rate e for respiration rate estimation in each window is derived from Eq. (4-9).

$$e = \frac{|f_{est} - f_{ref}|}{f_{ref}} \times 100 \tag{4-9}$$

Where, f_{est} and f_{ref} are the respiration frequency from accelerometer signal and reference spirometer, respectively. The overall average error rate is obtained 0.29% ± 0.33% (See Table 4-3) and 0.58% ± 0.84% versus spirometer volume and flow signals on five breathing patterns, respectively. As depicted in Table 4-3, the worst-case errors in all subjects occur in Bradypnea pattern where patients breathe slower than normal respiration rate. The results shown in Figure 4-7 (a) demonstrate that we could obtain the best accuracy for respiration rate measurement compared to [80], dual strain gauge [80], [72], [75]-[77] in lying position using a single accelerometer. In other words, the average absolute error ($|f_{est} - f_{ref}|$) of 0.05 ± 0.01 (bpm) is achieved based on all breath models and subjects. Therefore, the proposed technique can also surpass the previous methods in terms of average absolute error including [70] with 0.12 bpm, [79] with 0.5 bpm, [81] with 3 bpm, and [83] with 0.38 bpm depicted in Figure 4-7 (b). Besides, per breath time parameters through accelerometer and spirometer are calculated and listed in Table 4-4. The results of accelerometer-derived respiration parameters are validated against the spirometer results in terms of Mean Square Error (MSE) represented in Eq. (4-10). MSE is one of the most common reasonable criterion used to forecast accuracy in a predicted model [165].

$$MSE\ (T) = \frac{1}{n}\sum_{i=1}^{n}(\hat{T} - T)^2 \tag{4-10}$$

Where $\hat{T}$ is a vector of n predicted values with accelerometer signal, and T is the vector of timing values corresponding to the spirometer signal (our ground truth). The average MSE for three breathing types are listed in Table 4-4. The results also show the impact of body position on the correlation as well as time variables. For all subjects, the mean correlation on different positions and breathing patterns are more than 0.8 shown in the last column of Table 4-2.

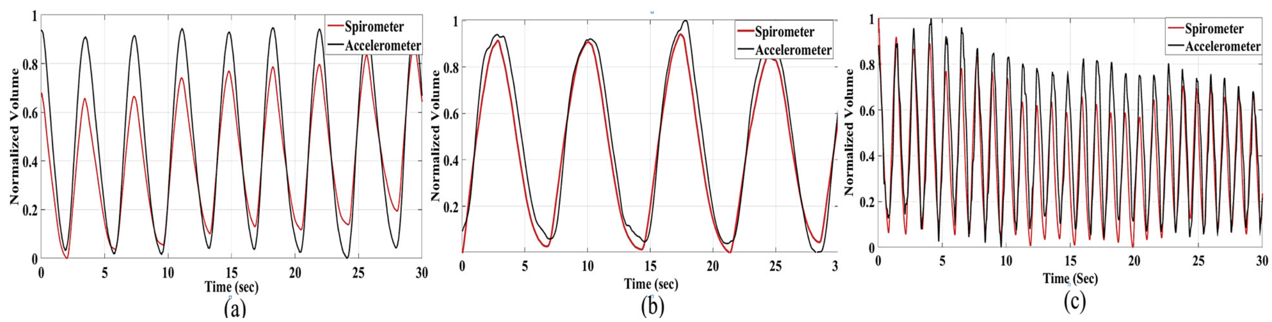

Figure 4-5: Accelerometer and spirometer signals for (a) Normal, (b) Slow and (c) Fast respiration patterns for one subject

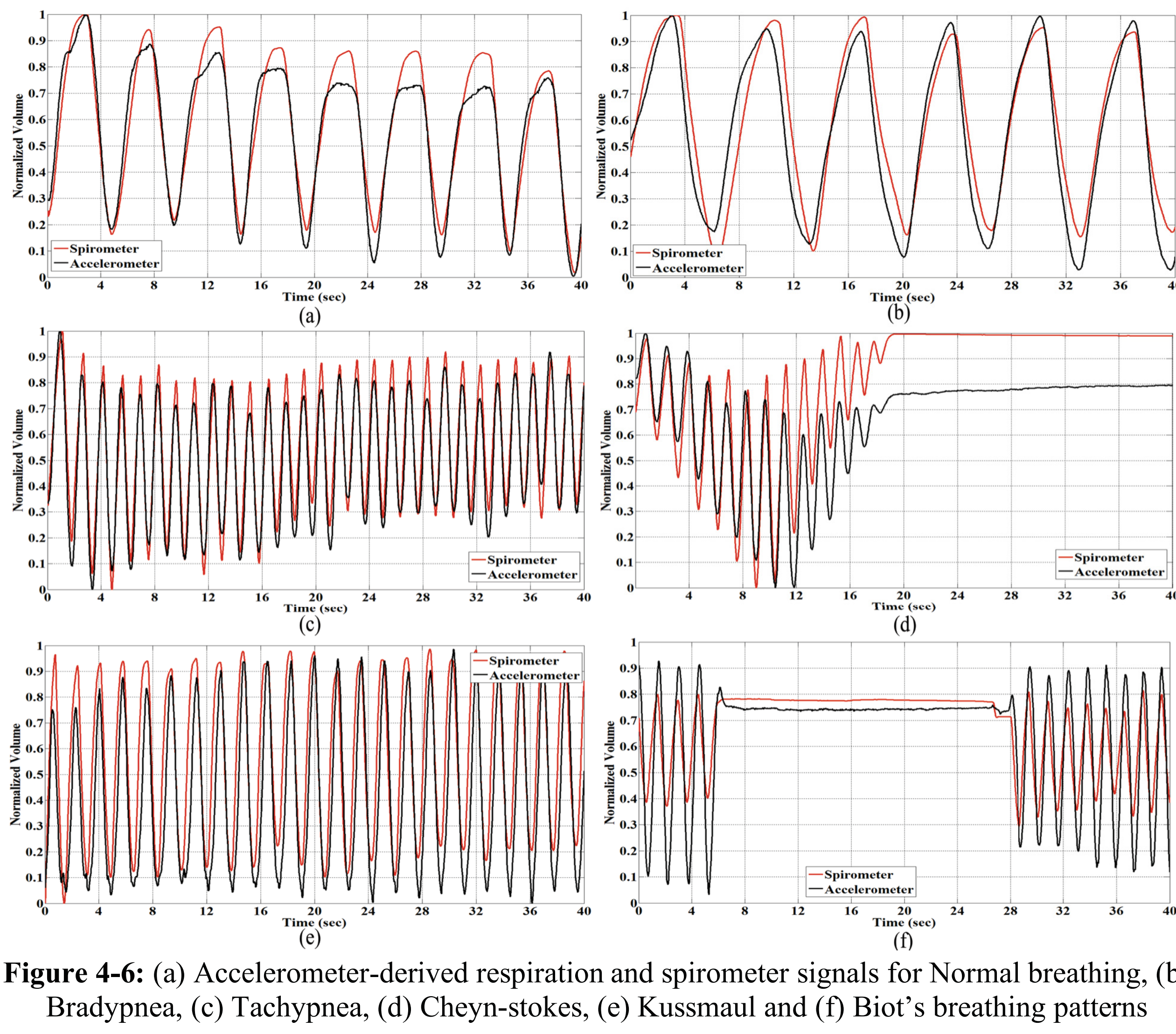

Figure 4-6: (a) Accelerometer-derived respiration and spirometer signals for Normal breathing, (b) Bradypnea, (c) Tachypnea, (d) Cheyn-stokes, (e) Kussmaul and (f) Biot's breathing patterns

Table 4-2: Correlation values of spirometer and accelerometer for all subjects and body positions

Subject ID	Gender /Age	Body Position															Average
		Sitting			Resting			Supine			Left side			Right side			
		Fast	Normal	Slow	Fast	Normal	Slow	Fast	Normal	Slow	Fast	Normal	Slow	Fast	Normal	Slow	
S1	F/46	0.97	0.85	0.91	0.79	0.71	0.74	0.91	0.80	0.83	0.78	0.80	0.72	0.79	0.72	0.97	0.82
S2	M/43	0.84	0.92	0.92	0.58	0.88	0.92	0.80	0.85	0.81	0.80	0.79	0.82	0.89	0.71	0.83	0.82
S3	F/37	0.82	0.89	0.97	0.92	0.93	0.95	0.72	0.76	0.74	0.74	0.77	0.93	0.85	0.70	0.76	0.83
S4	F/30	0.87	0.90	0.90	0.83	0.95	0.90	0.85	0.98	0.97	0.74	0.73	0.89	0.91	0.98	0.98	0.90
S5	F/29	0.83	0.96	0.63	0.90	0.98	0.92	0.97	0.97	0.97	0.68	0.56	0.81	0.83	0.89	0.96	0.86
S6	M/29	0.93	0.80	0.72	0.91	0.86	0.79	0.95	0.90	0.94	0.82	0.59	0.86	0.67	0.55	0.68	0.80
S7	M/28	0.86	0.95	0.93	0.63	0.86	0.63	0.75	0.92	0.77	0.91	0.84	0.87	0.90	0.88	0.72	0.83
S8	M/25	0.81	0.86	0.70	0.95	0.98	0.99	0.86	0.91	0.92	0.80	0.74	0.88	0.79	0.73	0.73	0.84
S9	F/22	0.94	0.91	0.96	0.88	0.87	0.94	0.86	0.95	0.95	0.78	0.80	0.82	0.70	0.78	0.96	0.87
S10	M/18	0.78	0.79	0.94	0.73	0.82	0.84	0.76	0.75	0.98	0.74	0.76	0.71	0.76	0.82	0.88	0.80
Average Correlation for all subjects with all conditions (Mean ± SD)																	**0.84± 0.03**

Table 4-3: Accelerometer-derived respiration rate errors versus spirometer with the correlation values

Subject ID	Gender/Age	Score	Respiration Rate Errors (%) vs. spirometer						Correlation with spirometer					
			Normal	Bradypnea	Tachypnea	Kussmaul	Cheyn-stokes	Biot's	Normal	Bradypnea	Tachypnea	Kussmaul	Cheyn-stokes	Biot's
S1	**F/46**	8	0.52	0.72	0	0.56	0.05	0.11	0.74	0.88	0.86	0.86	0.82	0.89
S2	**F/30**	8	0	1.51	0.54	0	0	0.11	0.96	0.93	0.76	0.78	0.82	0.74
S3	**F/29**	10	0.14	0.95	0.09	0.02	0	0.06	0.96	0.87	0.9	0.91	0.71	0.81
S4	**M/29**	9	0.06	0.51	0.3	0.18	0.07	0.03	0.95	0.89	0.77	0.83	0.73	0.87
S5	**M/28**	10	0	1.59	0.23	0.07	0.05	0.11	0.97	0.89	0.97	0.58	0.83	0.72
S6	**F/22**	9	0.16	1.14	0.24	0.06	0.16	0.11	0.97	0.94	0.96	0.68	0.75	0.68
S7	**M/24**	7	0.14	0.46	0.05	0.2	0.13	0.03	0.91	0.87	0.92	0.82	0.75	0.74
S8	**M/18**	10	0.22	0.74	0.34	0.58	0.34	0.08	0.82	0.98	0.78	0.94	0.93	0.77
Average		**8.875**	**0.16**	**0.95**	**0.22**	**0.21**	**0.1**	**0.08**	**0.91**	**0.91**	**0.87**	**0.8**	**0.79**	**0.78**

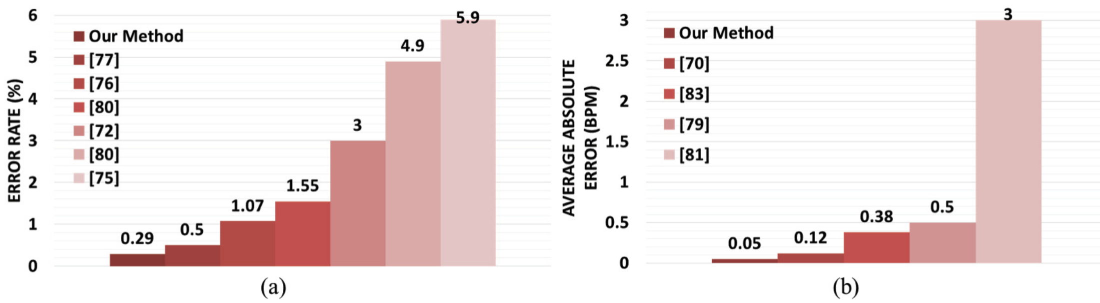

Figure 4-7: (a) Accelerometer-derived respiration rate error rates, (b) Average absolute error of accelerometer-derived respiration rate

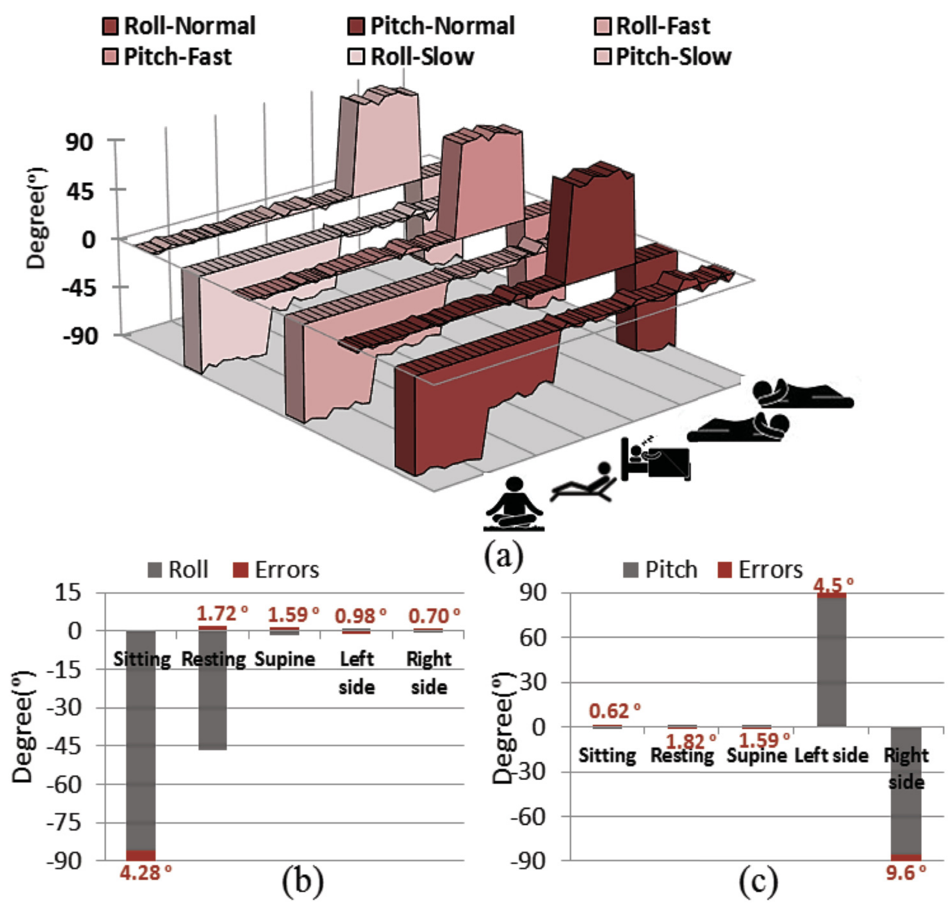

Figure 4-8: (a) Pitch and roll angles on three respiration patterns for all subjects in different body positions, (b) Average roll angles of all subjects and patterns for five different positions with absolute errors in degree (c) Average pitch angles of all subjects and patterns for five different positions with absolute errors in degree

Table 4-4: Average MSE of inspiratory time (T_i), expiratory (T_e), and total time of the respiratory cycle (T_{tot}) on three breath patterns derived from accelerometer vs spirometer and the pitch and roll angles during different body positions

Subject ID	Body Positions																				Average MSE T_i	Average MSE T_e	Average MSE T_{tot}
	Sitting				Resting				Supine				Left side				Right side						
	MSE T_i	MSE T_e	MSE T_{tot}	Pitch Roll	MSE T_i	MSE T_e	MSE T_{tot}	Pitch Roll	MSE T_i	MSE T_e	MSE T_{tot}	Pitch Roll	MSE T_i	MSE T_e	MSE T_{tot}	Pitch Roll	MSE T_i	MSE T_e	MSE T_{tot}	Pitch Roll			
S1	0.38	0.49	0.49	-1.00° -86.94°	0.42	0.55	0.03	1.69° -47.26°	0.08	0.08	0.06	2.53° -0.36°	0.01	0.01	0.01	87.21° -2.10°	0.01	0.01	5.4E-03	-81.51° 6.99°	**0.16**	**0.23**	**0.18**
S2	0.05	0.05	0.03	-0.77° -88.57°	0.02	0.02	0.00	3.89° -45.75	0.36	0.31	0.03	1.63° -2.85°	0.13	0.13	0.05	82.00° 5.79°	0.24	0.20	0.11	-87.73 -1.52	**0.16**	**0.14**	**0.04**
S3	0.02	0.04	0.01	0.56° -87.62°	0.02	0.01	0.00	3.53° -43.75°	0.14	0.26	0.12	2.00° -1.70°	0.09	0.08	0.02	85.16° 4.08°	0.33	0.18	0.14	-89.60° -0.38°	**0.12**	**0.11**	**0.06**
S4	0.19	0.20	0.09	-0.12° -83.87°	0.21	0.11	0.08	-0.87° -49.60°	0.08	0.07	0.03	-0.62° 1.23°	0.17	0.18	0.07	85.02° 3.54°	0.03	0.07	0.04	-84.82° -4.39°	**0.14**	**0.13**	**0.07**
S5	0.58	0.42	0.04	-2.12° -84.77°	0.11	0.08	0.08	0.33° -49.83°	0.02	0.01	0.02	4.07° -2.09°	0.50	0.67	0.21	85.89° 3.44°	0.07	0.10	0.06	-86.56° -2.48°	**0.26**	**0.26**	**0.08**
S6	0.29	0.30	0.12	0.18° -84.74°	0.07	0.08	0.01	1.27° -45.24°	8.96E-03	0.01	8.73E-03	4.66° -3.22°	0.15	0.13	0.15	86.68° -3.25°	0.23	0.19	0.06	-88.37° -1.52°	**0.15**	**0.14**	**0.08**
S7	0.03	0.05	0.06	-0.77° -84.19°	0.06	0.04	0.02	1.84° -45.36°	0.10	0.11	0.04	0.47° -1.36°	0.13	0.13	0.14	85.97° 1.12°	0.08	0.12	0.13	-85.09° -1.23°	**0.08**	**0.09**	**0.08**
S8	0.05	0.03	0.00	0.74° -85.16°	0.02	0.01	0.00	2.41° -43.35°	0.32	0.16	0.08	0.98° -2.04°	0.11	0.09	0.01	86.21° -3.76°	0.25	0.22	0.03	-84.99° -1.98°	**0.15**	**0.10**	**0.02**
S9	0.04	0.03	0.04	-1.02° -84.46°	0.01	0.01	0.01	2.57° -48.56°	0.18	0.16	0.01	-1.56° 0.10°	0.32	0.27	0.29	87.33° -2.29°	0.11	0.13	0.02	-84.32° -4.94°	**0.13**	**0.12**	**0.07**
S10	0.23	0.06	0.15	-1.92° -86.89°	0.01	0.02	8.56E-03	3.36° -48.49°	0.11	0.13	0.03	1.76° -3.58°	0.68	0.91	0.05	87.83° -2.09°	0.07	0.08	9.63E-03	-88.34° -0.57°	**0.22**	**0.24**	**0.05**
Average	**0.19**	**0.17**	**0.10**	**-0.624°** **-85.72°**	**0.09**	**0.09**	**0.02**	**2.00°** **-46.71°**	**0.14**	**0.13**	**0.04**	**1.59°** **-1.59°**	**0.23**	**0.26**	**0.10**	**85.93°** **0.45°**	**0.14**	**0.13**	**0.06**	**-86.13°** **-1.20°**	0.16	0.16	0.07

The goal is to provide a model in such a way that when its outputs are analyzed, the MSE is close to zero. The average MSE obtained from all subjects and postures are 0.16, 0.16 and 0.07 for T_i, T_e and T_{tot}, correspondingly. Therefore, the predicted accelerometer-based time parameters are very close to the spirometer observations, as evidenced by the small MSE. As described earlier, another potential application of the presented remote monitoring respiratory platform is the body position tracking. In our experiments, the subjects were asked to stay at specific angles described in Table 4-1 for different body positions.

The average results of their body angles for slow, normal and fast patterns at the end of each experiment are shown in Table 4-4. Since the subjects are kept in specific positions during the experiment, our system reports 3.62º average displacement in the pitch and 1.85º in the roll angles which are negligible for body position detection at sleep or rest conditions. These error values are calculated based on the MAE on all subjects and patterns. The pitch and roll angles on normal, fast and slow breath patterns for all 10 subjects are presented in Figure 4-8 (a). As an example, it could be observed that switching from sitting to rest position, angle β decreased in average from -85.72º to -46.72º (Figure 4-8 (b)) while angle α almost kept 0 degree (changing from -0.62º to 1.82º). Similarly, angle α started to increase in positive range (in average from 1.59º to 85.50º) when the subject changes his position from supine to left side shown in Figure 4-8 (c).

4.3.3 Results of Breath Synchronization Analysis

In this section, we have analyzed the accelerometer-derived respiration signals from both rib cage and abdomen, simultaneously. The impact of the body positions on RC and AB movements have been evaluated, as well. Different studies show the importance of body posture on RC and AB movements. For instance, according to [166], in approximately one-half of the COPD patients, the RC and AB paradox was noticed while sitting. In contrast, in supine position, the rib cage paradox disappeared which resulted from the improvement of the diaphragm mechanism. Therefore, in this study we aim to calculate the phase shift between RC and AB with low-cost and portable sensors along with high accuracy and performance. Here, we choose three different breaths from each individual in paradoxical and normal breathing maneuvers. Note that, since we have $\theta = 0$º and $\theta = 180$º for synchronous and paradoxical breathings, we test these two models in our system. The average phase shift measured from the Lissajous figure for different postures are shown in Figure 4-9 (a) and (c).

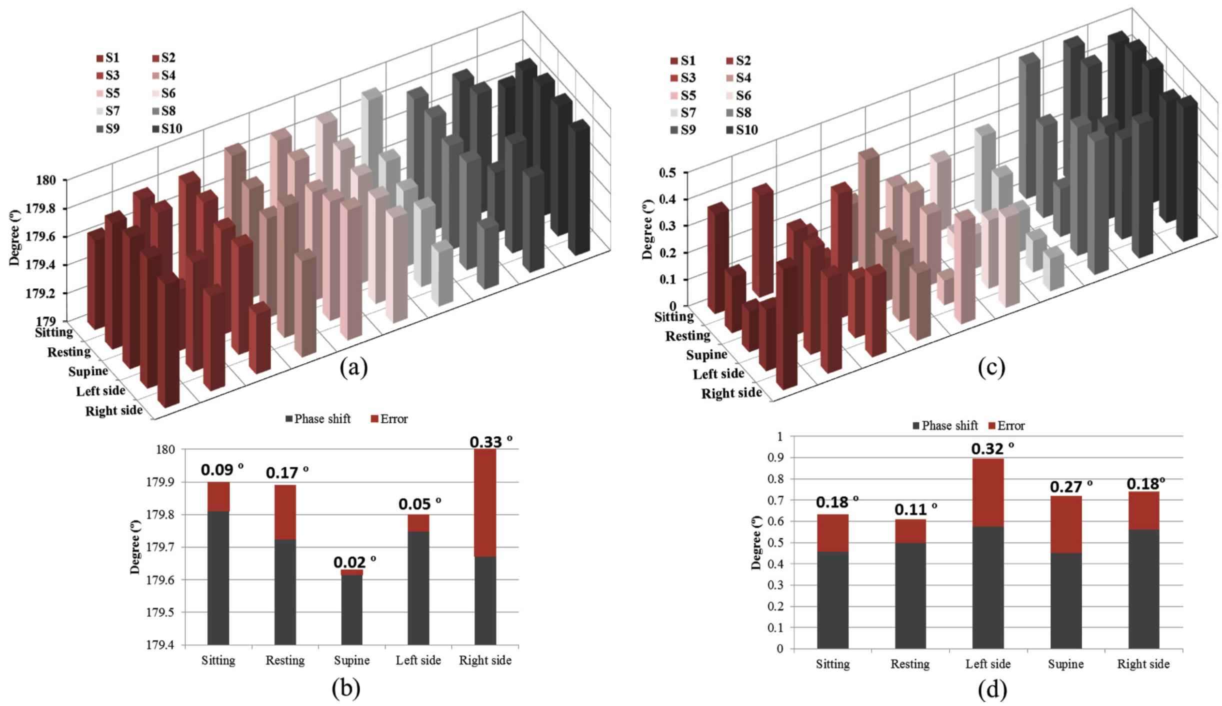

Figure 4-9: Average θ (a) For different body positions on three selected paradoxical breath cycles for all subjects (b) On all subjects for different body positions (c) For different body positions on three selected normal breath cycles for all subjects (d) On all subjects for different body positions

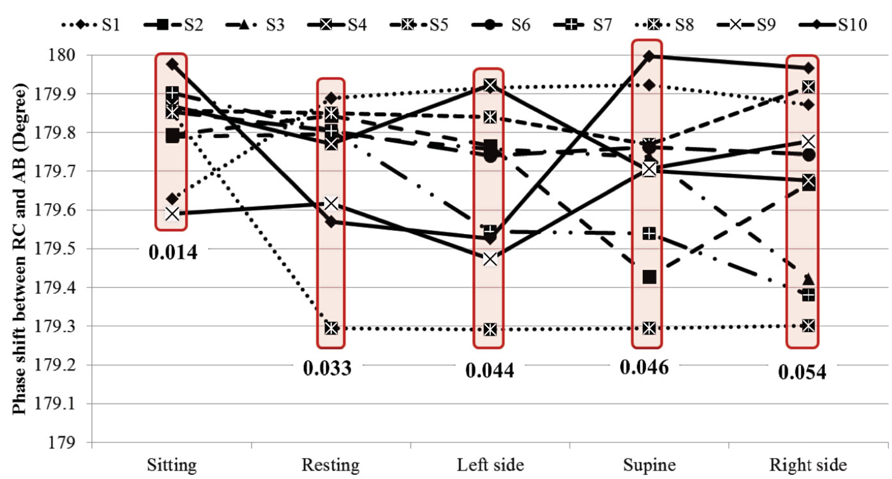

Figure 4-10: Phase angle between RC and AB compartments of different positions with the variances

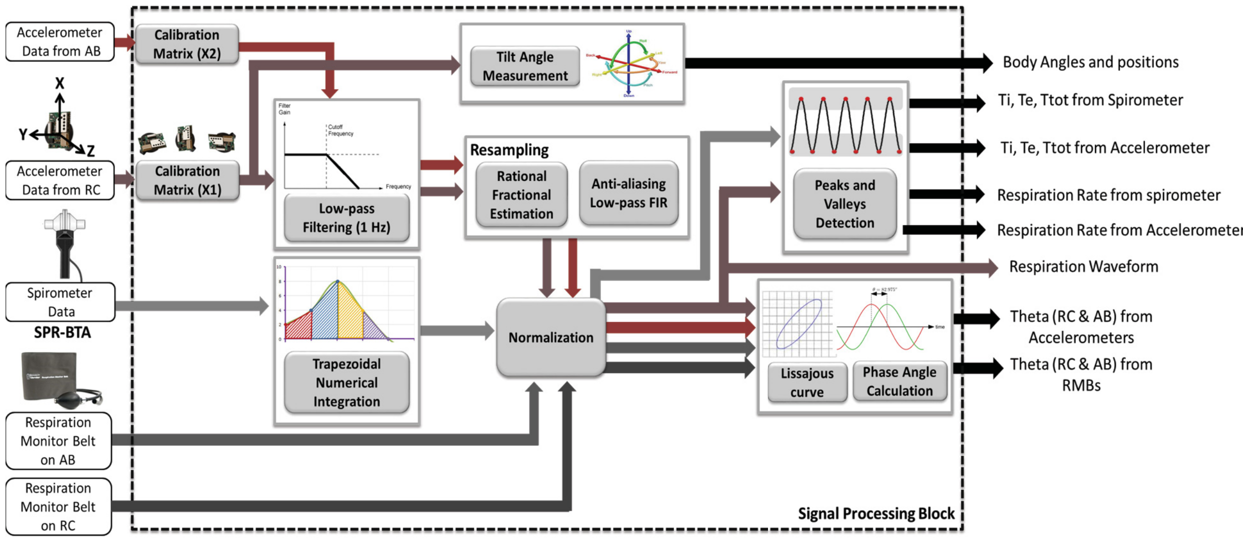

Figure 4-11: The overall procedures proposed in this chapter

The overall error for paradoxical experiments in all conditions versus the RMBs is 0.13º ± 0.12º derived from $|\theta_{RMB} - \theta_A|$ where θ_{RMB} is the calculated phase shift from two RMBs and θ_A is the estimated shift angle from accelerometer signals (see Figure 4-9 (b)). Similarly, for normal breathing in which we expect to have $\theta = 0$º, the average measured error in all body postures and subjects is obtained 0.21º ± 0.08º shown in Figure 4-9 (d). The results show that using two accelerometer sensors reliably estimates phase shift from the rib cage and abdomen motions. Figure 4-10 represents the phase angle between RC and AB compartments of different positions for 10 subjects. In this assessment, the effect of posture on the changes of the phase angles is discussed based on their variances depicted in Figure 4-10. It is observed that, in case of performing paradoxical test, the greatest variability is belong to the right side position while in sitting position all subjects have very close phase angles resulted in the least variability value. Finally, to evaluate the usability and flexibility of the proposed system, we asked our subjects to provide us a number between 0 and 10 to score the ease of use and flexibility of our system. The results are depicted in Table 4-3. The average score is obtained 8.875, which demonstrates the comfort and flexibility of the proposed intelligent system while giving more credits to accelerometer-based approaches as a simple and cost effective solution for m-health applications.

4.4 Summary

In this chapter, we discussed about estimating different parameters in a real-time respiration monitoring platform. Indeed, the proposed system is able to achieve and monitor different critical respiratory parameters with prominent benefits of cost, convenience, patient comfort and quality of service. We showed that there is a very close correspondence of the accelerometer-derived respiration waveform and spirometer data in terms of both correlation and three timing variables. Furthermore, the platform is capable of tracking the body position and tilt angles during rest positions and sleep. Since changing body position induces differences in the chest wall behavior, the impact of different postures on rib cage and abdominal asynchrony with different subjects have been investigated. The overall procedures are summarized in Figure 4-11.

Chapter 5

Tidal Volume Variability Estimation in an Emergency System

In this chapter, an intelligent system capable of measuring Tidal Volume variability (TV_{var}) via a wearable sensing technology is proposed. This system is designed particularly to help in diagnosis and treatment in people with pathological breathing e.g. respiratory complications after surgery or sleep disorders. Furthermore, since it is essential to detect the critical events caused by sudden rise or fall in per breath tidal volume of the people, a technique is provided to automatically find the accurate threshold values based on each individual breath characteristics.

5.1 Motivation

The accurate and precise detection of human respiration parameters poses several complex challenges. Although it might seem trivial at the first glance, the complexity and diversity of breathing models make truly difficult to elaborate a clear definition of them. In fact, the way people breathe varies from person to person. Therefore, there exists the need of an effort to collect rich general-purpose datasets as it occurs in other research fields such as activity recognition and computer vision. With the lack of complete datasets, the task of reproducing research turns to be quite difficult, which is found to be crucial in a research discipline. Therefore, in this part of this thesis, an appropriate dataset with motion sensors is provided on which the system will be evaluated. The use of a tri-axial device allows the inclination changes to be measured regardless of the body orientation. In fact, during a normal respiration, in each breathing cycle the volume of the thoracic cavity is changed, resulted from the displacement of the rib cage and diaphragm that is closely correlated with the tidal volume variability.

The measurement of tidal volume variability requires devices such as spirometer or pneumotachometr connected to the patient with a mouthpiece and nose clip or face masks. Indeed, the patients might have to wear nose clips during the procedure to prevent air leakage from the nose and they should breathe from the mounts with sealing their lips around the mouthpiece. These types of equipment are uncomfortable, and may cause a sensation of smothering [167] whereas they are impractical and not easy-to-use for long time monitoring or during sleep, especially for babies and children. The spirometers are mostly used in Pulmonary Function Test (PFT), which has to be conducted at the bedside, in a physician's office, or in a pulmonary laboratory under the expert’s supervision. Even though this type of test is short in time, patients may become lightheaded or dizzy after the test. Therefore, a monitoring method with simple setup and good accuracy for remotely estimating TV_{var} on a breath-by-breath basis is crucial. The study in [168] shows that an increase in children tidal volume variability is a better sign of opioid-induced respiratory depression than decreased respiratory rate. It is due to the fact that an increasing in TV_{var} is 10 times of a drop in respiratory rate. Besides, rising in TV_{var} also correctly predicts respiratory depression twice as often as decreased respiratory rate.

Indeed, the advantages of tidal volume variability monitoring as an indicator of impending respiratory depression are that TV_{var} is more sensitive than the respiratory rate and the magnitude of the changes is larger. It is worth noting that, the tidal volume variability is independent of age-related variations unlike respiratory rate [169]. Figure 1-4 shows the tidal volume variability and respiratory rate along with increasing doses of remifentanil in a typical patient. Remifentanil is a strong ultra-short-acting synthetic opioid analgesic drug, which is given to the patients during surgery to relieve pain and as an adjunct to an anaesthetic. In Figure 1-4 the patient was given 5 doses of remifentanil starting with 0.04 µg/kg/min and ending with 0.127 µg/kg/min. [169] demonstrates that an increase in tidal volume variability correctly identified that the next dose would cause respiratory depression in 41% of patients. The respiratory rate less than 10 breaths per minute correctly identified imminent respiratory depression in only 22% of the patients. Furthermore, TV_{var} increased by 336% over baseline during the penultimate dose and by 668%

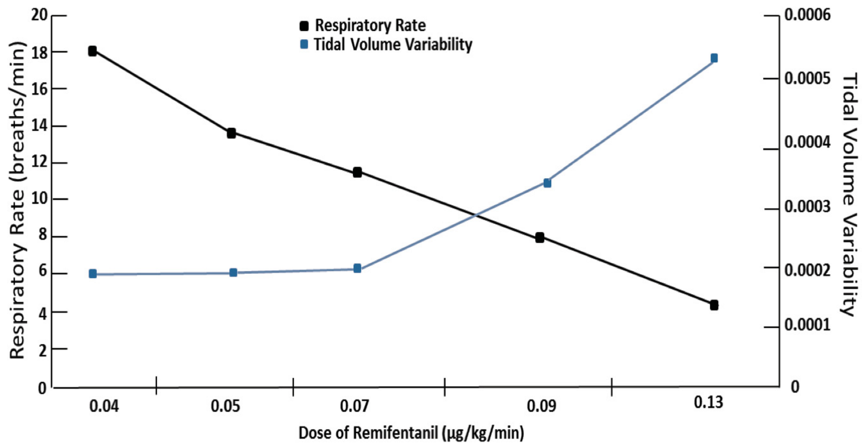

Figure 5-1: Tidal volume variability and respiratory rate versus the dose of remifentanil of a typical patient [169]

during the last dose. However, the respiratory rate, in contrast, decreased by 32% during the penultimate dose and by 56% during the last dose [169].

It is also well known that severe lung impairment in Cystic Fibrosis (CF) may compromise respiratory muscle function at rest. Patients with pulmonary disease caused by CF are known to have changes in their breathing pattern at rest. Hart *et al.* [170] reported these changes, specifically by a rapid rate and low tidal volume pattern associated with further impairment of gas exchange. Hence, monitoring of the tidal volume changes provides early identification and timely treatment of exacerbations with decreasing the hospital admissions, disease costs and slow deterioration.

As a method of improving patient care systems, hospitals often utilize patient monitoring and alerting systems in which the patient data stream is rapidly analyzed to recognize the emergency situations. The notifications regarding the presence of these critical events can come in the form of reminders or alerts. In this chapter, a new approach is proposed to find the appropriate threshold values based on respiration characteristics without the need of expert input. Therefore, this technique has significant potential to provide wide and positive effects on clinical care, in the future.

5.2 Tidal Volume Variability Estimation

In this section, we introduce a new method to accurately estimate TV_{var} with a single accelerometer from outside of medical centers. According to study in [74], the breath volume is equal to a corresponding change in the compartmental volume of the torso which is found to be fairly accurately represented by a changes in the cross sectional area of the chest during a breath cycle. So, in our experiments the accelerometer is attached on the chest to measure the inclination changes, which are closely correlated with tidal volume variability. In addition, we focus on providing an efficient technique to obtain TV_{var} in stationary positions, because people spend up to one-third of their lives at sleep and rest positions. This number grows for patients whom the respiratory condition during rest positions has an important role in their health management. The respiration signal obtained quite precisely from a calibrated accelerometer sensor in Chapter 3. Subsequently, the tidal volume variability is assessed based on the estimated volume signal. To eliminate the impacts of the postures, first we rescale the respiration signal to scale the range in [0, 1] and then calculate the per breath tidal volume. Indeed, this technique makes the breath volume to be independent of body position. The following notations are used through the rest of this section:

Acc: Normalized accelerometer signal after signal processing proposed in Chapter 3,

TV_{var}^{i}: Tidal volume variability of the i_{th}window,

TV_i: Tidal volume of the i_{th} breath cycle after signal normalization,

t: Window size for linear regression,

b_i: i_{th} breath (inhale) in each window,

p_i, v_i: i_{th} peak and valley values respectively.

The spirometer and accelerometer respiration signals are first normalized and then the volume of each breath is calculated from Eq. (5-1) shown in Figure 5-2. Steps 2 to 3 of Algorithm 5-1 show the procedures for obtaining TV_i for n inhales.

$$TV_i = p_i - \frac{(v_i + v_{i+1})}{2} \tag{5-1}$$

The calculated volumes are linearly fitted with different window sizes to obtain the trend of oscillations for both spirometer and accelerometer depicted in lines 5-9 in Algorithm 5-1. The window size refers to the number of breaths to obtain the tidal volume trend. In $\boldsymbol{fit}$ function (line 6 in Algorithm 5-1), we make use of the linear least square curve fitting for obtaining TV_{var} in each window as follows:

$$TV_{var} = \frac{t\sum_{i=1}^{t} b_i TV_i - (\sum_{i=1}^{t} b_i)(\sum_{i=1}^{t} TV_i)}{t\sum_{i=1}^{t} b_i^2 - (\sum_{i=1}^{t} b_i)^2} \tag{5-2}$$

Algorithm 5-1

$\boldsymbol{tidalVolumeEstimation}\ (Acc, t, TV_{var}^{1:\left\lfloor\frac{n}{2}\right\rfloor})\{$

// ***Inputs***: Acc, t // ***Output***: $TV_{var}^{1:\left\lfloor\frac{n}{2}\right\rfloor}$

1- $[p_{1:n}\ v_{1:n+1}] = \boldsymbol{peaksValleysDetection}(Acc)$; /* $peaksValleysDetection$ function extracts the peaks and valleys amplitudes */

2- $\boldsymbol{for}\ (i = 1;\ i \le n;\ i++)$
3- $\quad TV_i = p_i - (\frac{v_i + v_{i+1}}{2})$;
4- $i = 1;\ j = 1;$ /* Initialize the boundary*/
5- $\boldsymbol{while}\ (j + t - 1 \le n)\{$
6- $\quad TV_{var}^{i} = \boldsymbol{fit}(\ TV_{j:j+t-1}, t)$; **/*** The regression coefficient derived from the linear polynomial curve fitting function*/
7- $\quad i = i + 1;$
8- $\quad j = j + 2;\}$ /* Sliding window with $t - 2$ overlap*/
9- ***return*** $TV_{var}^{1:\left\lfloor\frac{n}{2}\right\rfloor}$;}

Here, TV_{var} is obtained based on the slopes (regression coefficients) of the linear fits for window size t. The window size should be chosen wisely based on the require sensitivity prescribed by the doctor. TV_{var} must be set to minimize the Sum of Square Error (SSE) function, which is defined as follows:

$$SSE = \sum_{i=1}^{t} (TV_i^{ref} - TV_i^{est})^2 \tag{5-3}$$

TV_i^{ref} is the calculated normalized tidal volume from Eq. (5-1) and TV_i^{est} refers to the estimated normalized tidal volume with least square technique. The proposed tidal volume estimation algorithm is also outlined in Figure 5-3. It shows about 42 sec of the accelerometer and spirometer signals of Biot's respiration for a 29 years old female. Per breath tidal volumes are first obtained from the normalized signals in Figure 5-3 (b) and (f). Then in Figure 5-3 (c) and (g), the least square fitted lines of each window as well as their slopes are shown while the window size is set to 3 and incremented by 2. Finally, TV_{var} is obtained as Figure 5-3 (d) from accelerometer sensor and (h) from SPR-BTA spirometer.

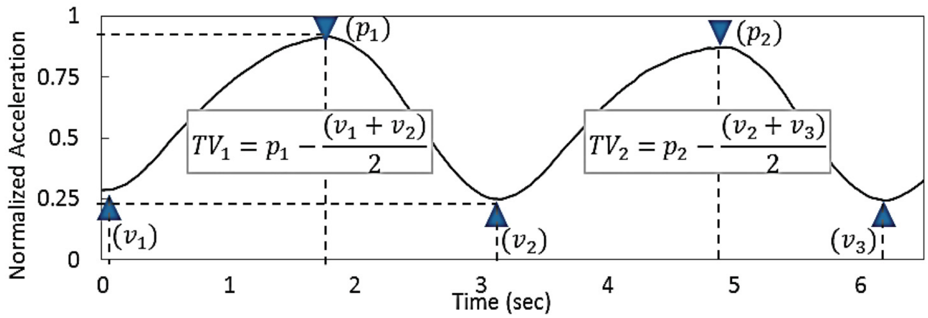

Figure 5-2: The tidal volume calculation after signal normalization

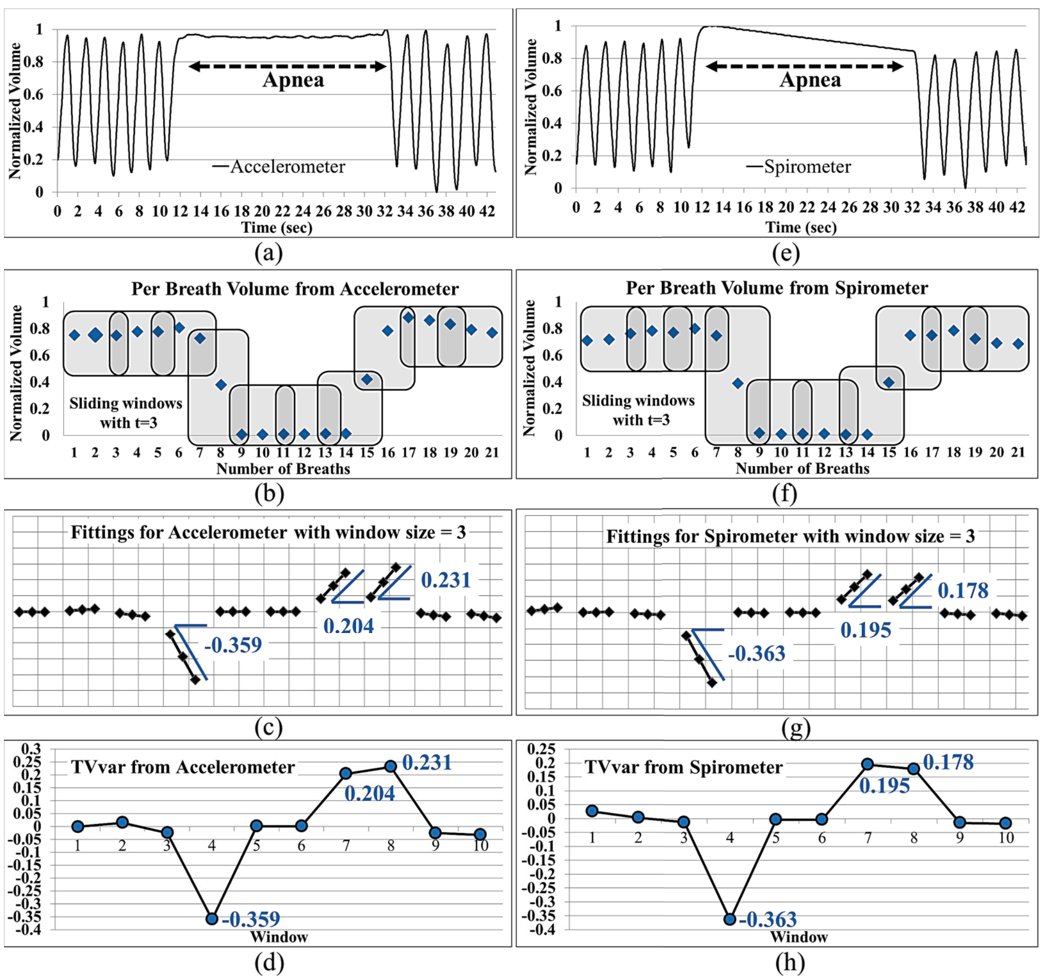

Figure 5-3: (a)-(d) The proposed procedures for tidal volume variability estimation with accelerometer signal, (e)-(h) The proposed procedures for tidal volume variability estimation with spirometer signal

Indeed, it indicates that there are negative and positive peaks of tidal volume in the 4th and 7th windows, respectively. These changes are due to the rapid respiration epochs followed by regular periods of apnea (Figure 5-3 (a) and (e)) in Biot's respiration pattern.

5.3 Dynamic Threshold Adjustment & Alarm Generation

Continuous respiration monitoring with high sensitivity for detection of critical events is essential. In this section, a new method is proposed to detect the critical points of tidal volume variability using Symbolic Representation of Time Series [171] in real-time. This method can be included in the platform to provide immediate feedback mechanism for round-the-clock breathing monitoring. Therefore, in case of sniffing a problem, it activates the sound alarm systems immediately or sends an email or SMS alert to the caregiver, family members or physicians.

People have different breathing characteristics such as rate, volume, tidal volume variability and pattern, which result in various threshold values for the recognition of an alarm. In this thesis, we apply SAX with a new segmentation technique in order to dynamically find the accurate threshold values based on each individual's breath characteristics in a short amount of time (~0.2 sec). The main goal is generating real-time alert based on monitoring the tidal volume variability if the condition of the patients are not suitable to make a call.

5.3.1 Symbolic Aggregate approXimation (SAX)

Lin *et al.* [171] introduced the Symbolic Aggregate approXimation (SAX) which allows a time series C of length n to be represented in a w dimensional space by a vector $\overline{C} = \overline{c_1}, \dots, \overline{c_w}$. The $\overline{c_i}$ is calculated as follows [172]:

$$\overline{c_i} = \frac{w}{n} \sum_{j=\frac{n}{w}(i-1)+1}^{\frac{n}{w}i} c_j \tag{5-4}$$

The average value of the data within an episode is calculated and a vector of these values over w intervals shows the dimensionality reduced representation. Before this transformation, which shows the Piecewise Aggregate Approximation (PAA) of the time series, we have standardized

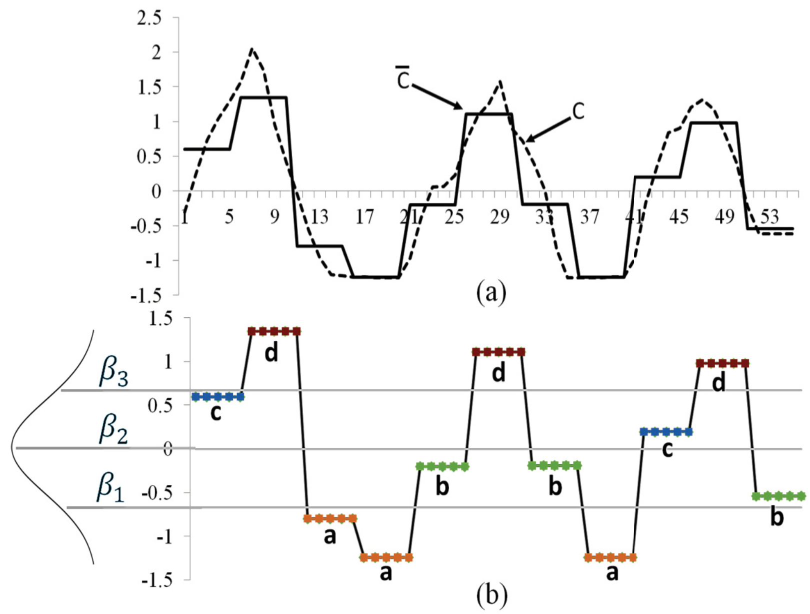

Figure 5-4: The main steps of SAX a) Piecewise Aggregate Approximation, b) Symbolic Discretization

the data to have a mean of zero and a standard deviation of one. If a time series is plotted in a Cartesian space, the PAA divides the *x* dimension into a set of intervals with an equal size [173]. Figure 5-4 (a) depicts the tidal volume of a subject after signal normalization and his PAA. A further transformation is applied to obtain a discrete representation known as Discretization. We need to have a technique that produces symbols with equiprobability [174][175]. This is easily achieved due to Gaussian distribution of the normalized time series [176]. We have applied SAX on per breath tidal volume achieved from the accelerometer data after signal normalization. The results show an accurate feedback alarm while there are major changes in tidal volume; however, in case of constant tidal volume this technique suffers from the problem of false alarms. Therefore, to avoid this and keep the data in an appropriate range, we have modified the data by injecting a square pulse at the end with zero and maximum value of the signal. The length of the pulse is considered either an episode size or the data size. The results are brought in section 5.4 while considering three scenarios: per breath tidal volume, per breath tidal volume with small pulse and large pulse.

Lin *et al.* [171] have found empirically using 50 different datasets that, the normalized time series have highly Gaussian distribution. There are two main methods of assessing normality: graphically and numerically. Figure 5-5 represents the normal probability plots of the cumulative distribution

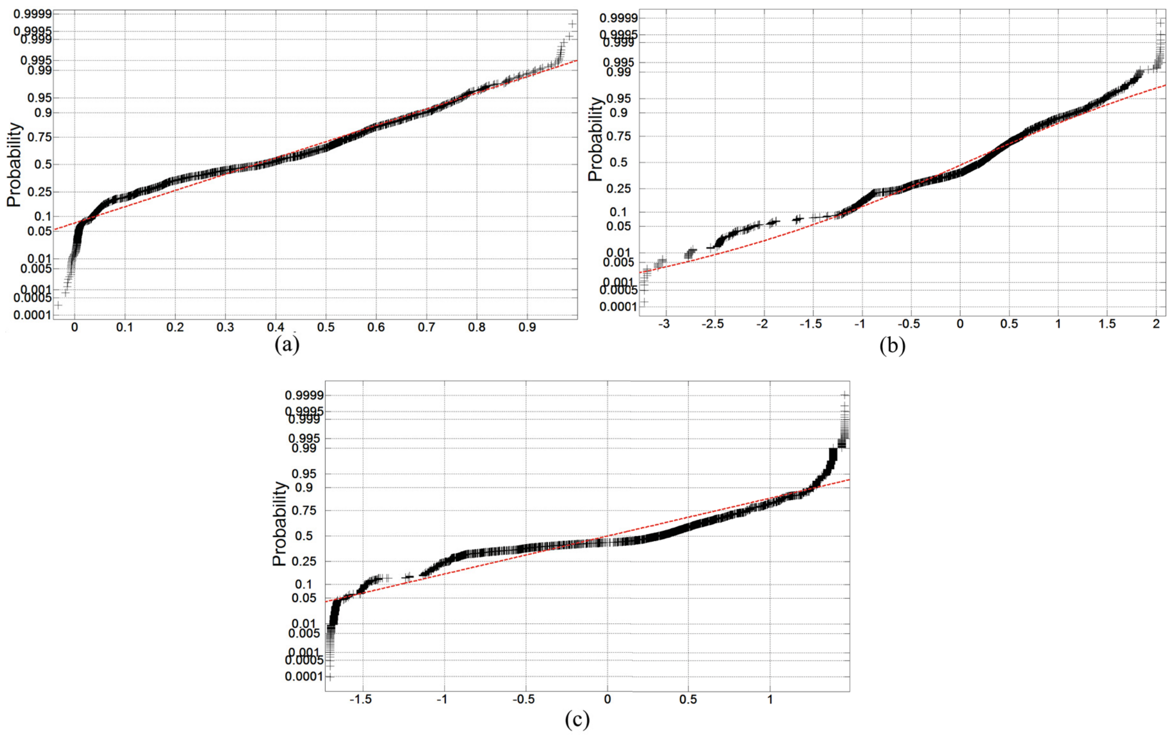

Figure 5-5: A normal probability plot of the cumulative distribution of data after normalization from all patterns and 8 subjects (a) Without pulse, (b) With small square pulse (c) With large square pulse

Table 5-1: A lookup table with the breakpoints that divide a Gaussian distribution in 3 to 6 of equiprobable regions [171]

β/α	3	4	5	6
β_1	-0.43	-0.67	-0.84	-0.97
β_2	0.43	0	-0.25	-0.43
β_3		0.67	0.25	0
β_4			0.84	0.43
β_5				0.97

from all considered respiration patterns. It shows the results from three scenarios with episode size 3 for 8 different volunteers. The linear nature of the plots suggests that the data derived from a highly Gaussian distribution [171]. In other words, the Kurtosis values for all scenarios are achieved between +1 to -1 [177], which numerically indicates that the data are following normal distribution. Now, the "breakpoints" can be determined to produce α equal-sized areas under Gaussian curve [176].

Definition: *"Breakpoints are a sorted list of numbers* $B = \beta_1, \dots, \beta_{\alpha-1}$ *such that the area under a* $N(0,1)$ *Gaussian curve from* β_i *to* $\beta_{i+1} = 1/\alpha$ *(*$\beta_0 = -\infty$*,* $\beta_\alpha = +\infty$*)"*[171].

These breakpoints are determined in a statistical table. Table 5-1 gives an example of the breakpoints for values of α from 3 to 6. Based on the equiprobable regions, Figure 5-4 (b) shows a sample of the alphabetic representation of per breath tidal volume with α equal to 4. The goal is to identify the critical points of tidal volume remotely and generate an alert in case of transaction to "a" or "d" sections. The SAX process is linear in time, which makes it suitable for stream processing in our real-time monitoring. The proposed method is briefly described in Algorithm 5-2. The new notations are defined as below:

A_i: Alarm state for i_{th} episode

S_i : Symbol (Alphabet) for i_{th} episode

L_i: i_{th} letter

In step 1 of Algorithm 5-2, we standardized the data to have a mean (μ) of zero and a standard deviation (σ) of one. Then in steps 2 to 6 the original time series with length n is transformed into PAA representation with size w. From step 7 to 16, the symbolic discretization is done considering the previous lookup table with the breakpoints that divide a Gaussian distribution into α equiprobable regions. Finally, the alarm detection is performed in lines 18 to 23. Since we set α to 4, the proposed system will generate an alert in case of transition to L_1 or L_4 sections due to our observations brought in subsection 5.4.3.

5.4 Experimental Results

For the evaluation of the proposed techniques, the results are derived from different subjects and breathing patterns explained in the next section.

5.4.1 Test Setup

The participants of this study were 4 males and 4 females aged 18 to 46. They were trained to perform each breath exercise before their recording sessions based on aforementioned definitions.

Algorithm 5-2

$\boldsymbol{alarmsDetection}\ (TV_{1:n}, \alpha, \beta_{1:\alpha-1}, A_{1:w})$ {
// ***Inputs***:$TV_{1:n}, \alpha, \beta_{1:\alpha-1}$ // ***Output***: $A_{1:w}$

$C_{1:n} = (TV_{1:n} - \mu_{TV_{1:n}})/\sigma_{TV_{1:n}}$; /*Data standardization*/
$\boldsymbol{for}\ (i = 1;\ i <= w;\ i++)$ {
  $sum = 0;$
  $\boldsymbol{for}\ (j = \frac{n}{w}(i-1)+1;\ j <= \frac{n}{w}i;\ j++)$
    $sum = sum + c_j;$
  $\overline{c_i} = \frac{w}{n} \times sum;$}
$\boldsymbol{for}\ (i = 1;\ i <= w;\ i++)$ {
  if $\overline{c_i} \leq \beta_1$
    $S_i = 'L_1';$
  elsif $\beta_1 \leq \overline{c_i} \leq \beta_2$
    $S_i = 'L_2';$
  elsif $\beta_2 \leq \overline{c_i} \leq \beta_3$
    $S_i = 'L_3';$
  …
  elsif $\beta_{\alpha-1} \leq \overline{c_i}$
    $S_i = 'L_\alpha';$} /* We obtained $S_{1:w}$ so far */
$S_0 = 'L_0';$ /* Only for the first iteration*/
$\boldsymbol{for}\ (i = 1;\ i <= w;\ i++)$ {
  $\boldsymbol{if}\ (S_i == 'L_1') \mid (S_i == 'L_\alpha')$ { /* $\alpha = 4$, and L_1, L_4 are “a” and “d” respectively*/
    $A_i = 1;$
    $\boldsymbol{if}\ (S_{i-1} \neq S_i)$
      Trigger_an_alarm;}}
$\boldsymbol{return}\ A_{1:w};$}

The experimental trials lasting for about 45 minutes (7 breathing signals) per subject resulting in a total of 112 different signals. In the test setup, we asked the subjects to perform normal (P1), Bradypnea (P2), Tachypnea (P3), and Kussmaul (P4) patterns, each for 1 minute, Cheyn-stokes (P5) and Biot’s (P6) each for 2 minutes and finally a pattern with different tidal volumes (P7) lasted for about 3 minutes. We assigned a 3-minute rest interval after performing each pattern. The LIS3DH 3-axis accelerometer was mounted on the subject’s chest in the middle of sternum region and secured by a soft and elastic strap which is easy to attach and comfortable to wear over the cloths. In the trial session, the subjects were in the lying position (torso at about 45° angle to the floor) on a chair; however, the rest positions or activities in which rib cage is stationary could be considered. The SPR-BTA spirometer signal is used as our reference that measures the oral breathing.

5.4.2 Accelerometer-derived Tidal Volume Variability Validation

We consider three types of pattern for tidal volume variability evaluation. In Biot's breathing, we expect to have reduction in tidal volume in each apnea with no significant changes during breathing cycles. However, in Cheyn-stokes pattern the tidal volume increases gradually and then decreases to start an apnea epoch. Additionally, we analyzed the changes in tidal volume for normal to deep, deep to shallow and shallow to normal conditions (P7). Figure 5-6 shows three respiration patterns for one of the subjects with his tidal volume variability obtained from accelerometer signal. There are positive changes from normal to deep as well as from shallow to normal breathing. As shown in Figure 5-6 (b), the variation from deep respiration to normal is less than changing pattern from deep to shallow breathing. We also obtain negative changes from deep to normal and deep to shallow breathing. The directions of the changes in TV_{var} are always the same as the spirometer in major changes. However, the different directions are resulted from the small acceleration movement of the body during constant tidal volume. To show the impact of size, we have swept t from 2 to 10 breaths. Indeed, t shows the sensitivity of the method. As can be seen in Table 5-2, there is a tradeoff between t and correlation. Larger window size resulted in better correlation of accelerometer versus the spirometer. This is due to unwanted motions of the rib cage during constant tidal volume epochs. Applying larger window size removes the trends of constant tidal volume while keeping the major changes. It is worth noting that, based on our patterns introduced earlier; we increase the size of window up to 10 breaths, because there are always more than 10 breaths per cycle in all of our patterns (P5, P6 and P7). Based on the respiration disorder, if the tidal volume of the patient changes frequently, the small window size is preferable; otherwise, larger size show the trend of tidal volume accurately over time. Therefore, in our portable platform we could manage the appropriate sensitivity value for the graphical representation of TV_{var} based on different breath disorders characteristics. The overall correlation is obtained 0.87 whereas it proves that TV_{var} derived from the accelerometer is strongly correlated with spirometer.

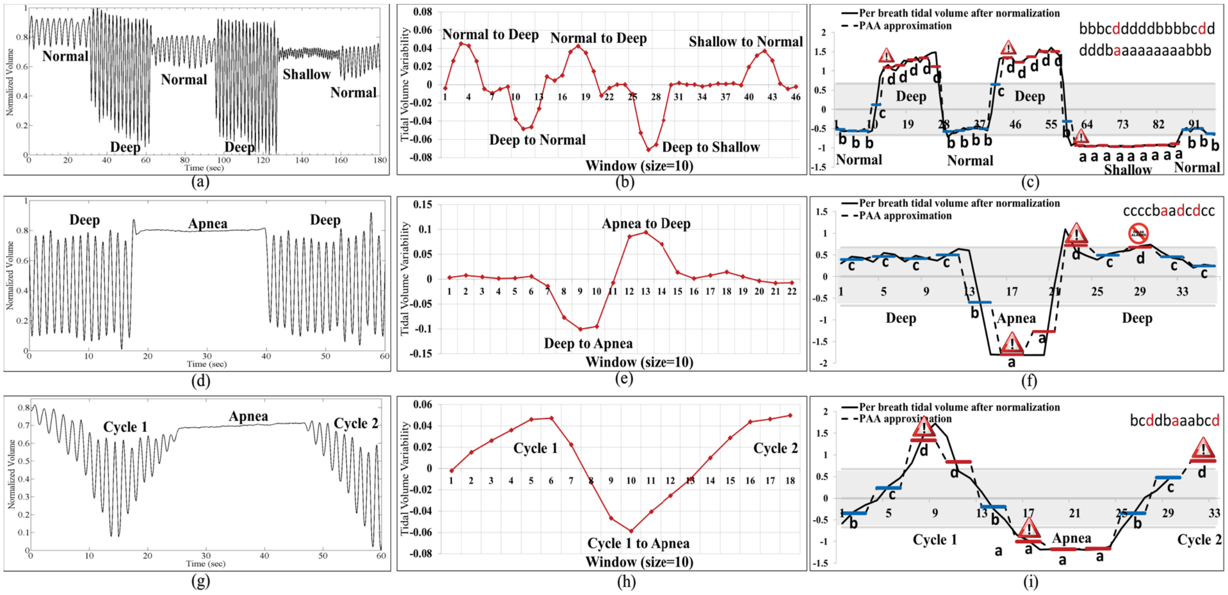

Figure 5-6: (a), (d), (g) P7, P6 and P5 breathing patterns derived from an accelerometer signal, (b), (e), (h) Tidal volume variability for P7, P6 and P5, (c), (f), (i) Symbolic representation of normalized tidal volume for alert detection system in P7, P6 and P5.

Table 5-2: Correlation values between tidal volume variability from accelerometer and spirometer of three different patterns

Subject ID	Correlation values												
	P5				P6				P7				
	t=2	t=3	t=5	t=10	t=2	t=3	t=5	t=10	t=2	t=3	t=5	t=10	Average
S1	0.90	0.94	0.96	0.98	0.74	0.81	0.86	0.84	0.86	0.89	0.91	0.95	**0.89**
S2	0.77	0.81	0.84	0.93	0.56	0.69	0.77	0.88	0.71	0.79	0.82	0.87	**0.79**
S3	0.63	0.80	0.88	0.93	0.70	0.80	0.85	0.94	0.68	0.77	0.81	0.89	**0.81**
S4	0.96	0.96	0.96	0.98	0.72	0.89	0.90	0.95	0.81	0.91	0.94	0.96	**0.91**
S5	0.88	0.92	0.95	0.98	0.59	0.71	0.91	0.97	0.80	0.86	0.92	0.93	**0.87**
S6	0.68	0.91	0.96	0.96	0.73	0.81	0.91	0.96	0.80	0.83	0.84	0.86	**0.85**
S7	0.74	0.77	0.82	0.91	0.77	0.87	0.92	0.96	0.77	0.81	0.85	0.87	**0.84**
S8	0.98	0.99	0.99	1.00	0.94	0.96	0.97	0.99	0.96	0.96	0.96	0.97	**0.97**
Average	**0.82**	**0.89**	**0.92**	**0.96**	**0.72**	**0.82**	**0.89**	**0.94**	**0.80**	**0.85**	**0.88**	**0.91**	**0.87**

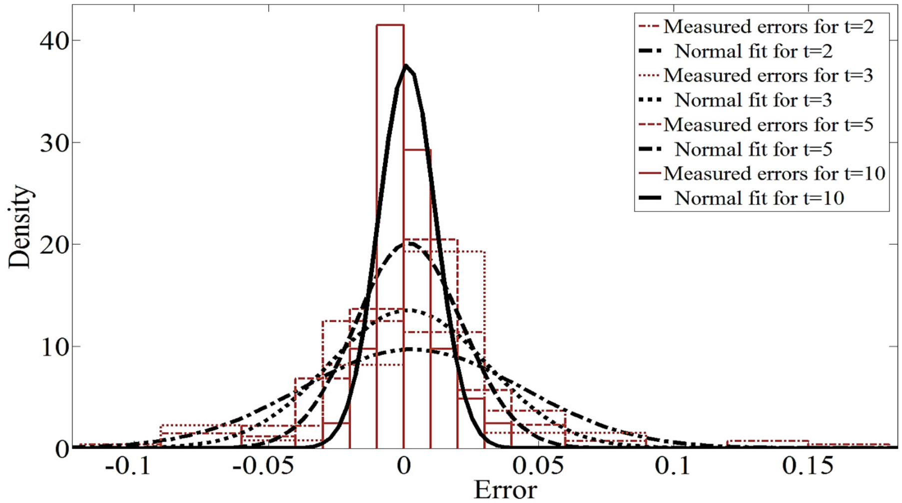

Figure 5-7: Normal fittings of the MSEs between accelerometer and spirometer for P6 of subject S2 considering different window sizes

The average Mean Square Errors (MSE) of the estimated tidal volume variability versus the reference for three types of patterns are 3.06E-05, 1.86E-03, 1.07E-03 and 4.33E-04 with standard deviations 7.27E-03, 4.36E-03, 2.31E-03 and 8.41E-04 for t = 2, 3, 5 and 10, respectively. The errors do decrease at the larger window sizes due to less sensitivity in the constant tidal volume variability periods.

Observation 1: The computed MSE for each subject can be fitted into a normal distribution, depicted in Figure 5-7. In this figure, the fitted normal distributions correspond to the average log-likelihood value of 124.8 ± 28.60 on different t, which indicates a good fit.

Figure 5-7 also shows the impact of the window size on MSE distributions. When the window is small the standard deviation is larger compared to the case with larger window sizes. For example with t = 10, the MSEs have less dispersion from the average value of zero. Therefore, a very high correlation between accelerometer-derived TV_{var} and spirometer indicates that the proposed method is promising to be used in a respiration tracking system specially for real-time monitoring of breath diseases during rest positions. Furthermore, the low MSE values suggests excellent consistency between actual and expected estimated tidal volume variability values.

5.4.3 Proposed Alert System Evaluation

So far, we have assessed a graphical representation of tidal volume variability in our remote monitoring platform. This section evaluates the method we developed for discovering the critical turning points in per breath tidal volume. As mentioned earlier, finding an accurate threshold value to identify the emergency alarms during critical and major changes is required, either in circadian remote monitoring or in e-health centers. We propose a new method to detect these changing points using symbolic representation of time series [171].

The evaluation are performed on three scenarios: per breath tidal volume, per breath tidal volume with small pulse and large pulse for 8 people and all seven patterns. From pattern P1 to P4 there is no major changes in tidal volume and we expect to have constant volume with no alarm; however for patterns P5, P6 and P7 the system should alert 5, 2 and 3 times in the considered window, due to the sudden increments and decrements of tidal volume. In other words, we define the critical points as transition into a high or very low breath volume as well as the apnea events.

Indeed SAX method removes the small redundant acceleration movement of the body during constant tidal volume. Note that in our experiments, we focus on extracting the major changes and we experimentally set the alphabet size to 4. However, to have a more sensitive alert system the users are able to increase the number of alphabets. In Figure 5-8, we compare the symbolic representation of all patterns for three scenarios and episode size 3. For example, in Figure 5-8 (m), there are two false alarms generated by the system when there is no pulse in the data; however, injecting large pulse reduces the number of false alarms into one and with small pulse, we can achieve zero false alarm. In Cheyn-stokes pattern, the system is supposed to alert in sudden increment and decrement of the volume. For instant, in Figure 5-8 (k) the system alerts 5 times with no false or undetected alarms. In other example, considering Figure 5-8 (l), the system generates true alarms in both ninth episode due to the sudden reduction of tidal volume and in twelfth episode after coming back into high constant tidal volume in Biot's pattern. It is worth mentioning that, in our proposed system the alert is generated when the tidal volume enters into "a" or "d" sections based on the following observation. Furthermore, Figure 5-6 (c) shows the alerts when tidal volume goes from normal to deep and deep to shallow breathing (3 alerts).

Observation 2: The best results are achieved by considering "a" and "d" as critical sections among all 15 combinations of four symbols. However, in case of any changes in the number of symbols, the condition might be changed for the emergency alert generation.

The average accuracy values of alarm system with different episode sizes are shown in Figure 5-9. We have changed the episode size from 3 to 10 sec. Figure 5-9 (a) depicts the accuracy of the alarm system for patterns with constant tidal volume on three scenarios. We note that the accuracy is almost constant for different episode size in patterns with constant volumes whereas for patterns with major changes (Figure 5-9 (b)), the larger the episode size, the smaller the accuracy of alarm system. Moreover, the figures demonstrate the improvement of the proposed alarm system after injecting both small and large square pulses. The overall accuracy for all patterns is plotted in Figure 5-9 (c) in which the blue sign corresponds to the best accuracy of 98.28% based on the small square pulse with episode size equal to 3. In Figure 5-10, we brought the accuracy of three patterns P5, P6 and P7, individually. It can be seen that the augmentation of episode size more affects the accuracy rates of Cheyn-stokes patterns in which there exist gradual changes, rather than the Biot's and P7 patterns in both large and small pulse injections. The results of Positive Predictive Alarm (PPA), Negative Predictive Alarm (NPA), False Positive Alarm Rate (FPAR) and False Negative Alarm Rate (FNAR) are listed in Table 5-3. PPA and NPA denote the rates of true predicted existing and non-existing alarms. False positive and false negative alarms refer to false alarms and undetected alarms, respectively. The formulas are summarized as follows:

$$PPA = \frac{T_P}{T_P + F_P} \tag{5-5}$$

$$NPA = \frac{T_N}{T_N + F_N} \tag{5-6}$$

$$FPAR = \frac{F_P}{T_N + F_P} \tag{5-7}$$

$$FNAR = \frac{F_N}{T_P + F_N} \tag{5-8}$$

$$Accuracy = \frac{T_P + T_N}{T_P + F_N + F_P + T_N} \tag{5-9}$$

Table 5-3 highlights the parameters for three patterns with major changes. It is shown that the accuracy values of our alarm detection system suffers when the episode size is incremented resulted from high information loss values.

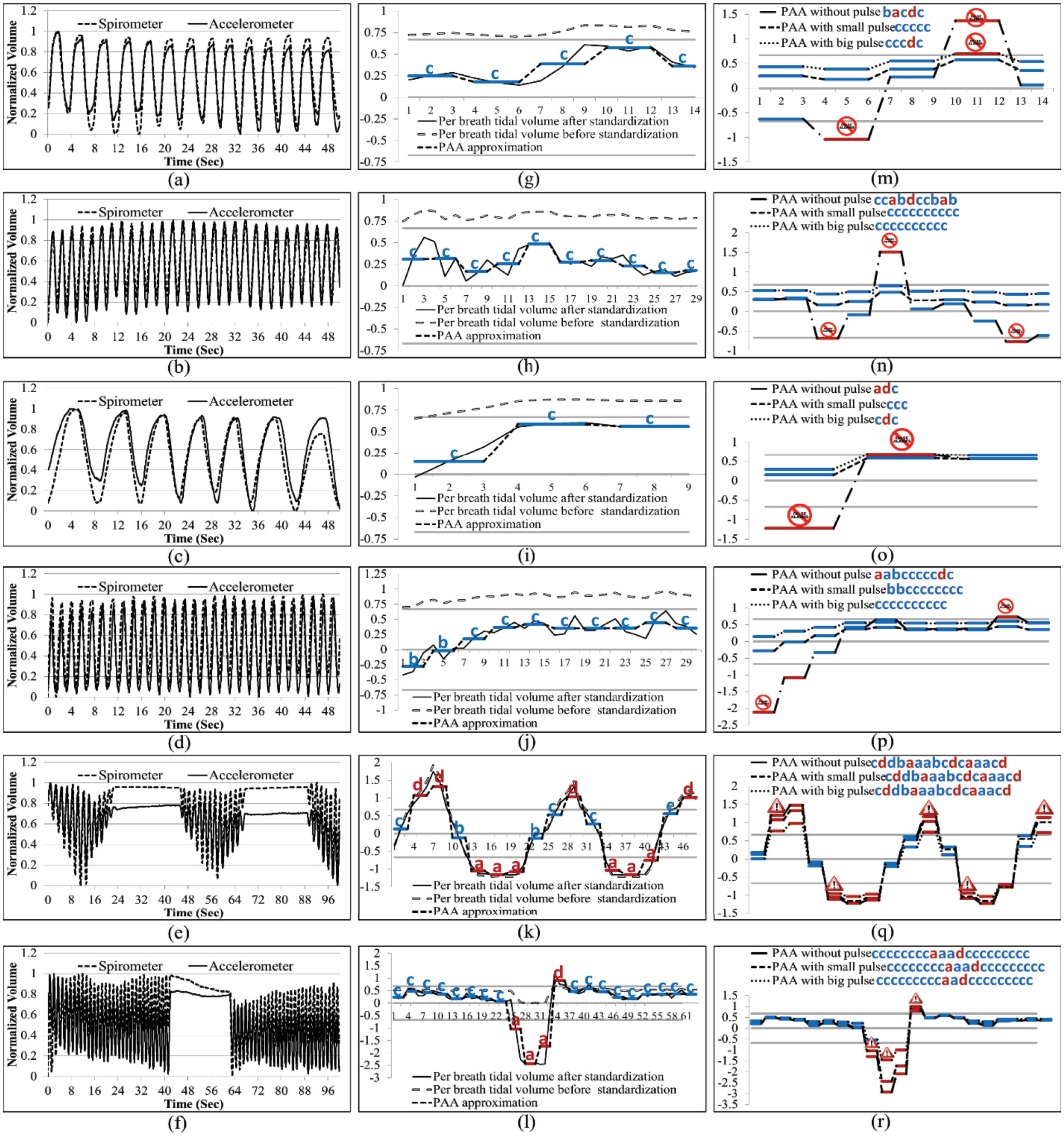

Figure 5-8: (a) Normal, (b)Tachypnea, (c) Bradypnea, (d) Kussmaul, (e) Cheyn-stokes, (f) Biot's breathing patterns from both accelerometer and spirometer, (g), (h), (i), (j), (k), and (l) The SAX of normal, Tachypnea, Bradypnea, Kussmaul, Cheyn-stokes and Biot's breathing, correspondingly with injecting small square pulse, (m), (n), (o), (p), (q) and (r) The SAX of all three considered scenarios for normal, Tachypnea, Bradypnea, Kussmaul, Cheyn-stokes and Biot's, respectively

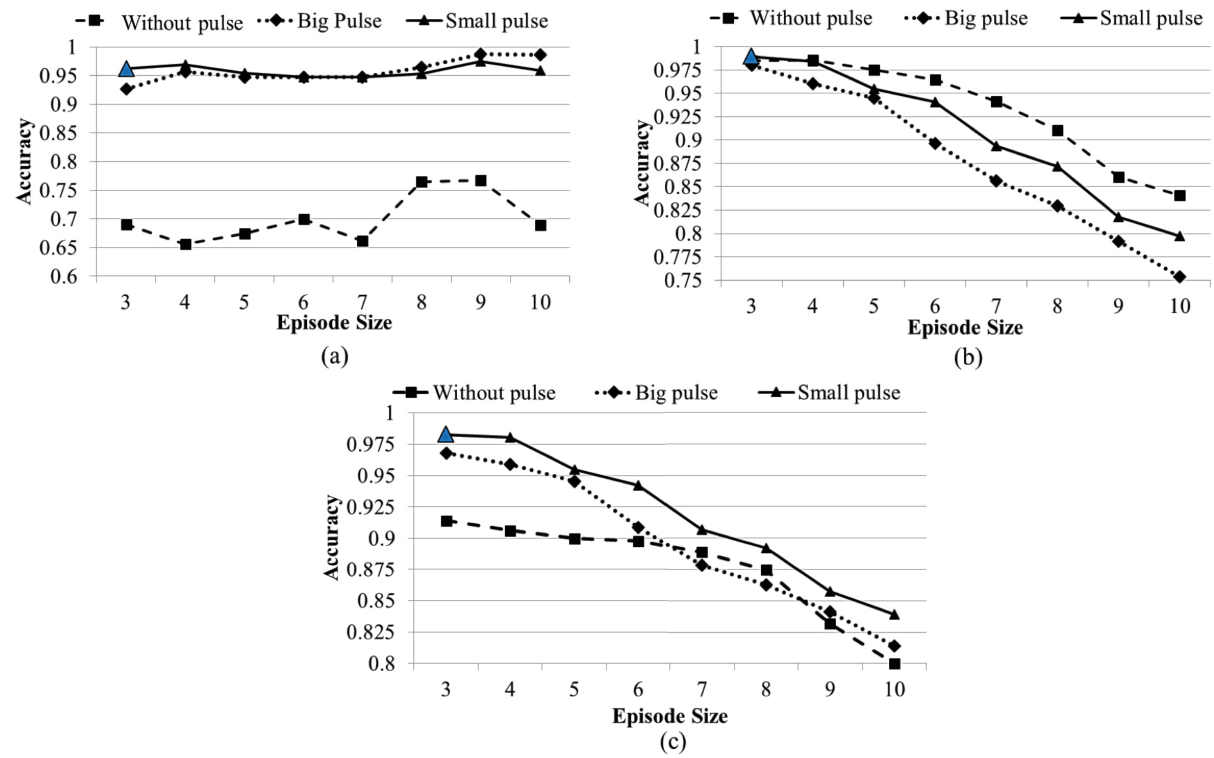

Figure 5-9: (a) Average accuracy of alarm system for P1, P2, P3, P4 with three scenarios on all subjects, (b) Average accuracy of alarm system for P5, P6, P7 with three scenarios on all subjects, (c) Average accuracy of alarm system for all patterns with three scenarios on all subjects

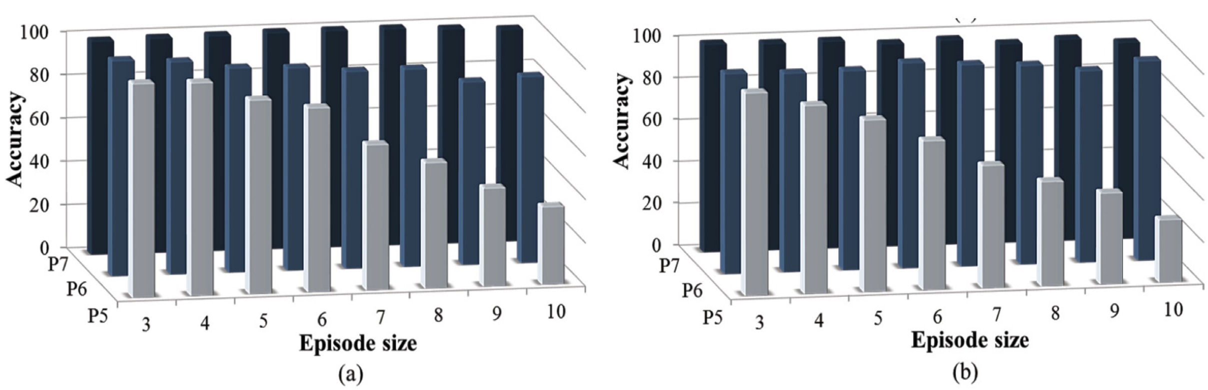

Figure 5-10: (a) Average accuracy of alarm system for P5, P6 and P7 with small square pulse injection on all subjects, (b) Average accuracy of alarm system for P5, P6 and P7 with big square pulse injection on all subjects

Table 5-3: Average quality parameters of alert detection with both small and big square pulse injections for different episode sizes on all subjects

Episode Size	Parameters of tidal volume alert detection when injecting small square pulse (%)														
	P5					P6					P7				
	PPA	NPA	FPAR	FNAR	Accuracy	PPA	NPA	FPAR	FNAR	Accuracy	PPA	NPA	FPAR	FNAR	Accuracy
3	**97.78**	**99.09**	**0.91**	**2.22**	**98.71**	**94.44**	**100**	**0.53**	**0**	**99.51**	**100**	**98.55**	**0**	**12.90**	**98.67**
4	100	97.26	0	4.26	98.31	83.33	100	2.12	0	98.08	100	99	0	6.89	99.12
5	77.78	100	16.67	0	89.47	66.67	99.06	5.41	7.69	94.35	100	99.35	0	3.57	99.45
6	73.33	100	25.53	0	85	61.11	99.06	6.25	8.33	93.55	100	100	0	0	100
7	48.89	100	47.92	0	67.14	55.56	100	10	0	91.11	100	100	0	0	100
8	42.22	100	60.47	0	58.06	61.11	100	10.14	0	91.25	100	100	0	0	100
9	33.33	100	75.00	0	45.45	38.89	100	17.19	0	84.51	96.29	100	1.27	0	99.04
10	28.89	100	86.48	0	36.00	50.00	100	16.07	0	86.15	96.30	100	1.51	0	98.91

Episode Size	Parameters of tidal volume alert detection when injecting big square pulse (%)														
	P5					P6					P7				
	PPA	NPA	FPAR	FNAR	Accuracy	PPA	NPA	FPAR	FNAR	Accuracy	PPA	NPA	FPAR	FNAR	Accuracy
3	91.11	99.09	3.54	2.38	96.77	83.33	98.40	1.60	16.66	97.07	92.59	100	0	0.71	99.34
4	73.33	100	14.12	0	89.83	83.33	98.55	2.16	11.76	96.79	92.59	99.50	0.98	3.84	98.69
5	62.22	100	25.37	0	82.11	83.33	100	2.75	0	97.58	92.59	100	1.27	0	98.91
6	48.89	100	39.66	0	71.25	61.11	100	7.44	0	93.33	88.89	98.45	2.30	7.69	96.79
7	35.55	100	53.70	0	58.57	50	100	9.38	0	91.42	92.59	99.06	1.85	3.84	97.76
8	31.11	100	64.58	0	50.00	61.11	100	10.14	0	91.25	85.19	97.85	4.21	8.00	95.00
9	31.11	100	75.61	0	43.64	27.78	100	19.69	0	81.69	92.59	97.47	2.53	7.41	96.22
10	22.22	100	87.50	0	30.00	44.44	100	17.54	0	84.61	85.19	97.10	5.63	8.00	93.75

Table 5-4: Average quality parameters of our alert detection with considered scenarios for different episode sizes on all subjects

Episode Size	Parameters of tidal volume alert detection for all patterns and subjects														
	Without pulse					With small pulse					With big pulse				
	PPA	NPA	FPAR	FNAR	Accuracy	PPA	NPA	FPAR	FNAR	Accuracy	PPA	NPA	FPAR	FNAR	Accuracy
3	97.78	90.87	0.28	45.34	91.41	**97.77**	**98.34**	**0.21**	**12.87**	**98.28**	90.00	97.56	1.17	19	96.77
4	97.78	89.49	0.39	40.54	90.62	93.33	98.77	1.05	7.69	98.03	81.11	98.25	2.93	12.05	95.92
5	95.56	88.91	1.00	36.29	90.03	82.22	98.19	3.56	9.76	95.49	75.55	98.42	4.81	9.33	94.55
6	88.89	90.03	2.98	31.03	89.80	78.89	98.06	5.09	8.97	94.23	63.33	97.79	8.55	12.31	90.90
7	82.22	91.11	6.11	24.49	88.88	65.55	98.32	9.60	7.81	90.69	54.44	97.97	12.34	10.90	87.86
8	75.56	91.70	8.66	23.59	87.46	63.33	98.42	11.70	6.56	89.21	53.33	98.02	14.48	9.43	86.30
9	64.84	90.08	12.8	28.92	83.18	53.33	99.09	16.22	4.00	85.76	48.88	98.63	17.55	6.39	84.14
10	63.74	87.89	16.50	28.40	80.07	53.33	98.42	18.34	5.88	83.92	45.55	98.42	20.76	6.82	81.42

Furthermore, the rates of false and undetected alarms are low dramatically in small episode size while we could obtain high true positive and negative alarm rates. Therefore, in case of facing a problem, the alert system will function properly as a sound alarm, email or SMS alert to the users. As an example, based on Table 5-3, with episode size 3 and 4 (with injecting small square pulse), we could obtain more than 98% accuracy in all three patterns with various types of tidal volume oscillations. In addition, the worst-cases of positive and negative predictive alarms with episode size 3, are 94.44% and 98.55%, correspondingly. Besides, our intelligent alarm system is designed to take care of the people and meanwhile, it should not be so sensitive that leads to excessive false alarms. Hence, from Table 5-3, it is observed that the low rates of both false negative and positive alarms (FPAR and FNAR) clearly demonstrate the robustness of the proposed technique. SAX technique depends on the size of data; here we apply SAX on all recorded data of our individuals. However, after different executions we conclude the following observation.

Observation 3: Smaller size of data will result in more sensitivity for the proposed alarm system, so that the rate of positive predicted alarm increases whereas the negative predicted alarm do decrease at the same time. Therefore, according to the criticality of the breath disorder, the data size should be chosen based on the require sensitivity prescribed by the doctor.

The overall rates and accuracies based on all patterns (P1 to P7) and conditions are outlined in Table 5-4. Our experimental results show that applying SAX method on tidal volume after small square pulse injection can attain at least 83.92% accuracy with episode size 10 whereas the best accuracy of 98.28% is achieved with episode size 3 (bold line in Table 5-4). In the proposed technique, the false negative and positive alarm rates are also very low which show considerably low false and undetected alerts.

5.5 Summary

In this chapter, a method was introduced to obtain tidal volume variability from an accelerometer data as a reliable and unobtrusive technique over extended periods. A new data-driven alert system was also designed and evaluated for tidal volume emergency situation feedback which can filter the false alarms and provide a high detection accuracy. This method applied a technique to

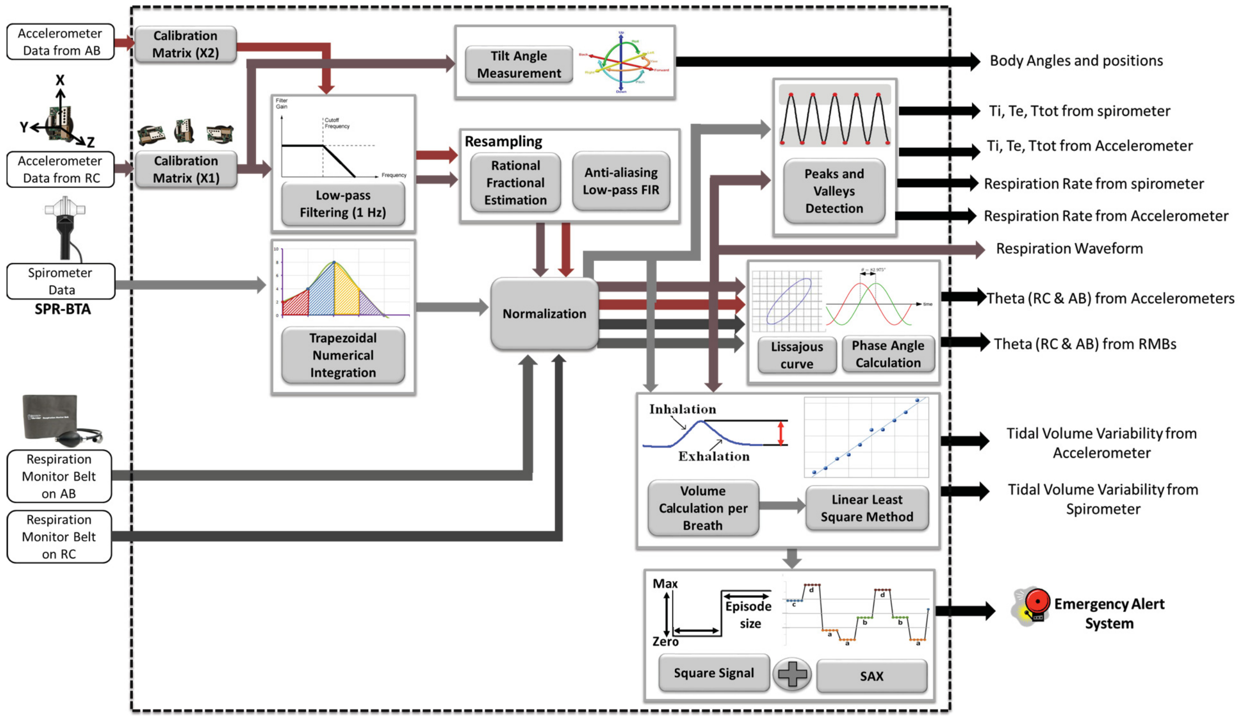

Figure 5-11: The overall view of the proposed procedures

dynamically calculate the alarm thresholds to effectively reduce the false alarm occurrences. Therefore, the platform can perform essential functions to fashion the signals received from the cloud, process them and eventually setoff the emergency alarm. The overall procedures are summarized in Figure 5-11.

Chapter 6

RESPIRATION DISORDERS CLASSIFICATION

Respiratory disorder is a highly prevalent condition associated with many adverse health problems. As the current means of diagnosis are obtrusive and ill-suited for real-time e-health applications, we explore a reliable and accurate automatic approach based on on-body inertial sensing system. In this chapter, we integrate inertial sensors with machine learning techniques to model a wide range of human respiratory patterns. A set of sensors is deployed on the user's body to register their upper body movements when performing a particular breathing pattern. An extensive evaluation is provided on different well-known classifiers with novel lightweight features as well as hierarchical tree-structured classification models. In addition, the effects of the number of sensors, sensor placement, feature selection and different sampling rates on accuracy as well as accuracy versus sensitivity are discussed. The different assessments of classification parameters are provided by measuring the specificity, F1-score and Matthew Correlation Coefficient (MCC).

6.1 Motivation

An accurate identification of breathing disorders requires direct measurement of upper airway airflow and respiratory effort. Although the Polysomnography (PSG) is known as the de facto gold standard mean in respiration disorders diagnosis, it is complicated, expensive, time consuming and has to be conducted in laboratory. Furthermore, it is scarce for everyone since there are few hospitals, which provide PSG test especially in rural areas. Due to this fact, a vast majority of patients with breathing disorder problems remain undiagnosed which may increase the risk of developing cardiovascular diseases such as stroke and heart failure. Another traditional technique for diagnosis of breath problems resulted from lung diseases is stethoscope. It is a widely used tool for the identification of various lungs' disorders. However, the interpretation of lung sounds strongly depends on the experience of the physician [178].

The advent of mobile health technology and maturity of pervasive sensing, wireless technology as well as data processing techniques enables us to provide an effective solution for remote detection of breathing problems and promote individual's health. Mobile health or m-health market was estimated to be valued at USD 1,950 million in 2012, with an estimated Compound Annual Growth Rate (CAGR) of 47.6% from 2014 to 2020 [179]. The previous available techniques and devices, albeit their accuracy, are expensive and could not be integrated in m-health applications. This unmet need for unobtrusive monitoring of respiration signal for the goal of respiration illnesses diagnosis has triggered research in introducing the use of wearable MEMS sensors. Therefore, such a system can help reducing the use of emergency department and hospital services resulted in increased health care team productivity. There are several methods for classification of normal and pathological breathing patterns, which are described in Chapter 2. For instance, [112] used a multi-layer perceptron neural network classifier applied on spirometry data. The total accuracy, sensitivity and specificity of 97.6%, 97.5% and 98.8% are achieved, respectively. Mahesh *et al.* [113] discussed the problem of binary classification with 92% accuracy through pulmonary function test and neural network. A neural network is described in [114] with flow-meter spirometer to differentiate between normal and obstructive abnormality. The validity of their result was tested with the accuracy 90%. In [115], the authors provide a combined two sequential binary neural network classifiers to detect normal, obstructive and restrictive breathing models. The first classifier separates the normal and abnormal patterns followed by the second binary classification between obstructive and restrictive breathing models. They could obtain an average accuracy of 92.5%. In this chapter, robust models are extracted and evaluated based on acceleration signals to distinguish among 2 to 9 different pathological breathing patterns, accurately.

6.2 The Proposed Methods

Breathing disorders recognition means identifying the patterns of one or more individuals using a series of observations and environmental conditions as formulated as follows:

Definition: With p extracted features from the motion sensors, given a set $W = \{w_1, w_2, \dots, w_m\}$ of labeled and equal-sized time windows, and a set $A = \{a_1, a_2, \dots, a_n\}$ of respiration patterns' labels, the goal is to find the best classifier model C, such that for any w_k which contains a feature set $F_k = \{f_{k,1}, f_{k,2}, \dots, f_{k,p}\}$, the predicted label $\hat{a}_k = C(F_k)$ is as identical as possible with the actual breathing model performed during w_k.

The recognition procedure starts with collecting data from the motion sensors. In order to capture the dynamics of the signals, the data are partitioned into segments of either fixed or variable size. Afterward, a feature extraction procedure is carried out to enhance the characteristics unique to each breath model and provide a more tractable representation of the signals for the respiration pattern classification. These features are inputted to a classifier, which ultimately yields the recognized breathing model to one of the considered patterns.

There are two main types of data features: time and frequency domain features. The time domain features are cheaper than the frequency domain features, because for the frequency domain features the sampling rate should be high enough to capture all of the relevant frequencies in each window. Although, a higher sampling rate may increase the accuracy, it will cause higher battery consumption. Therefore, in this thesis, we make use of time domain features, which are lightweight and can help to reduce latency and power consumption as the key factors during our online classification. These features might have different ranges resulted in a failure in classifier and recognition system. Therefore, to overcome this issue, rescaling the range of features and standardization are used. If f is an original value, the standardized value f' is determined based on the mean and standard deviation values of each feature (linearly scale to mean 0 and variance 1) [180].

$$f' = \frac{f - \mu}{\sigma} \tag{6-1}$$

In this thesis, we focus on supervised learning methods that create a predictor model based on known input objects (typically a vector) and known responses to the input data. Then, this model generates predictions for the response to a new window of data. The best extracted classification model can run through cloud computing to provide remote online detection of abnormal breathing patterns. The Windows Azure is an example of public cloud solution among different other providers such as Amazon Web Service, Google App Engine, Cloud Foundry, Engine Yard, Heroku, Mendix and OpenShift. Windows Azure is provided in the model of pay-per-use by Microsoft [181] which has main advantages such as the support of different programming languages, excessive documentation (MSDN Library) and availability of new learning courses. These advantages encourage us to choose Windows Azure as our cloud-computing environment.

6.2.1 Hierarchical Support Vector Machine (HSVM)

The main preprocessing steps for breath patterns classification are calibration, filtering and resampling explained in Chapter 3. The data segmentation is a requirement for feature/knowledge extraction. The window size is an important factor in data analysis and classification performance and should be large enough to contain a span of target event and avoid overlapping two unrelated data. Another main aspect is the percentage of adjacent windows overlap. There are different segmentation techniques including Fixed-size Non-overlapping Sliding Window (FNSW), Fixed-size Overlapping Sliding Window (FOSW), Top-Down (ToD), Bottom-UP (BUp), Sliding Window and Bottom-up (SWAB), and Variable-size Sliding Window (VSW) [182]. In this section, we make use of FOSW with window size and overlap values equal to 10sec and 0.8, respectively. Once the data are segmented, they must be labeled based on the different classes and then a hierarchical tree structure is built for modeling the classification problem. At each level of the tree, a SVM classifier is used based on the extracted features and data are separated into one of the branches. Once we reach a leaf node, a final classification is made.

6.2.1.1 Feature Extraction

Features can be thought of as statistically unique elements of the sensor data, which are used to differentiate diverse classes or states. In the proposed system, classes are the different respiration patterns inferred from various types of breath disorders such as normal, Bradypnea, Tachypnea, Kaussmal and two types of constraint breathing, such as Cheyn-stokes and Biot's respiration patterns. Features such as Energy (E), Mean, Maximum (Max), Standard Deviation (SD), Inter-axes Correlation ($Corr$) and the number of local maxima (P) are calculated on three axes (X, Y, Z) of the accelerometer and the magnitude of them $\left(Mag = \sqrt{X^2 + Y^2 + Z^2}\right)$. The features are listed in Table 6-1. Here S corresponds to the acceleration signal, and n is the number of samples. Besides, we extract the Approximate Entropy (ApEn) from the accelerometer signals as one of the main features in our classifier explained in the next subsection. Indeed, there are a vast number of diverse features providing freedom in selection best suit for each application.

6.2.1.1.1 Approximate Entropy (ApEn)

ApEn is a technique introduced by Pincus [183] to quantify the regularity/irregularity of a signal. It has been applied to describe changes in physical activity measures as well as other movement tasks [184]. ApEn has two user-specified parameters: m, a positive integer, indicates the length of compared window, and r is the tolerance range. It is worth mentioning that, although m and r are critical in determining the outcome of ApEn, there is no established consensus for choosing these parameters in short datasets, especially for biological data [184]. In our experiments we set m and r to 5 and 0.15, respectively.

For a n sample time series $\{u(i): 1 \leq i \leq n\}$, given m, form vector sequences x_1^m through $x_{n\text{-}m+1}^m$ as follows:

$$x_i^m = \{\, u(i), u(i+1), \dots, u(i+m\text{-}1)\}, \quad i = 1, \dots, n\text{-}m+1 \tag{6-2}$$

For each $i \leq n\text{-}m+1$, let $C_i^m(r)$ be $(n\text{-}m+1)^{-1}$ times the number of vectors x_j^m within r of x_i^m which means [185]:

$$C_i^m(r) = (n\text{-}m+1)^{-1}(number\ of\ j\ such\ that\ d[x(i), x(j)] \leq r) \tag{6-3}$$

$$d[x(i), x(j)] = \max_{k=1,2,\dots,m}(|u(i+k+1)\text{-}u(j+k\text{-}1)|) \tag{6-4}$$

ApEn is obtained from Eq. (6-5) as follow [183]:

$$ApEn(m, r) = \lim_{n\to\infty}[\, \phi^m(r) - \phi^{m+1}(r)] \tag{6-5}$$

$$\phi^m(r) = (n-m+1)^{-1} \sum_{i=1}^{n-m+1} ln\, C_i^m(r) \tag{6-6}$$

The ApEn calculation returns a nonnegative number where higher value shows irregularity of the signal and more regularity resulted from the lower ApEn. Note that ApEn can be used even for small data samples in real time, which makes it suitable for our cloud-based monitoring platform.

Table 6-1: The features for HSVM classification

Features	Description
Mean	$\bar{s} = \frac{1}{n}\sum_{i=1}^{n} s_i$, where s_i corresponds to the samples, $i = 1, \dots, n$
Standard Deviation	$SD = \sqrt{\frac{1}{n}\sum_{i=1}^{n}(s_i - \bar{s})^2}$, where s_i corresponds to the samples, $i = 1, \dots, n$
Inter-axis Correlation	$r_{\overrightarrow{s_1},\overrightarrow{s_2}} = \frac{n(\sum_{i=1}^{n} s_{1_i} s_{2_i}) - (\sum_{i=1}^{n} s_{1_i})(\sum_{i=1}^{n} s_{2_i})}{\sqrt{[n\sum_{i=1}^{n} {s_{1_i}}^2 - (\sum_{i=1}^{n} s_{1_i})^2][n\sum_{i=1}^{n} {s_{2_i}}^2 - (\sum_{i=1}^{n} s_{2_i})^2]}}$ where s_{1i} and s_{2i} are samples from two axes, $i = 1, \dots, n$
Energy	$e = \sum_{i=1}^{n} s_i^2$, where s_i corresponding to the samples, $i = 1, \dots, n$
Approximate Entropy	$ApEn(m, r, n) = \frac{1}{(n-m+1)}\sum_{i=1}^{n-m+1} \ln C_i^m(r) - \frac{1}{(n-m)}\sum_{i=1}^{n-m} \ln C_i^{m+1}(r)$ n is the number of samples in time series s_i, r is the tolerance range and m is the length of compared window and C is the correlation integral [185]
Maximum	*Max* (s, w) = The maximum value of s in window size *w*.

6.2.1.2 Feature Selection

The problem of reducing the dimension of the features (an optimal subset of q features out of the extracted set of P features) in order to improve performance and most likely accuracy is called feature selection. In [186] the feature selection algorithms are categorized into three ways i.e. complete, heuristic and random. Complete or exhaustive category includes algorithms which examine all combinations of feature subset and the order of search space is $O(2^P)$, where P is the number of features. However, as discussed in [187] a complete search can be non-exhaustive without jeopardizing the chances of finding the optimal subset such as Branch & Bound algorithm.

In the heuristic techniques, the selection is directed under certain guideline and optimal subset may not be achieved. However, the search space is smaller and faster than complete methods. In random category, there is no predefined way to select feature candidate, and features are picked at random e.g. based on a probabilistic approach. In each random generation procedure, some input parameters should be carefully assigned for achieving good results [187]. In this section, a heuristic feature selection technique is used which performs an exhaustive search on all pair of extracted features resulted in a complexity of $O(P^2)$.

The proposed tree-structured model is shown in Figure 6-1. G_{ij} represents the j_{th} group and f_{ik} is the k_{th} feature of the i_{th} branch. The best selected pair of features are brought in "Experimental Result" section. First, the data are automatically separated into G_{11} and G_{12} groups, employing the assigned labels in "Labelling" section shown in Figure 6-2 and then are passed in to the second and third levels. For classifying between different groups in each branch all pairwise of extracted features are analyzed in terms of accuracy and then the best pair is chosen for the specific branch. This procedure is repeated for each branch, separately. Finally, the breathing data are categorized into six classes based on the selected features.

6.2.1.3 HSVM Classification

The key advantage of SVM classifier is the ability of minimizing both structural and empirical risks [188]. These properties make SVM to be a strong generalization for new data classification even in case of limited training dataset. Therefore, in this chapter, the classification procedure on breathing disorders starts by evaluating linear and non-linear SVM classifiers. SVM is based on constructing one or a set of hyperplanes in a high dimensional space. It constructs linear functions from a set of labeled training dataset. The linear separator is constructed considering maximum distance from the hyperplane to a fraction of the data points, named support vectors [189] shown in Figure 6-2. SVM is designed for binary-classification problems with n training samples. Each sample is indicated by (x_i, y_i) where $(i = 1, 2, \dots, n)$. For a given dataset $\{x_i, y_i\}$, $i = 1, \dots n$, $y_i \in \{-1, +1\}$, $x_i \in R^d$, y_i is either 1 or −1, indicating the class to which x_i, belongs, and x_i is a d-dimensional real vector. The notation R^d refers to the Cartesian product of d copies of R, which is a d-dimensional vector space over the field of the real numbers. The SVM classifier is formulated as Eq. (6-7).

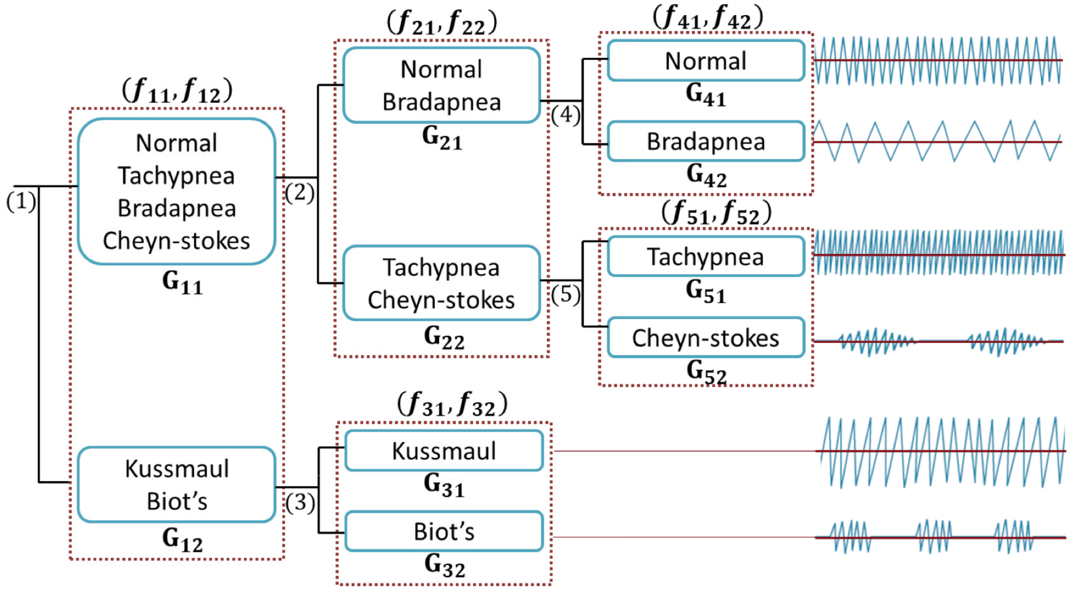

Figure 6-1: Tree-like structure of proposed hierarchical SVM classifier

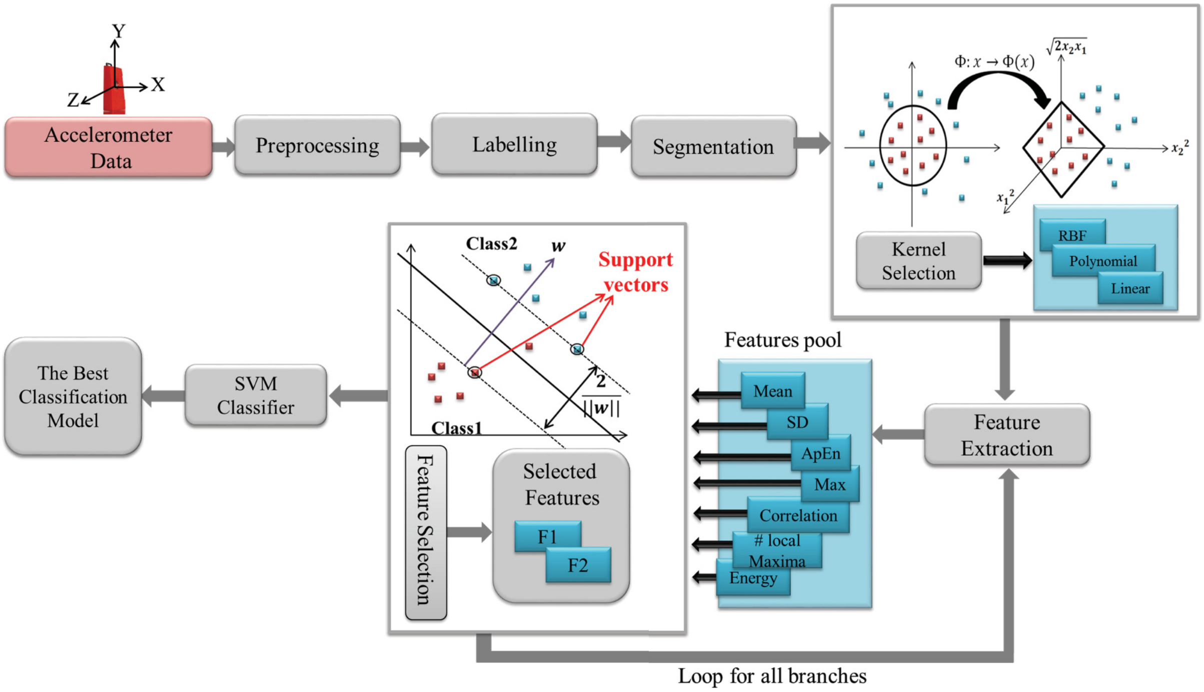

Figure 6-2: Respiration disorders classification procedure using different kernel functions in HSVM classifier.

$$f(x) = sign\left(\sum_{i,j=1}^{n_{sv}} \alpha_i\, y_i K(x_i, x_j) + b\right) \tag{6-7}$$

The optimization problem is a convex quadratic optimization with quadratic function subject to linear constraints, which is transformed into the Lagrangian dual with the Karush-Kuhn-Tucker (KKT) conditions. Lagrange multiplier α_i is linked with every inequality of the linear constrains in the primal problem. A kernel function $K(x_i, x_j) = \phi(x_i)^T \phi(x_j)$ gives the inner product value of x_i and x_j in the feature space and n_{sv} presents the number of the support vectors. Three types of kernels are evaluated in this chapter:

- Linear kernel: $\boldsymbol{K(x_i, x_j) = x_i^T x_j}$
- Polynomial kernel with degree 3: $\boldsymbol{K(x_i, x_j) = (x_i^T x_j + 1)^3}$
- Radial basis function (RBF) kernel: $\boldsymbol{K(x_i, x_j) = exp(-\frac{\|x_i - x_j\|}{2\sigma^2})}$

The performance of SVM depends on the choice of the kernel function to transform data from input space to a higher dimensional feature space. There are no defined rules for choosing the kernel type, except satisfactory performance by simulation study [189]. Figure 6-2 depicts the whole system flow of breathing disorders recognition architecture.

6.2.2 Robust classification based on Informative Features

In this section, new sets of time domain features are introduced to enhance the robustness of the classifier model. These informative features are obtained based on the respiration parameters explored from acceleration signal and individually evaluated in Chapters 4 and 5 on different groups of subjects. In addition, the number of breathing patterns (classes) are augmented from 6 to 9 in order to provide a more comprehensive model. An extensive evaluation is provided on six well-known classifiers as described in the following sections.

After preprocessing of the raw readouts, the stream of sensory data requires segmentation in order to facilitate effective feature extraction. We apply two window-based segmentation methods FNSW and FOSW to investigate the effectiveness of these techniques with respect to the window length and the percentage of adjacent windows overlap in obtaining the highest event classification accuracy. These techniques provide low complex implementations and reasonable performance, which will be discussed in details later.

6.2.2.1 Feature Extraction

The choice of features with high information content for classification purpose is a fundamental phase and a highly problem-dependent task. Therefore, we make use of features, which are evaluated, individually on different groups of subjects. The features are extracted from each separate window of data and then used as the inputs to the classifiers. The proposed features are simple, easy to calculate and will interpret the respiration parameters, properly. These features include Mean, Standard Deviation (SD), Respiration Rate ($RR = \frac{P \times 60}{ws}$; P is the number of local maxima and ws represents the window size in second), average respiratory time parameters: inspiration time (T_i) and expiration time (T_e), average tilt angles (roll and pitch), mean tidal volume variability (TV_{var}; with $t = 3$), average accelerometer-based breath volume (TV; with $t = 3$), mean phase shift (θ) and Symbolic Aggregate approXimation (SAX; with $w = 3$ and $\alpha = 4$) of the data. We choose mean and standard deviation, since they are widely used in different classification problems [190]-[192] and carry discrimination potential and ease of interpretation in the acceleration domain. Besides, the standard deviation, provide insights into the intensity and magnitude of the respiration function. The rest of features are validated with medical references in Chapters 4 and 5. Likewise, six of the most extensively and successfully used machine learning techniques are considered for classification.

6.2.2.2 Feature Selection

Generally, feature selection is used to reduce redundancy among features, as well as to minimize dimensionality. The fundamental hypothesis in feature selection is that good feature sets include features which are highly correlated with the class, but uncorrelated with each other [193]. Indeed, by recognizing the most relevant features extracted from all accelerometer axes for our classification training, those aspects of the data, which are most useful for analysis and future prediction, are considered. The feature selection techniques that select features regardless of the model are called filter methods. The wrapper method, in contrast, evaluates subsets of features based on the target learning algorithm. In this section, we use the Correlation-based Feature Selection (CFS), which is categorized as a filter technique. The results indicate that, in general, CFS can outperform the wrapper on small datasets [193], therefore, it is an appropriate feature selection for our classification. Furthermore, CFS as a filter, does not suffer from the high computational cost associated with repeatedly invoking the learning algorithm. The CFS algorithm attempts to maximize the following objective in its heuristic search strategy [193].

$$M_s = \frac{k\bar{r}_{cf}}{\sqrt{k + k(1-k)\bar{r}_{ff}}} \tag{6-8}$$

Where M_s is the heuristic merit of feature subset S with k features, $\bar{r}_{cf}$ is the average feature-class correlation and $\bar{r}_{ff}$ is the mean feature-feature inter-correlation. Here, CFS starts from an empty set of features and uses a forward best first search. The search is considered completed once five consecutive fully expanded subsets resulted in no improvement over the current best subset.

6.2.2.3 Classification Algorithms

In this section, we are dealing with the supervised methods, which use the class label when discretizing features. Thus, after data segmentation and feature selection, the training set is labelled, determining the corresponding classes. Here, we aim to provide a comprehensive evaluation over different classification algorithms including Decision Tree (DT), Decision Tree Bagging (DTB), Linear Discriminant Analysis (LDA), k-Nearest Neighbors (kNN), Support Vector Machines (SVM) and Multilayer Artificial Neural Networks (ANN).

DT classifies the instances by sorting them down the tree from the root to some leaf nodes, which indicate the classification results of an instance. Indeed, the internal nodes contain attribute test conditions to separate the instances that have different characteristics. Among different methodologies to combine classification models, ensembles of decision trees are described as the most accepted approaches [194]. DTB builds an ensemble of classification trees (in our tests 50) and uses bagging to combine the predictions. This family of classifiers are simple and very easy to interpret. The principle idea of LDA is to find a linear transformation that best discriminates among multiple classes. The classification is then performed in the transformed space based on metric such as Euclidean distance [195]. k-Nearest Neighbors algorithms have been used since 1970 in various applications such as statistical prediction and pattern recognition. It is a straightforward classifier, where instances are classified based on the "k" closest training examples in the feature space. This classifier stores all cases and classify new cases based on the similarity measurement [196]. k is set to 10 in our experiments. SVM is based on finding optimal separating decision hyperplanes between classes with the maximum margin between patterns of each class. The main advantage of this classifier as mentioned before is the ability of minimizing both structural and empirical risks. These properties make SVM to be a strong generalization for new data classification even in case of limited training dataset. In this section, we make use of SVM with Error Correcting Output Codes (ECOC) with One-Versus-One (OVO) coding design in our multi-class classification. The idea of using ECOC [197] is to break the multiclass task into several binary classification tasks and then combining the results of these classifiers to obtain the final outcome. Since SVM is very popular in binary classification, we choose to use ECOC for combining $l(l-1)/2$ multiple binary SVMs with linear kernel function [198] where l refers to the number of classes and is nine in the proposed classification.

Artificial neural networks provide a robust tool which helps people analyze, model and make sense of big clinical data across a wide range of medical applications [199]. It has proven itself to be widely used for diagnosis of diseases such as acute nephritis and heart problems. NN is inspired from simulation of biological nervous system and is represented as a set of neurons and connections between them [199]. The basic neural network architecture has three layers including input, hidden and output layers. The data is propagated through successive layers, and the final result is available at the output layer. Multilayer perceptron neural network (MLP) uses more than one hidden layer in its structure which might help in solving complex problems where a single hidden layer cannot provide an acceptable result [200]. We have used 20 hidden layers in our experimental results. In the next section, we compare the results of all described classifiers based on the proposed feature extraction and selection for distinguishing among nine different breathing

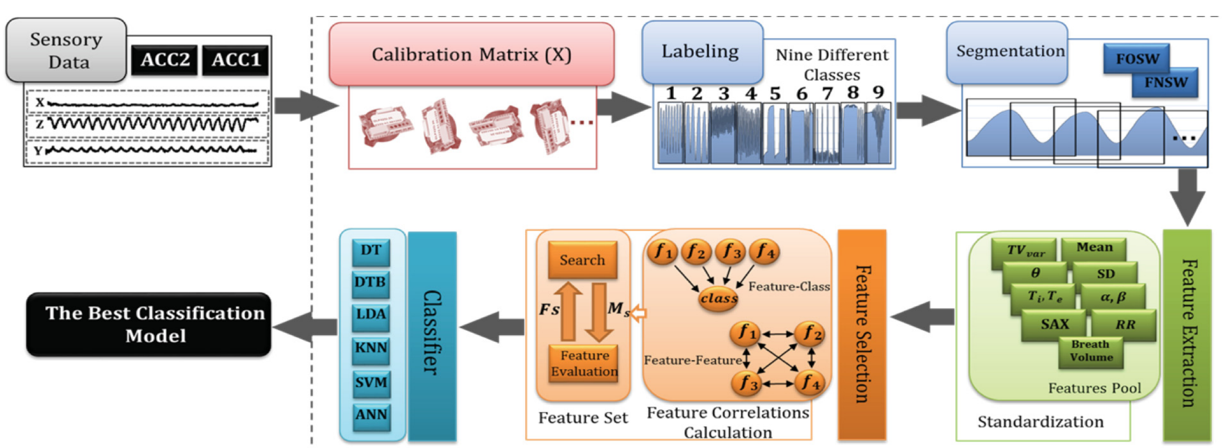

Figure 6-3: Respiration disorders classification procedures

patterns. Furthermore, our classification problem is also modeled as a binary classification for detecting normal and abnormal breathing patterns. The experimental results of the proposed binary model is also provided in section 6.3.3.4. Figure 6-3 depicts the whole system flow of breathing disorders recognition. In the next section, an innovative classification model is introduced by considering the proposed informative features and binary classifiers to optimize the accuracy rates and worst-case sensitivity of our multi-class problem, simultaneously.

6.2.3 Evolutionary Hierarchical Model for Breathing Disorders Classification

In this section, an evolutionary hierarchical classification model is proposed, which not only maximizes the accuracy of the classification, but also tries to optimize the classification rate for each class. In general, the second objective is not usually discussed in recognition systems, but is considered here to obtain high precision in each class in real problems. To solve this machine-learning problem, we use a Pareto-based multi-objective optimization methodology based on Genetic Evolutionary Algorithm. One of the potential benefits of Pareto-based learning approach is that using multiobjective techniques may help the learning algorithm to less likely get trapped at local optima, which results in improving the accuracy of the model [201].

6.2.3.1 Hierarchical Binary Tree Structure

The proposed top-down hierarchical structure is constructed based on a binary tree where each inter nodes represents a binary classifier and leaf nodes are the breathing patterns (classes). The tree is built from top to bottom by starting with a binary classifier with two groups of m and n classes, $G_n, G_m$where $G_n \cup G_m = G_l$, $G_n, G_m \neq \emptyset$, and $G_n \cap G_m = \emptyset$ and $l = 9$ in our problem. So, G_l and G_1 denotes the root and leaf, correspondingly, and the number of classifiers are $l - 1$. In particular, binary tree-based hierarchical multi-class classifications have been widely accepted due to their high accuracy and low computational complexity. The total number of trees is obtained from Eq. (6-9), where M denotes a set of classifiers with $|M|$ number of methods. Of course, such a complete search is impossible due to millions of feasible binary trees (>3,000,000 in our case). Consequently, there is a great interest in evolutionary algorithm that attempts to discover near-optimal solutions within a reasonable time while effectively sampling large search spaces.

$$T = \sum_{\substack{i=1 \\ N_1=1}}^{l-1} \binom{l}{i} \times N_i \times |M| \text{ , } where\ N_i = \sum_{j=1}^{i-1} \binom{i}{j} \times N_j \qquad (6\text{-}9)$$

Here, we choose multiobjective Genetic Algorithm (GA) as an optimization technique. It is a variant of NSGA-II [202] that uses a controlled elitist genetic algorithm. A controlled elitist GA takes into account both individuals with better fitness value and those can help increase the diversity of the population even if they have a lower fitness value. As the first step, a chromosome is defined with two layers as $C = (C_{class}, C_{model})$. The first layer, $C_{class} = (C_{class}[1], C_{class}[2], \dots, C_{class}[l])$, is the sub-chromosome representing the terminal node to which the point j, $j = 1,2 \dots, l$, is attached. It is an integer number within the interval $[1, l-1]$. The second layer $C_{model} = (C_{model}[1], C_{model}[2], \dots, C_{model}[l-1])$ represents the type of classifier in each node where $\forall\, i \in \{1,2,\dots,l-1\}$, $C_{model}[i] \in M$; so that it is an integer within interval $[1, |M|]$. There are two conditions to determine whether the chromosome is a feasible candidate as follows:

$$\forall\, i \in \{1,2,\dots,l-1\}, \qquad size(C_{class} == i) \leq 2\,, \qquad (6\text{-}10)$$

$$\forall\, j \in \{1,2,\dots,l-2\}, \qquad p_j > 0 \qquad (6\text{-}11)$$

Where:

$$p_j = \ p_{j-1} - size(C_{class} == j) + 1, \qquad p_0 = 1, (j = 1,2,\dots,l-2) \qquad (6\text{-}12)$$

The first condition in Eq. (6-10) insures that the graph is a binary tree and each node has at most two children. The second condition in Eq. (6-11) checks if there exists a place $(p_j > 0)$ to add either a class or classifier in the next step. $size(C_{class} == j)$ returns the total number of places where C_{class} is equal to j. Algorithm 6-1 presents the binary tree generation procedure and the conditions. The algorithm starts with the first node n_1 in the root of the tree shown in the first line. $freePositions$ is an array to store the available places in the tree in each iteration. In other words, $size\big(freePositions(j)\big) = p_j$ in the j_{th} iteration. Therefore, in line 3, the second condition in Eq. (6-11) is validated. For example, if $indices == 1$ ($case$ 1 in line 13), then it is corresponding to the left child as a leaf (line 14) and consequently node n_2 will be the root of right sub tree shown in line 16 of the Algorithm 6-1. If $indices == 0$, node n_2 and node n_3 are added as the roots of left and right sub trees in lines 9-12. And in case of $indices == 2$ the corresponding class labels

Algorithm 6-1

```
buildTree(C, tree) {
// Inputs: C    Output: tree /*if the chromosome is a valid binary tree*/

1. validationFlag = true; freePositions(1) = tree.root; j = 0; /*Initialization*/
2. for (i = 1; i < l; i++){
3.     if (freePositions(i) != Null){ /*Checking the second condition in Eq. (6-11)*/
4.         tree.insert (n_i, freePositions(i));
5.         n_i.model = C_model[i]; /*Determining the classifiers model for node n_i*/
6.         indices = find(C_class == i);
7.         swich size(indices):
8.         case 0:
9.             j++;
10.            freePositions(j) = (n_i.left);
11.            j++;
12.            freePositions(j) = (n_i.right);
13.        case 1:
14.            n_i.left = indices[1];
15.            j++;
16.            freePositions(j) = (n_i.right);
17.        case 2:
18.            n_i.left = indices[1];
19.            n_i.right = indices[2];
20.        others: /*The first condition in Eq. (6-10) */
21.            validationFlag = false;
22.            break;
23.    else
24.        validationFlag = false;
25.        break;}}
26. if (validationFlag == true)
27.   return tree;
28. else  return -1;} /*The chromosome is invalid */
```

are added as the left and right leaves in lines 18 and 19. Otherwise, $size(C_{class} == i) \geq 2$ and $validationFlag$ indicates that this chromosome is not a valid tree to be considered as out classification model. In addition, in line 5, the type of n_i classifier is determined based on the $C_{model}[i]$ values.

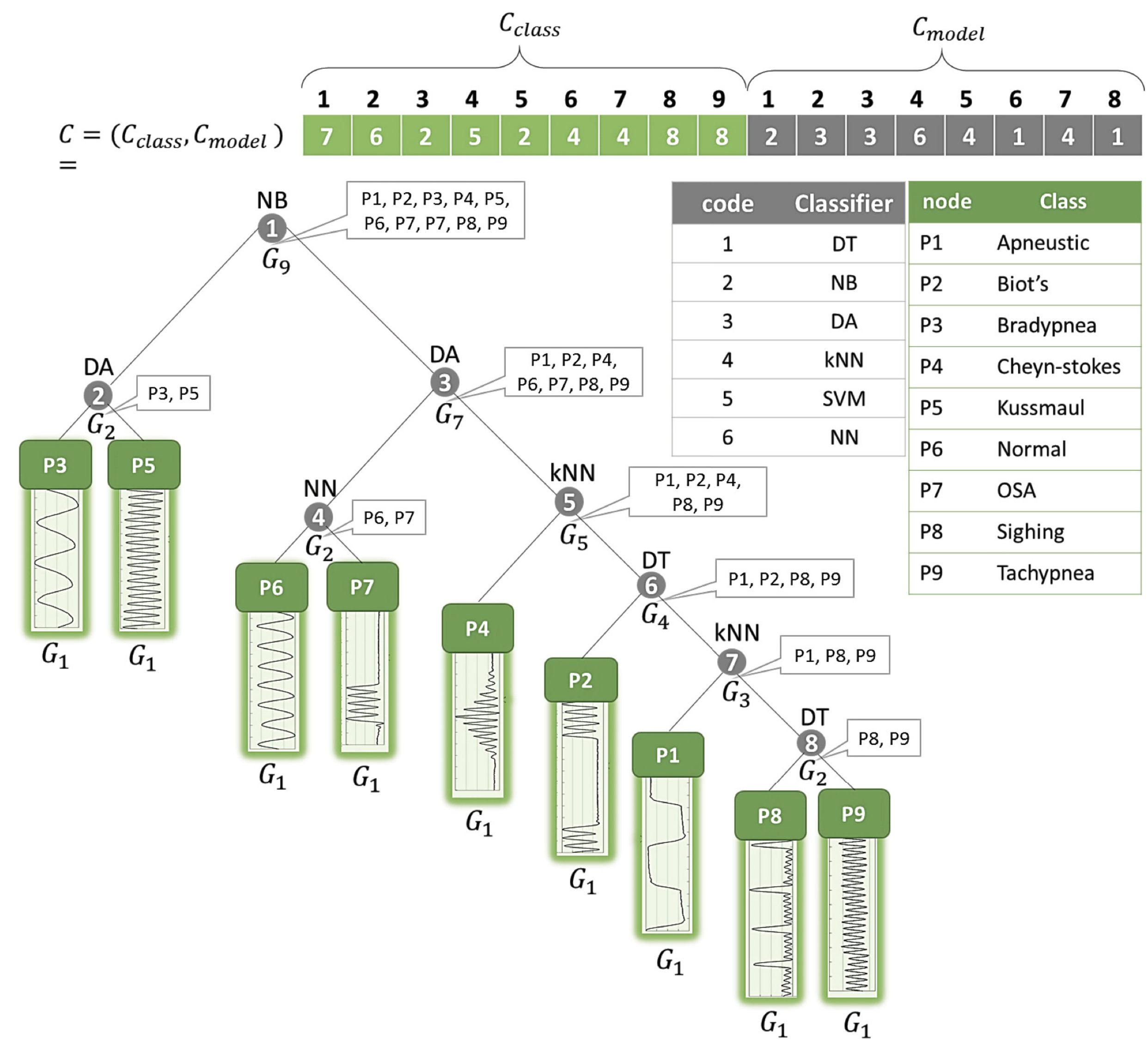

Figure 6-4: Example of the chromosome and corresponding hierarchical tree-structured classification

This procedure is repeated downward for each node based on the explained conditions. Figure 6-4 depicts an example of the proposed hierarchical binary tree structure with a sample chromosome. In this section, the Fixed-size Overlapping Sliding Window (FOSW) is used where the window and overlap values are set according to the best results of the section 6.2.2. The features are also based on the informative features derived from the accelerometer sensors in section 6.2.2.1. The CFS feature extraction algorithm is applied where six binary classifiers, DT, NN, kNN, DA, Naïve Bayes (NB) and SVM are used in each node of the tree. So, $M = \{DT, NB, DA, kNN, SVM, NN\}$ and $|M|$ is equal to 6 in our experiments.

6.2.3.2 Fitness function

In this section, we define a new model to maximize the accuracy of the classification as well as obtain an acceptable level of accuracy for each class. The accuracy rate is used as the performance measure, which is defined as the proportion of correct classifications with respect to the total classified instances as Eq. (6-14) [152]. Each row in confusion matrix CM indicates the instances in a true class, while each column represents the instances in a predicted class. We also consider the minimum of the sensitivities of all classes, i.e. the lowest percentage of trials correctly predicted for each class with respect to the total number of trials in the corresponding class. These two objectives, after certain levels, are usually in conflict in the optimization process. Here, the sensitivity for multi-class classification is defined in Eq. (6-15):

$$CM = \begin{bmatrix} M_{11} & \cdots & M_{1l} \\ \vdots & \ddots & \vdots \\ M_{l1} & \cdots & M_{ll} \end{bmatrix} \tag{6-13}$$

$$Accuracy = A = \frac{\sum_{i=1}^{l} CM(i,i)}{\sum_{i=1}^{l}\sum_{j=1}^{l} CM(i,j)} \times 100 \tag{6-14}$$

$$Seneitivity_i = \frac{CM(i,i)}{\sum_{j=1}^{l} CM(i,j)} \times 100 \tag{6-15}$$

$Sensitivity_i$ is the number of patterns correctly predicted to be in class i with respect to the total number of patterns in class i (sensitivity for class i). From the above equation, we define the sensitivity of the classifier as the minimum value of the sensitivities for each class as follows:

$$S = \min_{i=1,\dots,l} Seneitivity_i \tag{6-16}$$

Therefore, the main objective is summarized in Eq. (6-17):

$$Objective = Maximize(S, A) \tag{6-17}$$

The 2-D measure (S, A) associated with a given classifier is considered in this study. It is important to note that S and A are not cooperative in general. At the beginning of a learning process, accuracy and sensitivity could be cooperative, but after a certain level, these objectives become competitive while an increase in one objective tends to cause a decrease in the other one. This property have

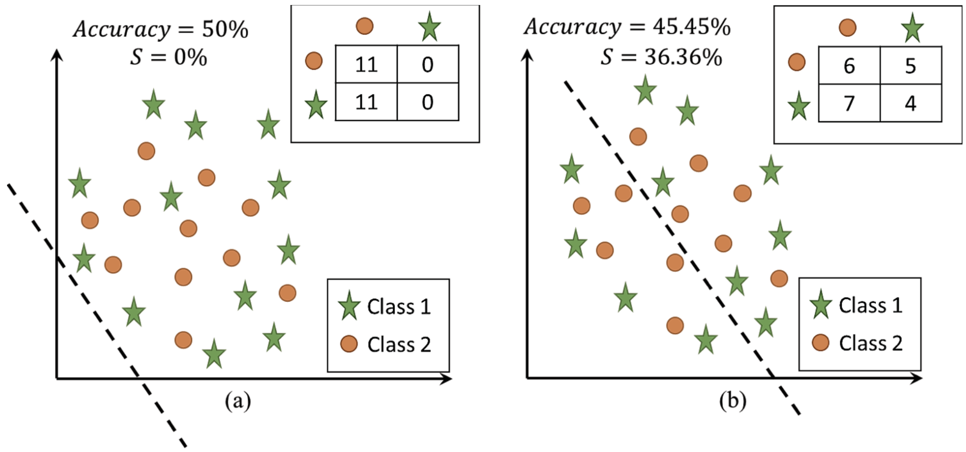

Figure 6-5: Accuracy and minimum sensitivity as conflicting objectives

been also proved in [201] considering 17 classification benchmark problems. Since we have equal number of trials for training and testing in different classes, we consider the percentage rates for both accuracy and sensitivity. The example in Figure 6-5 shows that S and A are conflicting objectives in general. For that balanced two-class example, in the left graph, the linear classifier obtains $A = \frac{11}{22}$, and $S = 0$. If we want to improve the sensitivity, the decision boundary should be moved to separate the green star class from the circle one resulted in reduction of the accuracy. We aim to find the hierarchical tree-structured model, which simultaneously optimizes two objectives: the global performance in the whole dataset and the performance in each class.

6.2.3.3 Genetic operators

The basic genetic operators in GA are selection, crossover, and mutation. We used the *gamultiobj()* function in MATLAB with Tournament selection, Adaptive Feasible mutation and Two points crossover with their default settings. The population size is set to 30 with 50 generations.

To verify the effectiveness of our proposed classification methodologies, we have considered two groups of dataset illustrated in the next subsection.

6.3 Experimental Results

This section aims to quantitatively analyze the capabilities of the proposed classification models on different groups of subjects.

6.3.1 Test Setup

The described three classification techniques are evaluated on two different groups. The first group includes 9 healthy volunteers, 3 men and 6 women aged 24 to 48 with (Mean ± SD), 31 ± 7.26. The experimental trials lasted for about 45 minutes per subject. We asked the subjects to perform normal, Bradypnea, Tachypnea, and Cheyn-stokes patterns, each for 2 minutes (6000 samples) and the other two types for 1 minute with a 3-minute rest interval. For simulating apnea in Cheyn-stokes and Biot's breathing exercises, we requested the participants to pause breathing for at least 10 seconds. In the trial sessions, the subjects were in the lying position. The second group consists of 10 healthy volunteers, 5 males and 5 females aged 27 to 48 with (Mean ± SD) 34.80 ± 6.89. The tests lasted for about 35 minutes per subject. The subjects are asked to perform nine introduced breathing patterns, each for 1 minute in sitting position (torso at about 90° angle to the floor). For simulating apnea in Cheyn-stokes, Biot's and OSA breathing exercises, the subjects paused their breathing for at least 10 sec. They are also asked to prolong their inspiration and expiration during Apneustic maneuver for at least 5 sec. Finally, for Sighing pattern, they perform normal breathing, which is followed by deep periodic of inspiration every 3-7 sec. Figure 6-6 shows 30-second samples of eight normalized respiration patterns derived from an accelerometer sensor. OSA breathing pattern is similar to Biot's breathing pattern; however, considering two accelerometer

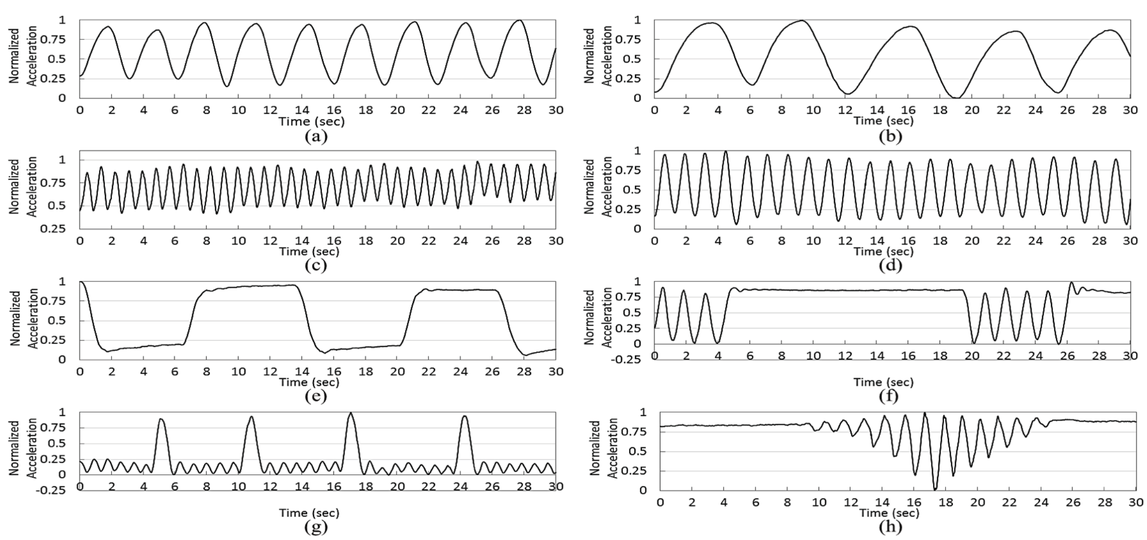

Figure 6-6: (a) Normal, (b) Bradypnea, (c) Tachypnea, (d) Kussmaul, (e) Apneustic, (f) Biot's, (g) Sighing and (h) Cheyn-stokes breathing patterns from accelerometer sensor mounted on the subject's chest

sensors, it has different phase shift between chest and abdomen compared to Biot's breathing. The SPR-BTA spirometer is also used in all tests to make sure that the subjects were not over emphasizing the breathing movements.

In the first classification algorithm presented in section 6.2.1, we provide experimental results on 12-bit resolution data derived from one SensorTag with 3-axis KXTJ9 accelerometer sensor. The sensor was mounted on the subject's chest in the middle of sternum and secured by a soft and elastic strap which is easy to attach and comfortable to wear. Two LIS3DH 3-axis accelerometers with 12-bit resolution are also worn by the second group to obtain the performance results on classification techniques proposed in section 6.2.2. The first sensor (Acc1) is mounted on the subject's chest in the middle of sternum region and the second accelerometer (Acc2) sensor is attached on the subjects' umbilical region. In our tests, the sensors are sampling with 50Hz rate.

6.3.2 Performance Evaluation of HSVM Classification

We have evaluated the performance of the proposed classification while it is individualized to each subject (case 1) as well as considering all subjects' data (case 2). The average volume of air that was inhaled/exhaled per breath for each subject is also calculated with spirometer and listed in

Table 6-2. It confirms that the subjects were not over emphasizing the breathing movements.

Table 6-2: The average volume of air (liter) inhaled/exhaled per breath for each subject

Subject ID	Normal	Bradypnea	Tachypnea	Cheyn-stokes	Kussmaul	Biot's
1	0.58±0.0036	0.72±0.0249	1.22±9.58E-04	2.78±0.412	3.20±0.003	2.78±0.003
2	0.67±0.0088	1.15±9.33E-04	0.53±6.67E-05	1.32±0.266	2.22±0.0048	2.25±0.0048
3	0.54±0.0015	1.54±0.0021	0.53±6.25E-04	0.88±0.3938	1.34±0.0044	1.70±0.0044
4	0.64±3.00E-04	3.12±0.0171	0.41±0.0014	1.38±0.1649	2.85±0.0033	3.50±0.0033
5	0.80±0.0023	0.93±0.0013	1.51±0.0065	1.27±0.2107	1.83±0.0028	1.36±0.0028
6	0.72±0.0016	1.50±0.0017	0.46±1.00E-04	1.00±0.2632	1.22±0.0013	1.03±0.0013
7	0.40±2.33E-04	0.71±0.0016	0.65±4.33E-04	1.02±0.0544	1.31±0.0018	1.59±0.0018
8	0.64±0.0025	1.71±0.0305	0.58±0.0028	1.15±0.2871	1.42±2.33E-04	1.78±2.33E-04
9	0.59±0.0019	0.79±0.0032	0.83±0.0043	0.93±0.078	2.39±0.0036	2.51±0.0036

Table 6-3: Five samples of pairwise feature combinations and training accuracies for different branches of the proposed classification for case 1 with RBF kernel function

Branch #1			Branch #2			Branch #3		
f_{11}	f_{12}	$A(\%)$	f_{21}	f_{22}	$A(\%)$	f_{31}	f_{32}	$A(\%)$
$\boldsymbol{SD(X)}$	$\boldsymbol{ApEn(Z_N)}$	**98**	$\boldsymbol{SD(Y)}$	$\boldsymbol{Mean(Mag)}$	**100**	$\boldsymbol{SD(Y)}$	$\boldsymbol{SD(X)}$	**100**
$Max(X)$	$Mean(X)$	96	$Mean(X)$	$ApEn(Y_N)$	100	$SD(Y)$	$P(X)$	100
$Max(Y)$	$Mean(Z)$	96	$Corr(X,Y)$	$Max(Mag)$	100	$SD(Y)$	$P(Y)$	100
$SD(X)$	$Max(Y)$	94	$SD(Y)$	$Max(Y)$	98	$ApEn(X_N)$	$ApEn(Y_N)$	100
$Max(Y)$	$E(X_d)$	94	$SD(Y)$	$SD(Y)$	97	$SD(Z)$	$Mean(X)$	95

Branch #4			Branch #5		
f_{41}	f_{42}	$A(\%)$	f_{51}	f_{52}	$A(\%)$
$\boldsymbol{E(Y_d)}$	$\boldsymbol{SD(X)}$	**100**	**SD($\boldsymbol{Y}$)**	$\boldsymbol{P(Z)}$	**100**
$SD(Z)$	$Max(X)$	100	$Max(Z)$	$P(X)$	100
$SD(Y)$	$Mean(Y)$	100	$Max(X)$	$ApEn(Y_N)$	100
$SD(Y)$	$ApEn(X_N)$	100	$SD(Y)$	$Max(Y)$	97
$Mean(X)$	$P(X)$	92	$SD(Y)$	$Max(Mag)$	94

X_d, Y_d, Z_d and Mag_d correspond to X, Y, Z and Mag after removing the DC levels, X_N, Y_N, Z_N and Mag_N are the normalized values of the accelerometer data, *P(.)* is the number of local maxima derived from corresponding signal.

Table 6-4: The best selected pairs of features and training accuracies for different branches of the proposed classification in case 2 with RBF kernel function

Branch #1			Branch #2			Branch #3		
f_{11}	f_{12}	$A(\%)$	f_{21}	f_{22}	$A(\%)$	f_{31}	f_{32}	$A(\%)$
$Corr(X,Y)$	$E(Y_d)$	92	$Max(Y)$	$Mean(Y)$	94	$E(Y_d)$	$ApEn(Z_N)$	98

Branch #4			Branch #5		
f_{41}	f_{42}	$A(\%)$	f_{51}	f_{52}	$A(\%)$
$Mean(X)$	$ApEn(Y_N)$	99	$Max(Y)$	$Max(Mag)$	99

Table 6-5: Selected features and training accuracies for different branches of the proposed classification with different kernel functions for both cases

Case 1

Best Features	Branch #1			Branch #2			Branch #3		
	f_{11}	f_{12}	$A(\%)$	f_{21}	f_{22}	$A(\%)$	f_{31}	f_{32}	$A(\%)$
Linear	$Max(X)$	$Mean(X)$	93	$Max(Mag)$	$Mean(Mag)$	97	$P(Z)$	$E(Mag_d)$	100
Polynomial	$SD(X)$	$ApEn(X_N)$	97	$SD(Y)$	$P(\mathrm{Y})$	100	$SD(Y)$	$SD(X)$	100

Best Features	Branch #4			Branch #5		
	f_{41}	f_{42}	$A(\%)$	f_{51}	f_{52}	$A(\%)$
Linear	$Max(X)$	$ApEn(Z_N)$	100	$SD(Y)$	$P(Y)$	100
Polynomial	$SD(Y)$	$Max(Mag)$	100	$SD(Z)$	$SD(Y)$	100

Case 2

Best Features	Branch #1			Branch #2			Branch #3		
	f_{11}	f_{12}	$A(\%)$	f_{21}	f_{22}	$A(\%)$	f_{31}	f_{32}	$A(\%)$
Linear	$ApEn(Z_N)$	$SD(X)$	81	$SD(Y)$	$Mean(Mag)$	86	$P(Z)$	$E(Mag_d)$	94
Polynomial	$ApEn(Z_N)$	$P(Y)$	89	$SD(Y)$	$SD(X)$	90	$P(Z)$	$SD(Y)$	95

Best Features	Branch #4			Branch #5		
	f_{41}	f_{42}	$A(\%)$	f_{51}	f_{52}	$A(\%)$
Linear	$E(Y_d)$	$ApEn(Y_N)$	97	$Max(Y)$	$P(Z)$	99
Polynomial	$Mean(Y)$	$P(Z)$	97	$SD(Z)$	$SD(Y)$	99

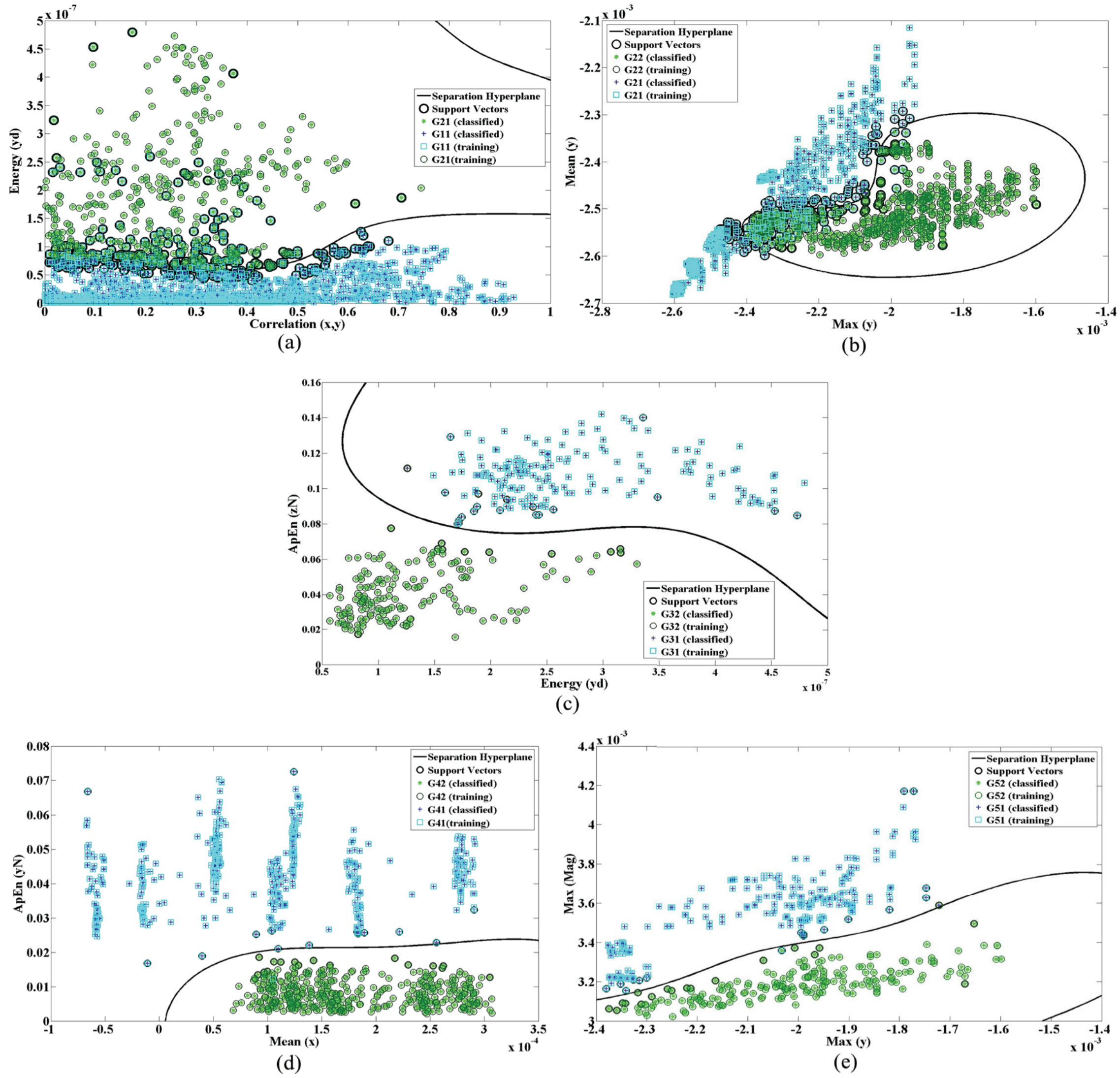

Figure 6-7: Selected features for (a) The first branch (b) Second branch, (c) Third branch, (d) Forth branch (e) and fifth branch of our classification structure with RBF kernel function considering all subjects' data.

As expected, the standard deviation in Cheyn-stokes pattern is more than other types, meaning that subjects were able to correctly change their air volumes in this exercise. Five samples of extracted pairs of features and accuracies in training phase for an individual subject are listed in Table 6-3. The highlighted line corresponds to the best selected features. Table 6-4 also provides the best extracted features in terms of training accuracy while the system is trained with all subjects' data. All simulations are carried out using the Radial Basis kernel Function (RBF) with $\sigma = 1$. The columns labelled $A(\%)$ in Table 6-3, Table 6-4, and Table 6-5 denote the training accuracy calculated by our HSVM classifier for each branch. We use linear and non-linear SVM classifiers on each level of our HSVM structure while training the system with randomly chosen 70% of the data (hold-out cross validation). The performance evaluation is done by testing the remaining 30% of the data. Figure 6-7 (a) shows the energy along axes Y of the accelerometer versus the cross-correlation along dimensions X and Y. The ApEn is applied on the normalized data while energy performs on X, Y, Z and Mag dimensions after removing DC levels.

Figure 6-7 shows the nonlinear trends plot for the different features in all branches of our classification structure while the system was trained with all subjects' data (case 2). There are totally 168 and 42 training trials for G_{11} and G_{12} in case 1, correspondingly. The numbers of trials for training all subjects' data are 1512 and 378, respectively. The processing window for testing data was experimentally selected to be 10sec, which is shifted in increments of 2sec (80% overlap). The average classification accuracy of 94.52% is obtained with RBF kernel function for 9 subjects while the proposed classification is individualized to every subject. In this case, the system is effectively tuned to every individual and the subjects can use the system either at home or during periodic visits to specialist or a physician. The classification performance of 81.29% is also attained when only a single system is trained with using all subjects' data. As performance of SVM depends on the choice of the kernel function, we also evaluate the linear and polynomial kernel functions. Table 6-5 shows the selected features and accuracy for other two types of kernel functions in both cases 1 and 2. The classification of the dataset using the selected features in case 1 gives average accuracies of 94.52%, 93.15% and 84.93% for RBF, polynomial and linear kernel functions, respectively. In addition, we have also executed 10-fold cross validation. In this case, the available dataset is randomly split into 10 folds, where, in turn, 9 subsets are used for the training phase and the remaining as a validation set. The results from evaluating different kernel functions with cross validation are 95.89%, 86.19% and 84.93% for RBF, polynomial and linear kernel functions, respectively. These results demonstrate that there is no over-fitting in the final model. In case 2, the accuracy rates are obtained 81.29%, 78.12% and 69.95% for RBF, polynomial and linear kernel functions, respectively. Therefore, we conclude that for our system (in both cases) the radial basis function results in the best accuracy compared to the other methods.

6.3.2.1 Normal and Impaired Respirations Classification

In another aspect, our classification problem could be modeled as a binary classification for detecting healthy (positive) or unhealthy (negative) subjects. In this case, TP, FP, FN, TN stand for true positive, false positive, false negative and true negative, correspondingly. The performance of the classifier was quantified based on its sensitivity, specificity and the overall accuracy. It is worth mentioning that sensitivity is also called positive class accuracy or true positive rate, while specificity called negative class accuracy or true negative rate. Another parameter often used is the geometric mean of sensitivity and specificity (G-mean) which is defined as the square root of the product between sensitivity and specificity as Eq. (6-21). The average values of sensitivity, specificity and G-mean of SVM classifications for 9 subjects with different kernel functions are shown in Table 6-6. The values of TP, FP, FN, TN are presented according to the logged data of normal and impaired breaths, e.g. there are 18 and 72 testing trials for each subject's normal and impaired breathing patterns, respectively.

$$Sensitivity = \frac{TP}{TP + FN} \tag{6-18}$$

$$Specificity = \frac{TN}{TN + FP} \tag{6-19}$$

$$Accuracy = \frac{TP + TN}{TP + FN + FP + TN} \tag{6-20}$$

Table 6-6: Performance metrics of the classification for case 1 (average of 9 subjects) and case 2

Case 1								
Evaluation parameters	TP	TN	FN	FP	$Sensitivity$	$Specificity$	$Accuracy$	$G - mean$
RBF	18	72	0	0	1	1	1	1
Polynomial	18	67.97	0	4.03	1	0.94	0.95	0.97
Linear	16.28	72	1.72	0	0.90	1	0.98	0.95
Case 2								
Evaluation parameters	TP	TN	FN	FP	$Sensitivity$	$Specificity$	$Accuracy$	$G - mean$
RBF	137	617	25	31	0.85	0.95	0.93	0.90
Polynomial	131	611	31	37	0.81	0.94	0.92	0.87
Linear	120	596	42	52	0.74	0.92	0.88	0.83

$$G - mean = \sqrt{Sensitivity \times Specificity} \quad (6\text{-}21)$$

Therefore, the best classification parameters are achieved for distinguishing between normal and impaired respiration patterns while using RBF kernel function.

6.3.3 Performance Evaluation of Recognition System based on Informative Features

The evaluation of the breath problems classification is performed first through a 10-fold random-partitioning cross-validation process applied across all subjects and breathing patterns. This process is repeated 10 times for each method to ensure the statistical robustness. Then, a Leave-One-Subject-Out cross validation is evaluated in which a single subject is iteratively left out from the training dataset and considered in the test set. The procedure is then repeated for all 10 subject. In fact, as summarized in [203] and according to [204] Leave-One-Subject-Out is the best technique for risk estimation, whereas 10-fold is the most accurate approach for model selection. The effects of the segmentation, sensor placement, number of sensors as well as different sampling rates on the classification performance are discussed in the next sections.

6.3.3.1 Data Segmentation Analysis

In this section, we analyze the effects of the windowing operation on the breath disorders classification process. The results for different window sizes of two segmentation techniques, i.e. FNSW and FOSW, for each specific classifier are depicted in Figure 6-8. These results are obtained based on two accelerometer sensors and all features. We have swept the window size from 5 to 15 sec while five different overlap values including 0.10, 0.25, 0.50, 0.75 and 0.90 are considered. The best performance accuracy of FNSW and FOSW with all overlap values are highlighted in Figure 6-8 (a)-(f). For example, Figure 6-8 (a) indicates that the best accuracy reaches 91% with DTB classifier and non-overlap fixed size windowing method. Obviously, the outermost layers in Figure 6-8, indicate high performance accuracy. It can be observed that SVM obtains the maximum accuracy of 97.50% with the window size 13 sec and overlap 0.90

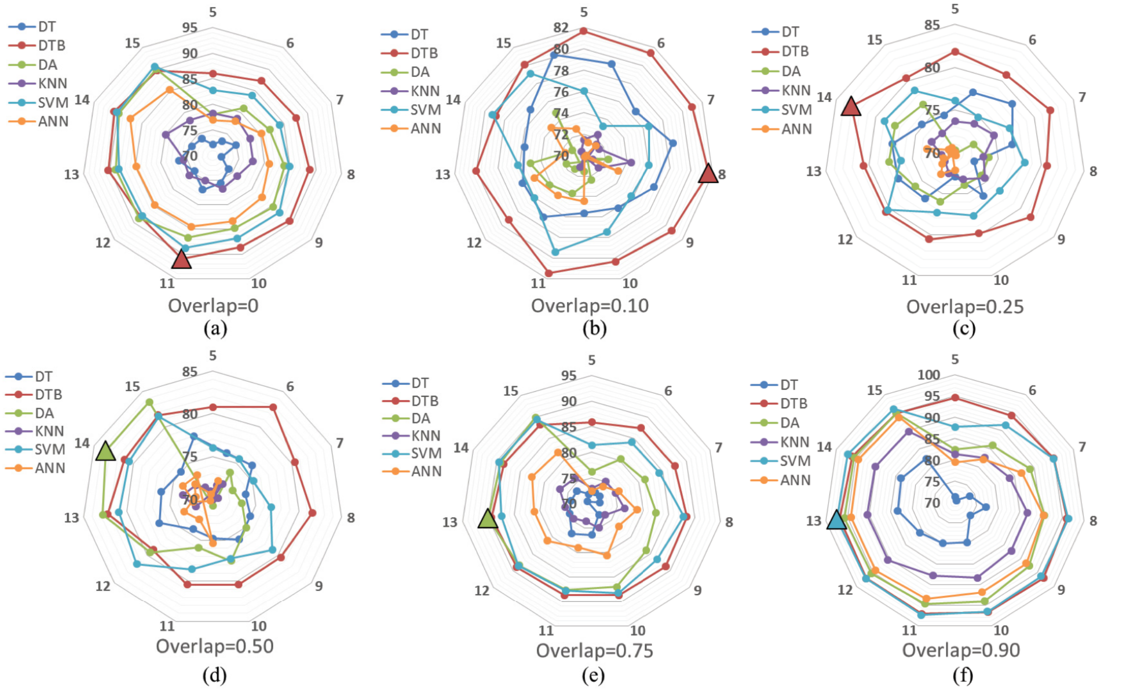

Figure 6-8: Accuracy rates with two sensors and all features for (a) FNSW segmentation, (b)(c)(d)(e)(f) FOSW with 0.10, 0.25, 0.50, 0.75 and 0.90 overlap values, respectively

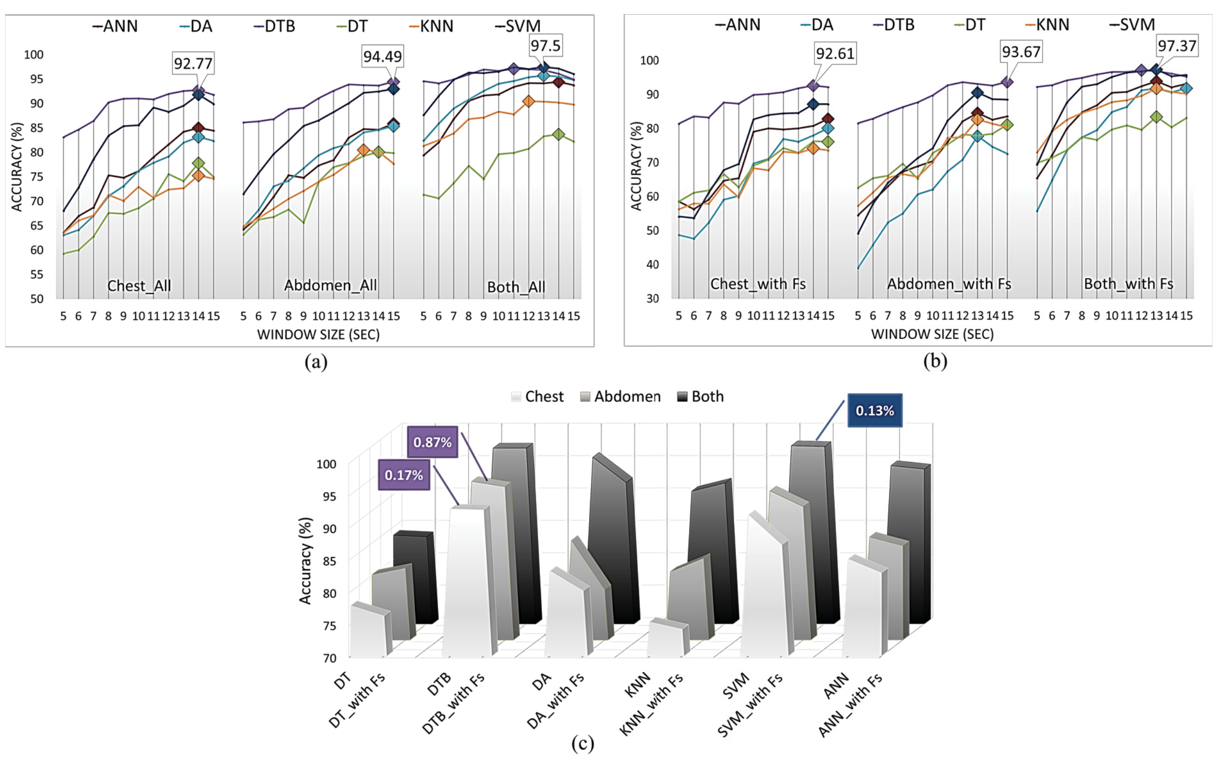

Figure 6-9: (a)The classification accuracy for six methods with overlap = 0.9 and different window sizes considering three scenarios with all features and (b) after CFS feature selection (c) the best accuracy rates with all features and with FS for three scenarios

(see Figure 6-8 (f)). The accuracy decreases by 6.93% considering Leave-One-Subject-Out evaluation.

6.3.3.2 Discussions on the Number of Sensors, Sensor Placement and Feature Selection

The effect of the number of sensors on accuracy rate is shown in Figure 6-9. The DTB and SVM models are shown to be quite robust considering their moderate performance drop by reducing the number of sensors. DTB proves to be the most accurate model in case of using a single accelerometer. The best accuracies of 92.77% and 94.49% are achieved for sensors on chest (Acc1) and abdomen (Acc2) with all features (Figure 6-9 (a), (c)), respectively. These rates drop by 7.19% and 6.83% with Leave-One-Subject-Out cross validation. The assessments are computed based on FOSW segmentation with overlap value 0.9 and widow size 14 sec and 15 sec for Acc1 and Acc2. An improvement is observed for the case of using both sensors with SVM classifier by approximately 4%. Therefore, decreasing the number of sensors represents a reduction of classification accuracy. It is also worth mentioning that using the accelerometer on the abdomen umbilical region overcomes the performance obtained from the sensor on the middle of sternum region. This is due to the movement mechanism of upper rib cage (RC) and lower rib cage/abdomen (AB) during respiration function [121]. Based on [121] the lower six ribs have a greater ability to move independently compared to the upper six ribs. Due to this fact, the breathing signals collected from Acc2 resulted in better classification accuracy compared to Acc1.

The impacts of CFS feature selection is also plotted in Figure 6-9 (b) and (c). In order to avoid overoptimistic performance evaluation in the machine learning models, the feature selection has been applied only on training dataset. After feature selection, the number of features for the best accuracy cases are reduced from 55 to 19 for two sensors and 26 to 14 for a single sensor either on the chest or abdomen locations (listed in Table 6-7). The results depicted in Figure 6-9 (a) and (b) are achieved with the same segmentation methods, window sizes and overlap values. At first glance, the performance tendency is decreased in most cases after feature selection; however, using kNN classifier with two sensors or kNN/DT with one sensor on abdomen, the situation is quite opposite. The best results after feature selection are obtained 92.61%, 93.67% with DTB and 97.37% with SVM, using Acc1, Acc2 and both sensors, respectively. Therefore, despite a small drop in accuracy (less than 1%), we could reduce the redundancy among features by 65.45% for two sensors and 46.15% for a single sensor conditions. Figure 6-9 (c) is devised as a good means to visually inspect the performance trade-off in applying feature selection. Figure 6-10 summarizes the achieved classification and misclassification rates for each class. These results are for the best classifiers in terms of overall accuracies with all features and after feature selection. The classification parameters are computed as follows:

$$ClassificationRate(i) = \frac{CM(i,i)}{\sum_{j=1}^{l} CM(i,j)} \times 100 \tag{6-22}$$

$$MisclassifcationRate(i) = \frac{\sum_{j=1,i\neq j} CM(i,j)}{\sum_{j=1}^{l} CM(i,j)} \times 100 \tag{6-23}$$

Where, the $ClassificationRate(i)$ is the proportion of predicted class i which actually belongs to i_{th} class. And $MisclassificationRate(i)$ indicates the false predicted portions of class i into class j. Figure 6-10 (a)-(c) identify the misclassification rates with all features and after feature selection as well as the classification rates when a single sensor is used on the subjects' chest. For example, in Figure 6-10 (a), to determine whether a respiration disorder is the OSA breathing pattern, the classifier misclassifies it as Sighing breathing for 5% and normal for 3.68%, resulted in classification rate of 91.32% shown in Figure 6-10 (c). After feature selection, in Figure 6-10 (c) the classification rate reduces to 90.53% representing the misclassification rates of 5% and 4.47% with Signing and normal breathing patterns plotted in Figure 6-10 (b). Therefore, the use of more features could be of interest to separate as much as possible the diverse classes and reduce the breath patterns' confusion likelihood. Furthermore, based on the observations in Figure 6-10 (g)-(i), in case of using two accelerometer sensors, all misclassification rates are kept below 5.5% which indicates a high recognition rate (> 94.5%) for each class, individually. The accuracy values after feature selection with Leave-One-Subject-Out cross validation are obtained 85.15%, 88.44%, and 89.75% with Acc1, Acc2 and both sensors, respectively. This is due to the subject-to-subject variation that occurs during validation of the models.

6.3.3.3 Sampling Rate Analysis

Another important point of discussion is how to reduce computations, storage, and energy consumption by means of reducing sampling rate in our online recognition system.

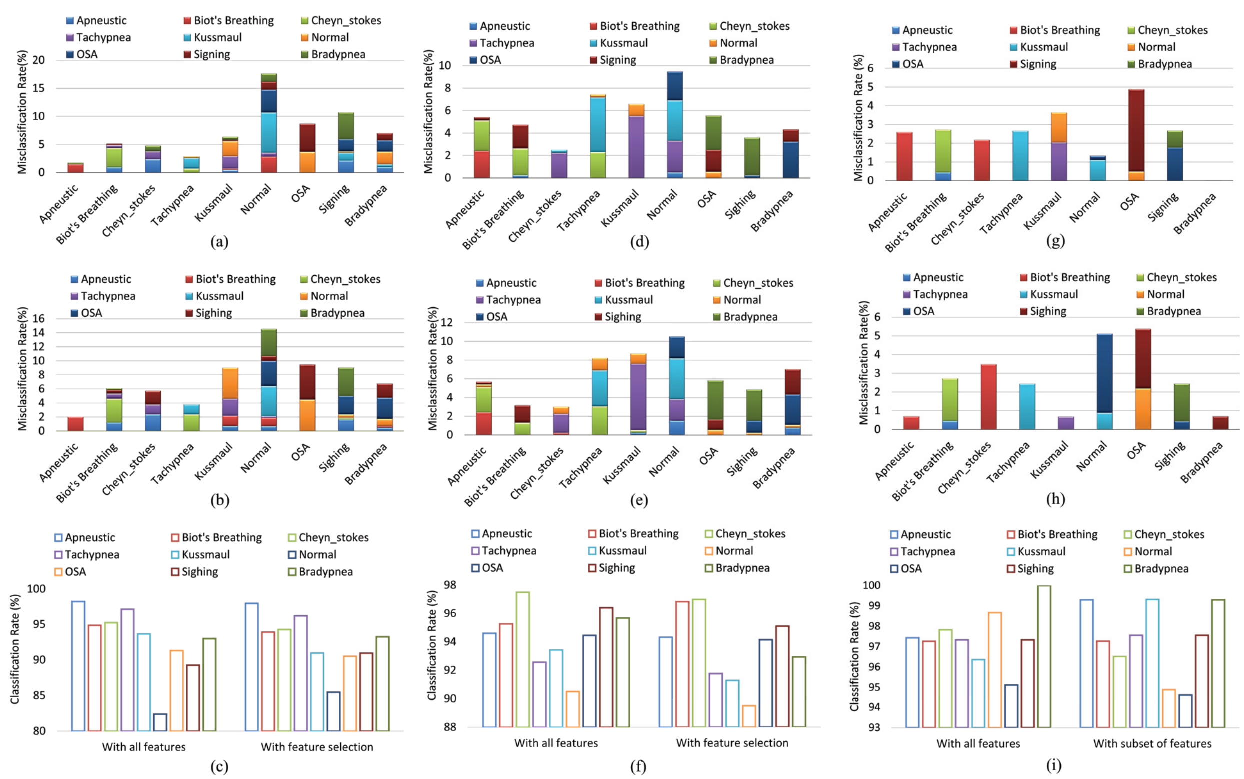

Figure 6-10: Misclassification rates for the best obtained classifiers based on 10-fold cross validation with (a) Acc1, (d) Acc2 and (g) two sensors with all features, Misclassification rates for the best obtained classifiers with (b) Acc1, (e) Acc2 and (h) two sensors with CFS feature selection, Classification rates for the best obtained classifiers with (c) Acc1, (f) Acc2 and (i) two sensors

Table 6-7: Feature sets with two sensors and single sensor

Feature set for a single sensor						
$Mean(Z)$	$SD(Z)$	$RR(Y)$	$RR(Z)$	$TV(Z)$	$TV(Y)$	SAX(Y)
$TV_{var}(Z)$	$TV_{var}(Y)$	$T_e(Z)$	$T_e(Y)$	T_i(y)	$T_i(Z)$	SAX(Z)

Feature set for two sensor									
$Mean(Z_1)$	$SD(Z_1)$	$SD(Y_2)$	$Pitch$ (Acc2)	$RR(Z_1)$	$RR(Y_2)$	$TV(X_1)$	$TV(Y_1)$	$TV(Z_2)$	SAX (Z_2)
$TV_{var}(Z_1)$	$TV_{var}(Z_2)$	$T_e(Z_2)$	$T_e(X_1)$	$T_i(Z_2)$	$T_i(Y_2)$	$\theta(Y)$	SAX (Y_1)	SAX (Z_1)	

Indices “1” and “2” refer to Acc1 (Accelerometer on the chest of subject) and Acc2 (Accelerometer on the abdomen of subject).

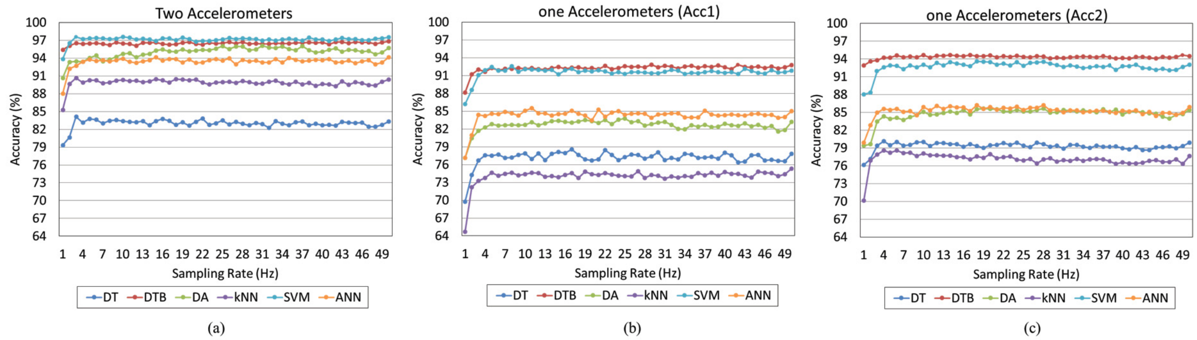

Figure 6-11: Accuracy values for different sampling rates in applying (a) two sensors, (b) Acc1, and (c) Acc2

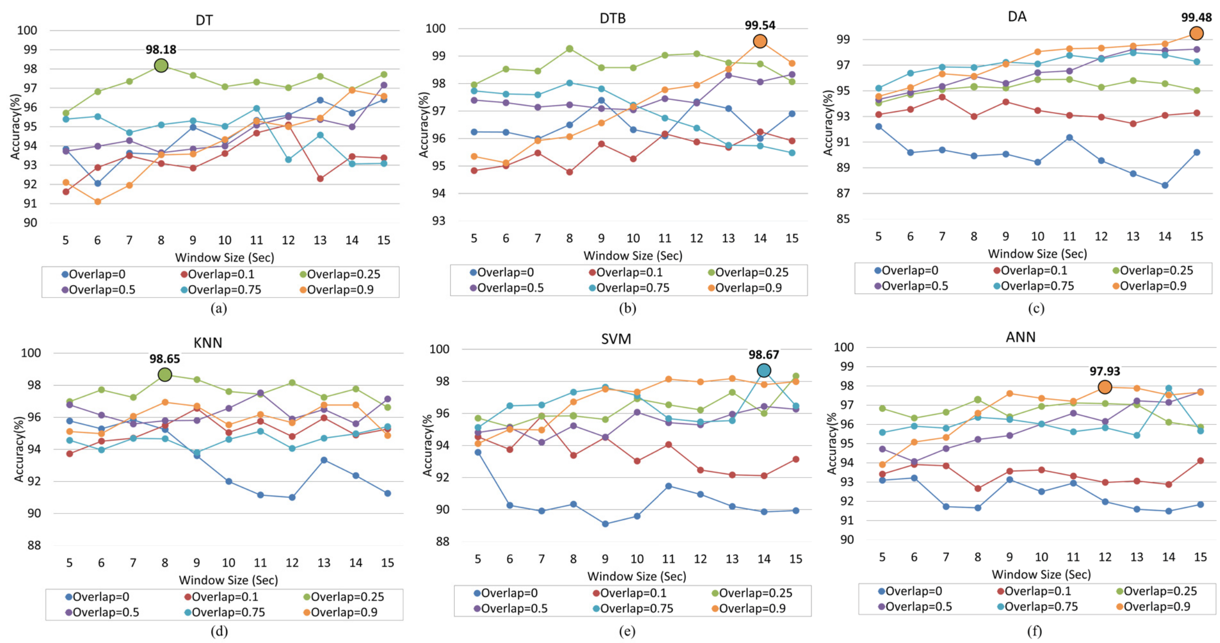

Figure 6-12: Accuracy rates for (a) DT, (b) DTB, (c) DA, (d) kNN, (e) SVM, (f) ANN classifiers for all overlap values in binary classification

The sampling rate should be carefully chosen to guarantee a reasonable response time and battery life while keeping the accuracy sufficiently high. We test whether the classification problem can allow the sampling rate to be reduced so that we can increase energy efficiency. This would permit to use smaller size batteries and hence increase the comfort of the wearable system. In our experiment, we have swept the sampling rate (by resampling explained in Chapter 4) from 1Hz to 50Hz for the best model obtained from either two sensors or single accelerometer on the upper

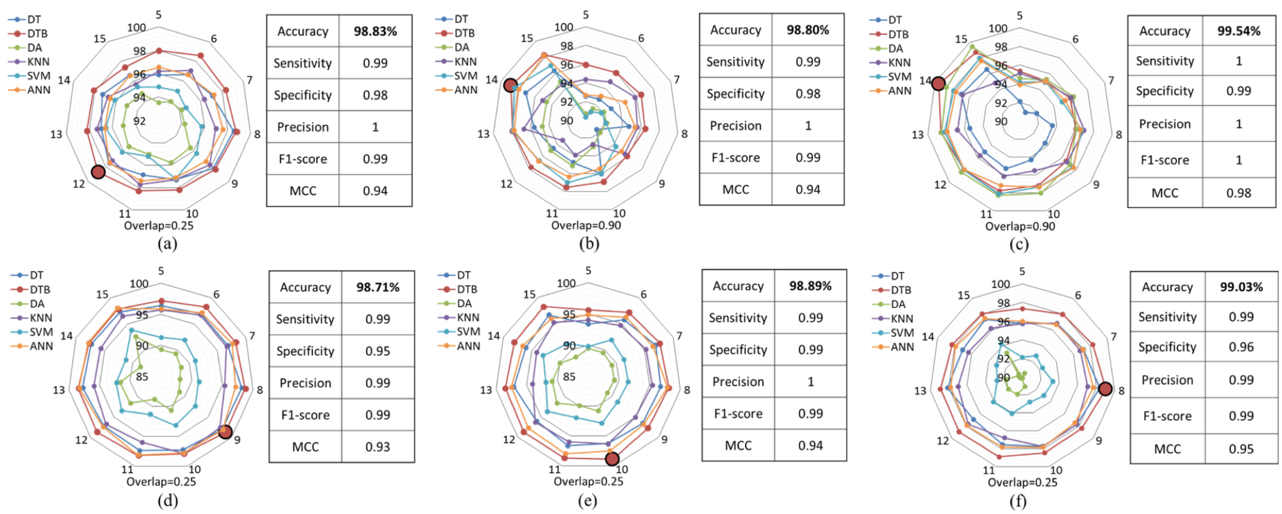

Figure 6-13: The best results in terms of accuracy with all features and 10-fold cross validation (a) Acc1 (b) Acc2 and (c) two sensors, the best results in terms of accuracy after feature selection and 10-fold cross validation (d) Acc1 (e) Acc2 and (f) two sensors

body of the subjects with all features. Figure 6-11 displays the behavior of the recognition accuracy as a function of the accelerometer sampling rate in all six classifiers.

Interestingly, we found that no significant gain in accuracy is achieved for sampling rate above 4 Hz. In other word, the performance of breathing disorders classification was insensitive to a reduction in sampling rate from 50Hz to 4Hz for inertial sensors. Therefore, it is concluded that low-frequency sampling of accelerometer data can lead to classification results competitive with previous results with much higher sampling rates.

6.3.3.4 Binary Classification

In this section, the results corresponding to the evaluation of the proposed binary classification are presented. Six classifiers are tested in three scenarios: accelerometer on the chest (Acc1), on the abdomen (Acc2) and in both locations. The best overall accuracy of 99.54% is obtained with DTB classifier for the case of applying two sensors with all features. As shown in Figure 6-12 (b) the best accuracy occurs when window size is set to 14 sec with overlap 0.9. The lowest performance is achieved for a window size of 14 sec, with DA classifier and overlap 0.75 depicted in Figure 6-12 (c). Nevertheless, the DA classifier provides the second best performance of 99.48% along with window size 15 sec and overlap value 0.9. For the single sensor scenarios (Acc1, Acc2), the overall accuracy rates of 98.83% and 98.80% are obtained, correspondingly. All results are based on a 10-fold cross validation process within 10 iterations. We also provide results with CFS feature selection summarized in Figure 6-13. The upper plots (Figure 6-13 (a), (b) and (c)) show the best results which are obtained in terms of accuracy with all features.

Due to the imbalanced normal and abnormal datasets, there is no single statistic, which can adequately evaluate or rank the classifiers. Therefore, in this section, we adopted six evaluation measures to show the performance of selected model: sensitivity (Eq. (6-18)), specificity (Eq. (6-19)), accuracy (Eq. (6-20)), precision, F1-score and Matthews Correlation Coefficient (MCC), as defined below.

$$Precision = \frac{T_P}{F_P + T_P} \tag{6-24}$$

$$F1 - score = 2\times\frac{Precision\times Sensitivity}{Precision + Sensitivity} \tag{6-25}$$

$$MCC = \frac{T_P\times T_N - F_P\times F_N}{\sqrt{(T_P + F_N)(F_P + T_P)(F_P + T_N)(F_N + T_N)}} \tag{6-26}$$

Where T_P is the number of true positives, i.e., proportion of actual healthy patterns, which are predicted as "healthy". T_N is the number of true negatives, i.e., proportion of actual unhealthy patterns which are predicted as "unhealthy", F_P (False Positive) refers to the proportion of actual healthy patterns which are predicted as "unhealthy", and F_N (False Negative) defines as the proportion of actual unhealthy patterns which are predicted as "healthy". Sensitivity is the probability that a test pattern will be classified as "healthy" among those healthy patterns. While the specificity is the fraction of those with breath problems who will have an "unhealthy" test result. Precision shows the proportion of predicted healthy pattern, which are actual "healthy". The F1-score is a combination of precision and sensitivity measures. It has a range between [0,1], where one represents an optimal recognition capability, whilst zero corresponds to a system that is not capable of recognition at all. Finally, the MCC is a measure of how well the predicted class labels correlate with the actual class labels. An MCC of 1 corresponds to the perfect prediction, -1 indicates the worst possible prediction; and an MCC of 0 corresponds to a random guess.

We could achieve all performance parameters above 0.94 when all features are considered listed in Figure 6-13 (a), (b) and (c). For example, with single accelerometer sensor, the selected models provide the Matthews Correlation Coefficient above 0.94. Whereas for the best model with two sensors and all features, the MCC is close to one (0.98). Besides, the high sensitivity and specificity values (> 0.98) denote that how well the achieved models predict both categories. After feature selection, all best models are obtained from overlap value 0.25 and DTB classifiers. Indeed, the classification with subset of features leads to performance degradation for the cases of using Acc1 (Figure 6-13 (d)) and two sensors (Figure 6-13 (f)). Conversely, accelerometer on the abdomen (Figure 6-13 (e)) copes with the challenge of decreasing the number of features while providing better performance parameters compared to the results shown in Figure 6-13 (b). Furthermore, the F1-score values are more than 0.99 in all cases specifying optimal discrimination capabilities of the final classification models. It can be also concluded that, two sensors deliver a bit stronger discrimination accuracy by approximately 0.72% (with all features) and 0.23% (after feature selection) compared to a single sensor either on the chest or abdomen location.

Table 6-9 listed the previous related studies described in Chapter 2. It is worth mentioning that, the accuracy rate for each study is computed with different sets of subjects as well as various settings and methods. Based on this assumption, the proposed accelerometer-based binary classification can outperform the results obtained from the prior models trained by sound, airflow, ECG or the combination of these signals.

6.3.4 Performance Evaluation of the Evolutionary Hierarchical Model

The experimental results are validated on the second group of subjects explained in section 6.3.1 with 10-fold cross validation. The recognition of each test pattern starts from the root of the tree. At each intermediate node of the binary tree, a decision is made about the assignment of the input pattern into one of the two possible groups: left or right sub-tree. Each of these groups may contain multiple classes. This is repeated recursively downward the tree until the sample reaches a leaf node that represents the class in which the pattern belongs to. Figure 6-14 shows the accuracy versus sensitivity for all population and generations.

The worst-case sensitivity S is represented in the horizontal axis and accuracy rate (A) on the vertical axis. A point (tree) in (S, A) space dominates another if it has higher accuracy and equal or greater S, or if it has greater S and equal or better accuracy rate. The accuracy and minimum sensitivity measures verify that:

$$S \leq A \leq 1 - (1 - S)p^*$$

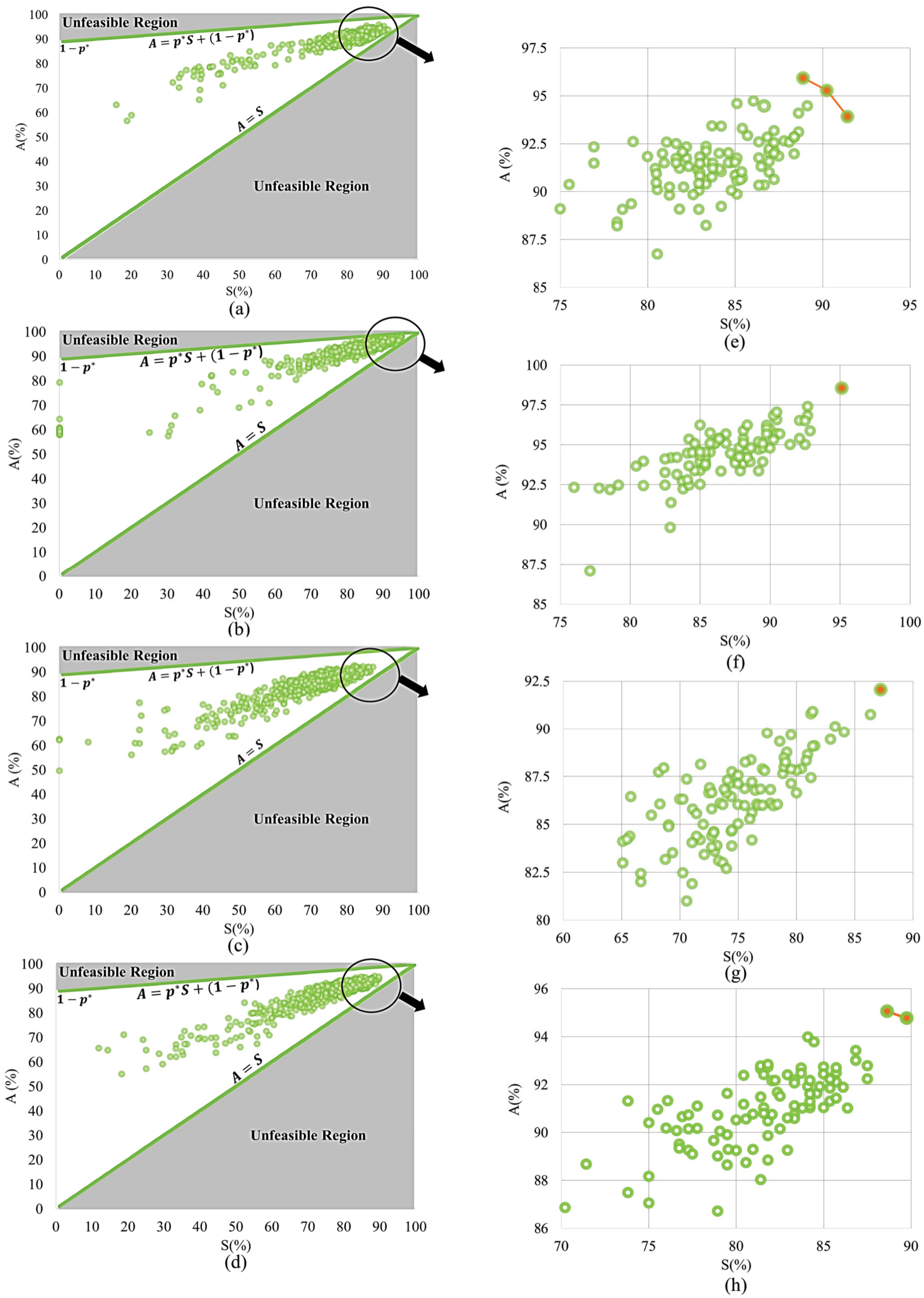

Figure 6-14: Feasible and unfeasible regions in the 2-D (*S, A*) space for (a) Acc1 with all features, (b) Acc2 with all features, (c) Acc1 after feature selection, (d) Acc2 after feature selection (e), (f) , (g), (h) Pareto fronts for all cases in testing with 10-fold and 50 iterations, correspondingly.

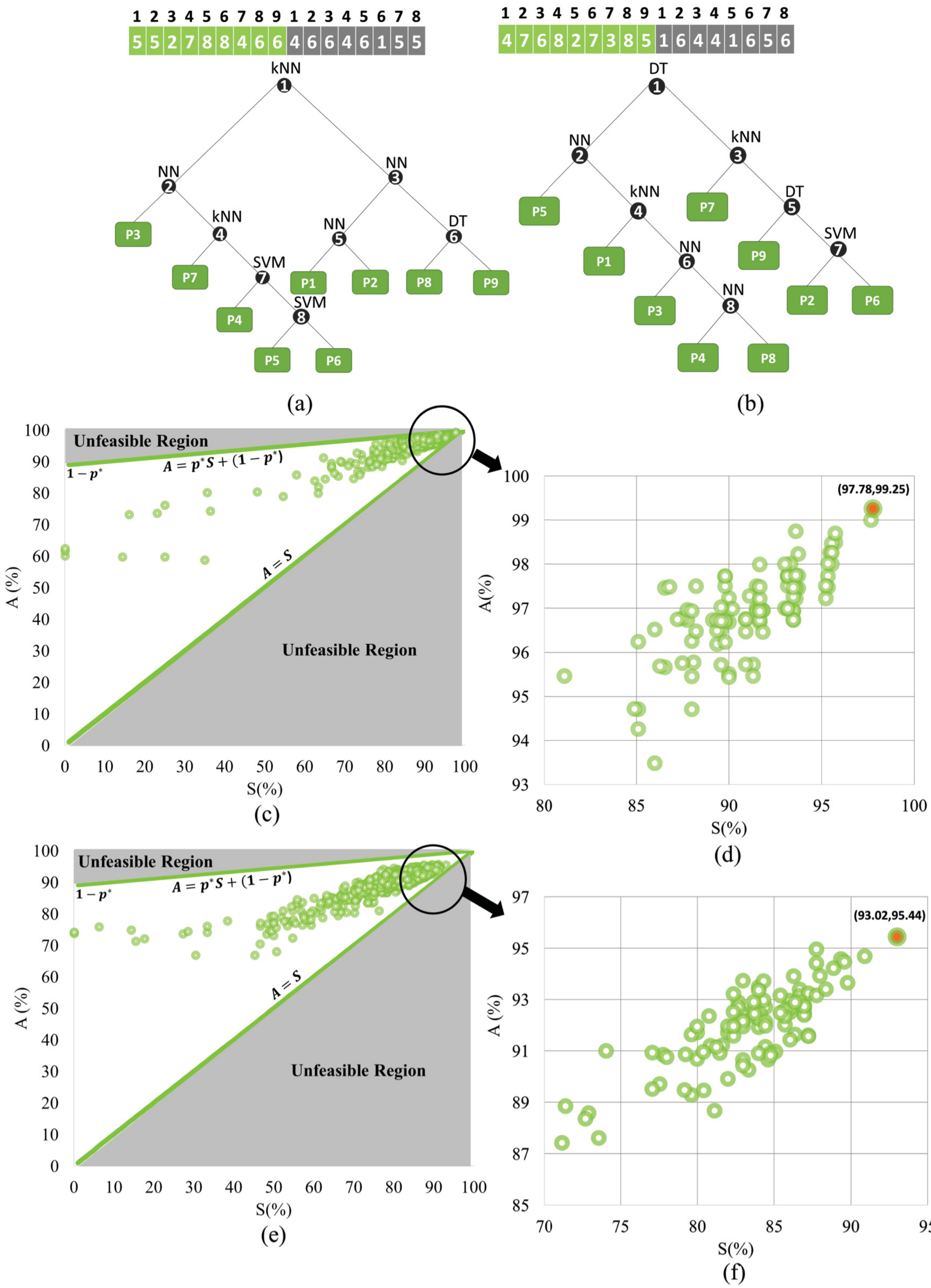

Figure 6-15: (a)-(b) The best classification models before and after feature selection with two sensors, (c)-(d) feasible and unfeasible regions in the 2-D (*S, A*) space with two sensors and all features, (e)-(f) feasible and unfeasible regions in the 2-D (*S, A*) space with two sensors after feature selection

Where p^* is the minimum of the estimated *prior* probabilities and in our balanced classification problem with l classes is equal to $\frac{1}{l}$. Therefore, each tree is denoted as a point in the white region in Figure 6-14 (a)-(d) and the gray area is marked as the unfeasible regions. Figure 6-14 (a) and (b) show the results when we have one sensor on the chest and abdomen, respectively. Figure 6-14 (e)-(h) show zoomed portions of the feasible solutions. In the first scenario (Acc1) we could obtain three points distributed on the Pareto front. The maximum accuracy of 95.94% is obtained with 88.89% worst-case sensitivity while the maximum S is obtained 91.43% by 93.92% accuracy rate. In case of using accelerometer sensor on the abdomen region (Acc2) the best point (95.12%, 98.55%) is achieved for (S, A) which again dominates the results derived from Acc1.

Figure 6-14 (c), (d), (g), (h) show the results after CFS feature selection. The redundancy among features is reduced by an average of 66.66% (from 27 to 9 features) for a single sensor condition while the best points shifted to (87.23%, 92.06%) for Acc1 and {(89.74%, 94.77%), (88.64%, 95.06%)} for Acc2. Thus, the system suffers by less than 5.5% for both accuracy and worst-case sensitivity. Therefore, the use of more features could be of interest to separate as much as possible the diverse classes and reduce the possibility of the breathing patterns confusions.

The best classification models with two sensors are obtained with (97.78%, 99.25%) and (93.02%, 95.44%) with all features and after feature selection, correspondingly (see Figure 6-15). The best models are depicted in Figure 6-15 (a) and (b). The mean number of features is reduced from 55 to 14 (74.55%) by a drop of less than 4% in accuracy and 5% in worst-case sensitivity. Therefore, the results guarantee that each class is individually classified with more than 97% with all features and 93% after feature selection. Table 6-8 compares the previous results explained in section 6.3.3

Table 6-8: Comparison between single objective and multiobjective techniques

The best results of single objective techniques (section 6.3.3)					
	Acc1+Acc2	Acc1			Acc2
A(%)	97.50%	92.77%			94.49%
S(%)	95.12%	82.38%			90.51%
The results of multiobjective technique					
	Acc1+Acc2	Acc1			Acc2
A(%)	99.25	93.92	95.28	95.94	98.55
S(%)	97.78	91.43	90.24	88.89	95.12

and the new results based on the proposed hierarchical tree-structured models. It is demonstrated that, in all scenarios, the introduced models can surpass the previous single objective techniques in terms of both accuracy and sensitivity. The results verified that, the combination of the results obtained by different hierarchical classifiers improves the outcomes that each provides, individually.

6.4 Summary

With the growth of sensor technology and the data analysis methods, diagnosis systems based on wearable sensors carry the advantages of simple setup, high reliability and accuracy as well as providing useful information for health-related applications. In this chapter, we exploited recent advances in wearable sensing and machine learning principles to provide innovative decision making capabilities for subjects' breathing characteristics and to discern valuable information. First, we start with designing a hierarchical tree-structured SVM classifier with well-known time domain features and a low-cost feature selection technique. The results were evaluated for two cases: each individual and with all individuals' data. Then, novel approaches were discussed for extracting information-rich features to enhance the machine learning model while the number of breathing patterns were increased, as well. The selected features feed six different classifiers and the best models are obtained considering extensive sets of performance metrics. Finally, a multiobjective approach was developed to optimize the accuracy rate as well as the worst-case sensitivity on our multi-class classification problem. An evolutionary algorithm was applied which attempts to intelligently get closer and closer to the best hierarchical model. The assessments indicated that, the combination of the classifiers in a hierarchical structure outperforms the results obtained by each classifier in a single objective problem.

Table 6-9: List of previous related work for binary classification of normal and abnormal breathing patterns

Ref#	Technique	Detection	Wireless	Accuracy (%)
This work	DTB	Normal/Abnormal (9 types)	Yes	Accelerometer
[119]	HMM	Normal/Abnormal	No	Microphone
[118]	HMM	Normal/Abnormal	No	Microphone
[117]	HMM	Normal/Abnormal	No	Microphone (Lung+Hearth sounds)
[116]	SVM	Normal/Abnormal (2 types)	No	Microphone
[115]	NN	Normal/Obstructive+Restricted	No	Spirometer
[114]	RBF NN	Normal/Obstructive breathing	No	Spirometer
[113]	NN	Normal/Restricted breathing	No	Spirometer
[112]	NN	Normal/Obstructive+Restricted+Mix	No	Spirometer
[111]	SVM	Normal/Apnea/Hypoapnea	No	Airflow (oronasal airflow)
[109]	SVM	Normal/Apnea	No	ECG
[108]	Hierarchical Bayesian	Normal/Apnea	No	ECG
[107]	Regression Tree	Normal/OSAS	No	ECG+EEG+EOG+Pulse Oximetry
[106]	Quadric Discrimination (QD)	Normal/Apnea(OSA or Mixed)	No	ECG (Single lead)

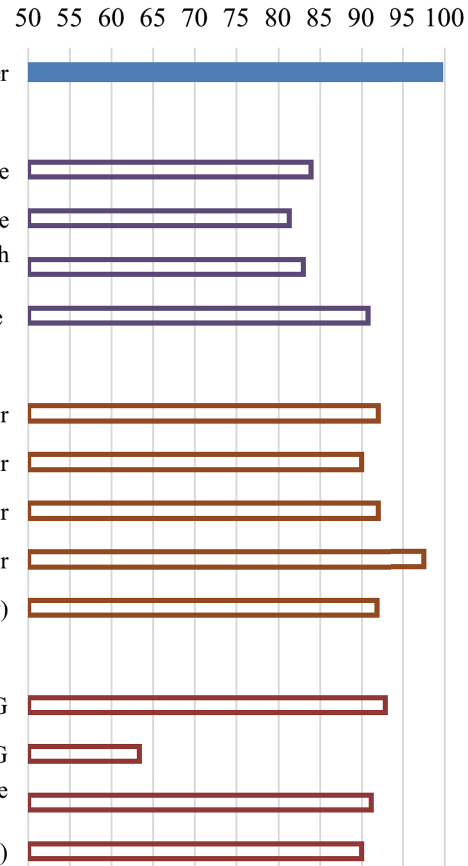

Chapter 7

A Real-Time Biofeedback During Breathing Therapy

To complete our platform, we have added the concept of “Breathing Therapy” as an innovative way for helping people to learn the science of breath in a systematic way. We employ Dynamic Time Warping (DTW) to identify all subsequences within a continuous sensor data stream that are similar to a given reference pattern. An online biofeedback is provided based on the distance vector derived from DTW to make aware the users about their practices quality. So that, it potentially lifts the people's motivation up towards treatment while accurately tracks their real condition and improvement at low cost. The proposed technique could be further integrated in virtual reality frameworks, as well.

7.1 Motivation

Human beings naturally do not need any instruction in breathing. They breathe, the way nature intended them to do, however they have contracted wrong methods of walking, standing and sitting, which have robbed them of their birthright of natural and correct breathing [122]. Different researches [122] show that the physical health depends very materially upon correct breathing. In addition to the physical benefit derived from correct habits of breathing, people’s mental power, happiness, self-control, clear-sightedness, morals, and even their spiritual growth may be increased by an understanding of the "Science of Breath" [122].

The breath exercises as well as yoga breathing maneuvers were widely used as a means of self-regulation and restoration of mental and emotional balance in India and now are also in the area of modern respiratory psychophysiology [205]. Ancient systems such as Indian yoga pranayama which refers to the “Control of breath in specific postures” directs the curative power of air energy to the certain parts of human body and through this benefit the health of the mind and body [205].

According to [122], if one does not breathe in a sufficient quantity of air, the blood circulation system does not work properly, which may cause various disease symptoms. The blood of people who breathe improperly is of a bluish, dark colour, lacking the rich redness of pure arterial blood resulting in a poor complexion. In contrast, correct breathing function, and a consequent good blood circulation can result in a clear, bright complexion. Breathing is highly sensitive to physiological and psychological arousal and metabolic activity [206] and can be controlled voluntarily to serve as an entry point for physiological and psychological regulation [207].

An average people takes about 21,000 breaths per day and 10.5 million breaths per year. Breathing is often denoted as a bridge, connector or channel between the body and mind since there is an inter-relationship between emotions, mental processes, patterns of body tension and breathing [208]-[210]. It is also worth noting that visualizing something in the brain can encourage the body to make it happen. For that reason, in this section, we introduce a new technique based on wearable and wireless sensory system to bring cutting edge technology into breathing therapy area. Such a system enthuses people with a vision for quality and informs them of their progress in performing the prescribed breathing models. We utilize a robust algorithm to analyze the signals and provide rich feedback on performance accuracy in breathing therapy. Although the present cutting edge technologies are predominantly in the research domain, they will almost certainly enter routine clinical use in the near future.

7.2 The Proposed Breathing Therapy Framework

In this section, we have analyzed the motion of humans’ chest compartments via a motion sensor in different yogic breathing practices for designing our online biofeedback breathing therapy platform. In the proposed system, first the users are asked to perform the breathing patterns under supervision of specialists to record a golden standard profile (reference pattern) while the accelerometer sensor is worn on their abdomen. Then, the testing patterns are compared with the reference automatically, once the users are performing the prescribed exercises on their own at home. Through visual feedback on performance accuracy of each breath, people are informed how well they are executing the patterns.

The samples received from motion sensors carry noise and applying denoising algorithms is essential to facilitate accurate assessment of human respiration signal. Hence, both test and reference patterns are smoothed by a 29-point frame third order Savitzky-Golay (SG) smoothing filter since it does not delay the signal and is able to preserve features such as local minima and maxima. This filter is optimal in the sense that it minimizes the Least-Squares Error (LSE) in fitting a polynomial degree three to frames of noisy data. To provide the biofeedback, we make use of Dynamic Time Warping with our proposed new segmentation technique, which is described in the next sections.

7.2.1 A Brief Review of Dynamic Time Warping (DTW)

DTW has been originally used to compare different speech patterns and also extensively studied in the clustering algorithms [211]. It is very applicable for measuring similarity between time series by providing metric that summarizes the Euclidean distance along the warping path. Indeed, DTW leverages the impacts of amplitude variance and speed variance of the time series signal [212].

We employ DTW to identify all subsequences within a continuous sensor data stream that are similar to a given reference pattern. Here is the formal definition of classical DTW [213]. Assume that we have two time sequences, X and Y, of length N and M, respectively, where:

$$X := (x_1, x_2, \dots, x_N), \qquad N \in \mathbb{N} \tag{7-1}$$

$$Y := (y_1, y_2, \dots, y_M), \qquad M \in \mathbb{N} \tag{7-2}$$

An (N, M)-warping path is a sequence $P = (p_1, p_2, \dots, p_l)$ with $p_l = (n_l, m_l) \in [1{:}N]\times[1{:}M]$ for $l \in [1{:}L]$ which assigns x_{n_l} the element of X to y_{n_l} the element of Y and should satisfy the following conditions:

(i) Boundary condition: $p_1 = (1,1)$ and $p_L = (N, M)$

(ii) Monotonicity condition: $n_1 \leq n_2 \leq \cdots n_L$ and $m_1 \leq m_2 \leq \cdots m_L$

(iii) Step size condition: $p_{l+1} - p_l \in \{(1,0),(0,1),(1,1)\}$ for $l \in [1: L-1]$.

The cost of a warping path p between X and Y is defined as:

$$c_p(X,Y) \coloneqq \sum_{l=1}^{L} c\left(x_{n_l}, y_{m_l}\right) \tag{7-3}$$

Which $c(x_n, y_m)$ is the Manhattan distance (absolute value of the difference) between x_n and y_m. A warping path actually defines an alignment between two sequences X and Y. The alignment is optimal in the sense that a cumulative distance measured between the aligned samples is minimized [214]. It means we require to find the optimal warping path (p^*) between X and Y which has the minimum total cost among all possible warping paths. The matching cost considered as an indicator of the similarity of two patterns is defined as:

$$\begin{aligned} Matching\ Cost &= DTW(X,Y) = c_{p^*}(X,Y) \\ &= min\left\{c_p(X,Y) \mid p\ is\ an\ (N,M)-warping\ path\right\} \end{aligned} \tag{7-4}$$

To determine an optimal path p^*, the exhaustive search leads to an exponential computational complexity; however, applying dynamic programming makes it possible to compute the cost matrix D with $O(MN)$ operations. The accumulated cost matrix D satisfies the following identities:

$$D(n,1) = \sum_{k=1}^{n} c(x_k, y_1)\ \ for\ n \in [1: N], \tag{7-5}$$

$$D(1,m) = \sum_{k=1}^{m} c(x_1, y_k)\ \ for\ m \in [1: M] \tag{7-6}$$

$$\begin{gathered} D(n,m) = \min\{D(n-1,m-1), D(n-1,m), D(n,m-1)\} + c(x_n, y_m) \\ for\ 1 < n \leq N\ and\ 1 < m \leq M \end{gathered} \tag{7-7}$$

$$D(N,M) = \ Matching\ Cost = \ DTW(X,Y) \tag{7-8}$$

This study introduces the use of DTW with a new segmentation technique to calculate the similarity between the reference and test patterns while providing a graphical feedback in real-time. Therefore, such a system can support abnormal breathing detection as well as a systematic breathing therapy visualization component.

7.2.2 The Proposed Method

In our experiments, the data stream is segmented according to the reference pattern, and the similarity is computed on each window. Algorithm 7-1 summarizes the proposed breathing therapy procedure. For calculating the signal similarity, the algorithm checks whether a window of new instances is ready in our data stream ($sensorData$) in line 6. Otherwise, the procedure keeps collecting the new instances of accelerometer data in lines 3, 4 and 5. The dissimilarity/distance of reference and test signals is calculated in line 7. Here, X and Y are the reference and test signals, correspondingly. The processing window size (W) is set to a value equal to the length of the reference pattern (N). The variable S refers to the starting point of the window. This variable is updated in lines 9 and 11 based on the overlap value (O_v), which is set to 0.9 in our experiments. When the DTW distance of the current window is larger than the previous window (line 8), the starting point will be updated to the end of the last window (line 9) resulted in skipping ($\left\lceil \frac{O_v}{1-O_v} \right\rceil -$ 1) processing windows to speed up the procedure. Otherwise, it is updated to the next processing window based on O_v value. Figure 7-1 briefly describes the segmentation method for one selected breathing pattern derived from the accelerometer. The arrows show the starting points of the windows. In this example, as you can see, there are 5 cases in which the sliding window jumps forward (e.g. from window 2 to 3) resulted in reducing the number of processing windows by about 77%. After DTW calculation, an overall score is given in the form of graphical signs in line 13 according to the obtained distance value d. This scoring function is based on our intervals assigned to various graphical representations shown in Figure 7-2. We experimentally consider seven intervals to feedback the quality of the practice patterns.

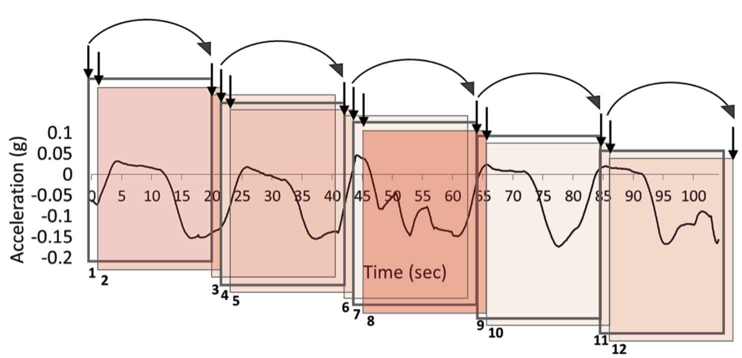

Figure 7-1: The proposed segmentation on the accelerometer-derived respiration signal of one subject

Algorithm 7-1

```
breathingTherapy (X_{1:N}, O_v, W) {

  // Inputs X_{1:N}, O_v, W
  // sensorData is updating every 20 msec!

  S = 0; pre_d = infinity; i = 0;/*Initialization*/
  while (!Stop) { /*Stop/Start condition*/
    while (!Ready(sensorData.newInstance));
    i = i + 1;
    Y_i = sensorData.newInstance;
    if (S + W = i){/*A window of new instances of data is ready*/
      d = DTW(X_{1:N}, Y_{S+1:S+W}); /*In our experiments W = N*/
      if pre_d < d {
        S = S + WO_v;
        pre_d = infinity;}
      else {S = S + (1 − O_v)×W;
        pre_d = d;}
    qualityScore(d); }}} /*A function to display the corresponding graphical
                          sign of value d*/
```

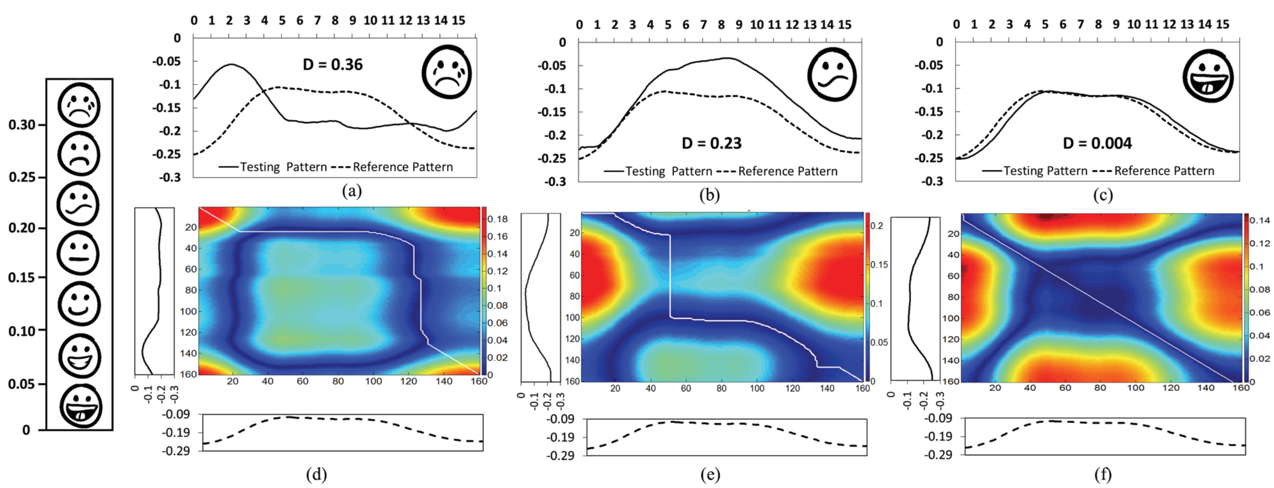

Figure 7-2: (a), (b), (c) Graphical representaions of three intermediate pranayama testing, (d)(e)(f) The distance matrix and warping path to compare the reference signal with three intermediate pranayama breahitng cycles of one subject ((the colorbar represents the absolute difference between them))

The margins of different signs can be changed based on the patient's disease and the breathing patterns prescribed by the doctor. The smaller the margins, the more sensitive visualization feedback is achieved. The feedback display is shown in Figure 7-2 on three samples. The dashed lines in the upper plots represent the reference and the solid lines show the test patterns of one subject during his intermediate pranayama breathing practices. As can be found out in Figure 7-2 (a), the test pattern has a large distance from the reference pattern, which may cause due to both timing and breathing volume mismatches. However, in Figure 7-2 (b) the matching cost of reference signal with test pattern is 0.23. It denotes that the subject was not able to breath with the analogous volume of the prescribed model. Finally, in Figure 7-2 (c) he could mimic the reference pattern almost perfectly. Figure 7-2 (d), (e) and (f) describe the obtained cost matrix as well as warping path to compare the reference and test signals.

7.3 Experimental Results

In this section, we present the experimental results on evaluating the proposed breathing therapy framework. Different yoga-based breathing exercises are chosen from recent medical researches to test the new developed biofeedback mechanism.

7.3.1 Test Setup

The investigation were carried out with 10 healthy volunteers (5 males and 5 females) aged 18 to 46 with (Mean ± SD) 30.70 ± 8.87. An accelerometer sensor was mounted on their umbilical region. We asked the subjects to perform five different yogic breathing patterns in sitting position including Buteyko and pranayama breathing exercises. The Buteyko (T_i: 2 sec, T_e: 2 sec) with 5-10% less breath volume than normal breathing, basic1 pranayama breathing pattern (T_i: 4 sec, T_e: 7 sec), basic2 pranayama breathing (T_i: 3 sec, sustain time: 6 sec and T_e: 5 sec), intermediate pranayama (T_i: 5 sec, sustain time: 4 sec and T_e: 7 sec), and advanced pranayama (T_i: 4 sec, retain time: 7 sec, T_e: 5 sec and sustain time:3 sec). In yoga, deep breathing is part of the practice of pranayama. In Sanskrit, prana is the vital energy or life force that is refers to respiration. Pranayama exercise slows down the rate of breathing and expands chest and lung capacity. In our tests, the subjects are asked to fulfill the yogic breathing requirements such as, keeping the upper body straight and erect, the head, neck and back are in alignment and the body remains motionless during the practices. To test our framework, first, the supervised reference patterns are recorded and then the test patterns are performed by each volunteer for all yogic breathing, each for one minute. The platform was able to graphically score the user's performance on a series of repetitions.

7.3.2 Results of Real-Time Biofeedback Mechanism

In this section, we provide an assessment of our proposed breathing therapy framework. The evaluations are based on five different breathing exercises. Four models are chosen from pranayama patterns and one from Buteyko control breath pattern. Previous clinical researches on pranayama as the art and science of yogic breathing techniques have indicated that pranayama might be of profit in the conditions such as, insomnia [215], heart disease [129][216], asthma [217]-[220], non-insulin dependent diabetes [221], epilepsy, obsessive compulsive disorder and depression [222]-[224]. While the pranayama breathing concentrates on reduction of breathing frequency, the core Buteyko exercises consciously reduce either breathing rate or breathing volume [224]. During our experiments, we coach our subjects to breathe the specified breathing models to record the reference patterns. Then, they are requested to practice the models based on the instruction with our proposed graphical feedback framework. Figure 7-3 (a)(d)(g)(j)(m) depict five reference patterns of one subject. For instance, the circle in Figure 7-3 (g) indicates that the subject should inhale for 3 sec, and then he should retain his breathing for 6 sec and finally exhale within 5 sec. Therefore, this breathing pattern results in respiration rate equal to 4.29 rpm. Since our technique decides based on each subject's reference pattern individually rather than a fixed breath model, the potential influences of age, gender and body size are already implicated in the results. The results of DTW technique for the first ten windows of each individual with all patterns are shown in Figure 7-3 (b)(e)(h)(k)(n). It is observed that, most subjects have high distance from the reference pattern at the first minutes of the tests; however, they gradually refine their breathing patterns in terms of the respiration rate and volume. Furthermore, considering Figure 7-3 (b) and (n), one can conclude that in easy breathing exercises the distances between reference and test patterns are less than 0.05 in most cases while for advanced practices there exist lots of peaks indicating the high distances between the reference and test patterns. It means that, in most cases the subjects achieved worse results when the breathing patterns tend to become complex. This feature is signified by the plots in Figure 7-3 (c)(f)(i)(l)(o).

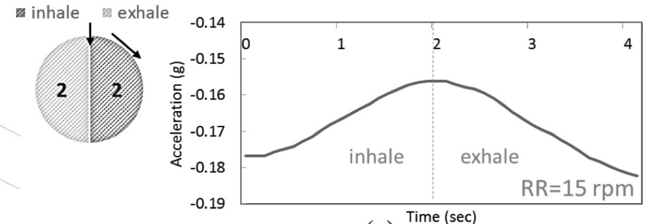
inhale
exhale
2
2
Acceleration (g)
Time (sec)
inhale
exhale
RR=15 rpm

(a)

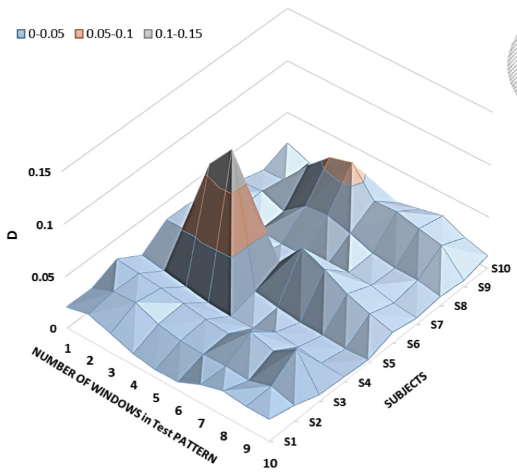
0-0.05
0.05-0.1
0.1-0.15
D
NUMBER OF WINDOWS in Test PATTERN
SUBJECTS

(b)

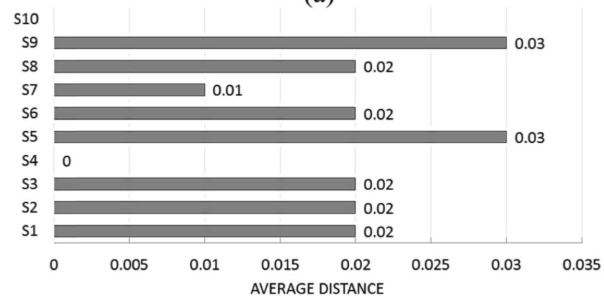
S10
S9 0.03
S8 0.02
S7 0.01
S6 0.02
S5 0.03
S4 0
S3 0.02
S2 0.02
S1 0.02
AVERAGE DISTANCE

(c)

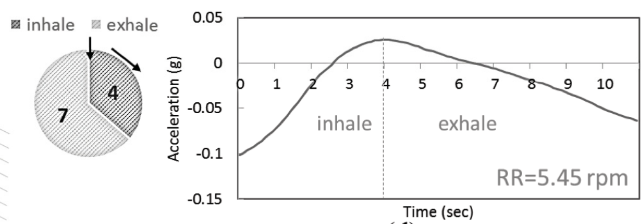
inhale
exhale
4
7
Acceleration (g)
Time (sec)
inhale
exhale
RR=5.45 rpm

(d)

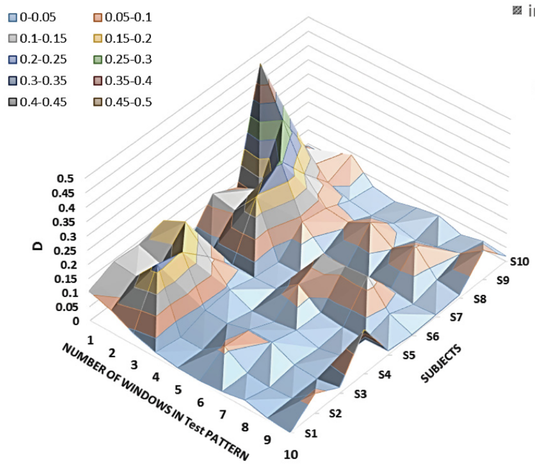
0-0.05
0.05-0.1
0.1-0.15
0.15-0.2
0.2-0.25
0.25-0.3
0.3-0.35
0.35-0.4
0.4-0.45
0.45-0.5
D
NUMBER OF WINDOWS IN Test PATTERN
SUBJECTS

(e)

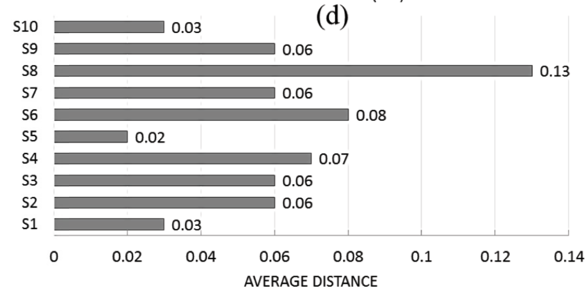
S10 0.03
S9 0.06
S8 0.13
S7 0.06
S6 0.08
S5 0.02
S4 0.07
S3 0.06
S2 0.06
S1 0.03
AVERAGE DISTANCE

(f)

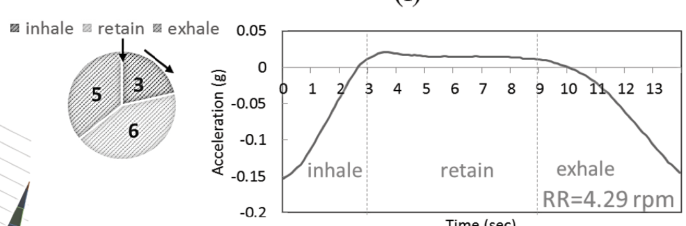
inhale
retain
exhale
5
3
6
Acceleration (g)
Time (sec)
inhale
retain
exhale
RR=4.29 rpm

(g)

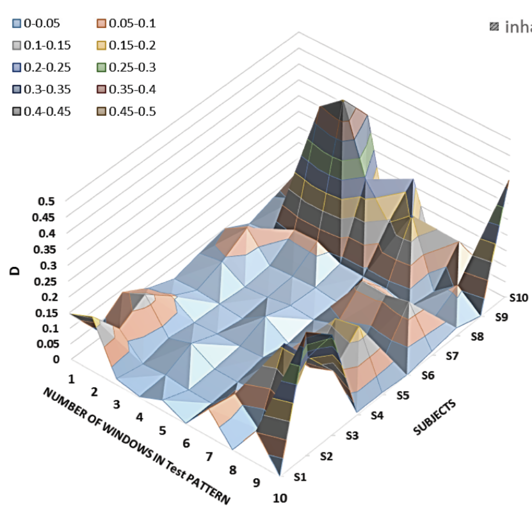
0-0.05
0.05-0.1
0.1-0.15
0.15-0.2
0.2-0.25
0.25-0.3
0.3-0.35
0.35-0.4
0.4-0.45
0.45-0.5
D
NUMBER OF WINDOWS IN Test PATTERN
SUBJECTS

(h)

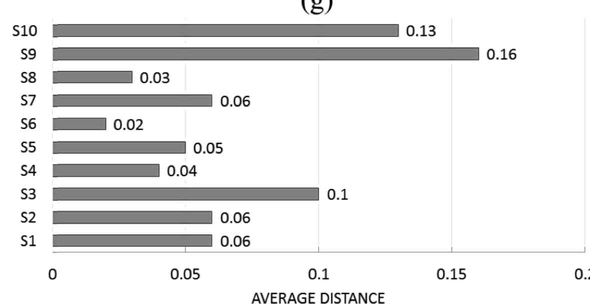
S10 0.13
S9 0.16
S8 0.03
S7 0.06
S6 0.02
S5 0.05
S4 0.04
S3 0.1
S2 0.06
S1 0.06
AVERAGE DISTANCE

(i)

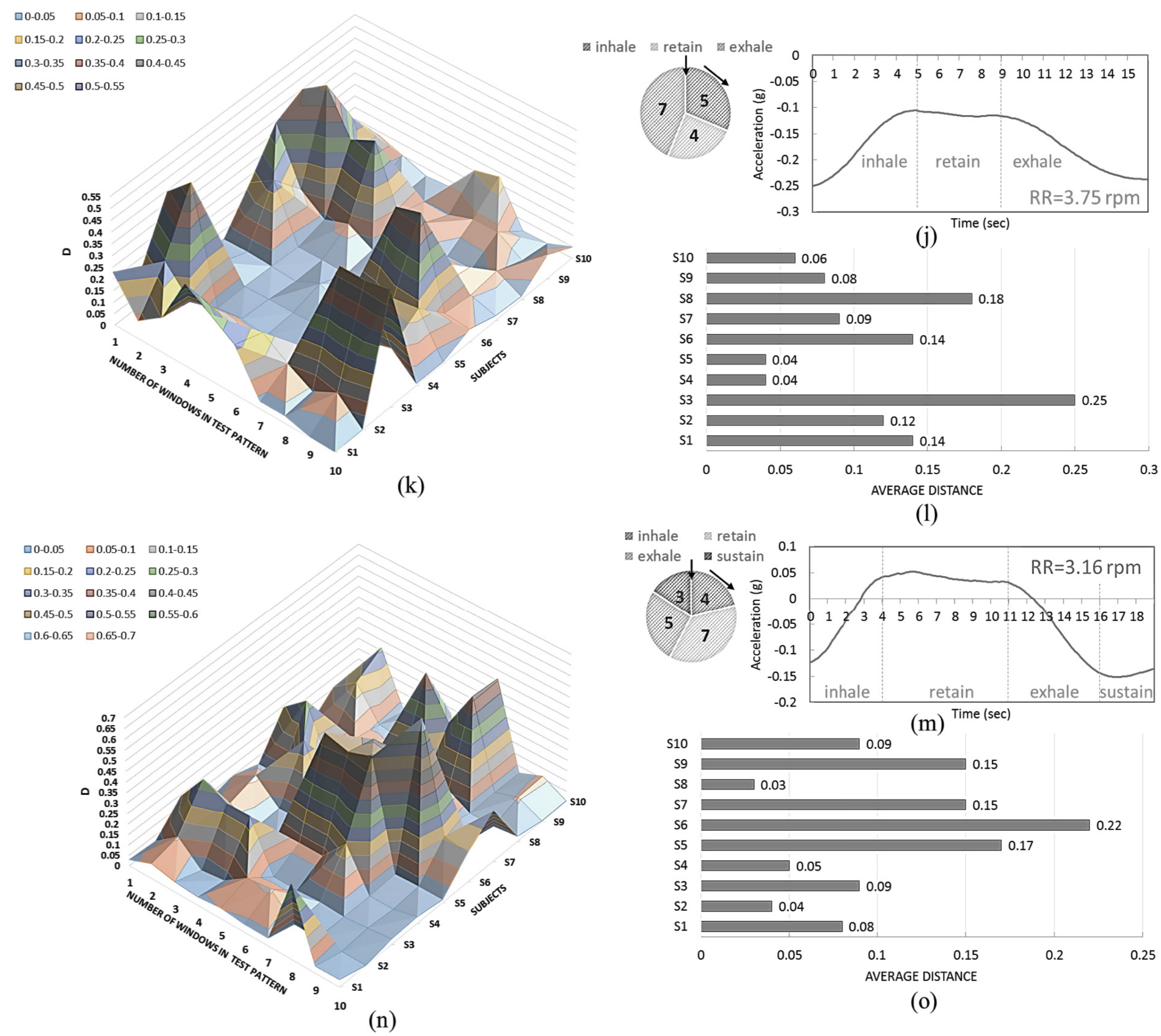

Figure 7-3: (a), (d), (g), (j), (m) Buteyko reduced breathing, basic1, basic2, intermediate and advanced reference patterns of one subject obtained from an accelerometer sensor, respectively, (b), (e), (h), (k), (n) The distance values of each segment of Buteyko reduced breathing, basic1, basic2, intermediate and advanced test patterns of 10 subject correspondingly, (c), (f), (i), (l), (o) The average distance on all testing patterns of each subject

These plots show the average distance of each subjects from the reference patterns for all breath maneuvers. For example, considering Figure 7-3 (f), Subject#8 has the maximum average distance during his ten sequential iterations while performing the basic1 pranayama pattern. This is also signified in Figure 7-3 (e). In the first three iterations, Subject#8 has large mismatches between his reference and test patterns; however, he could improve his poor breathing in the final iterations.

The average distance values on all subjects derived from Figure 7-3 (c)(f)(i)(l)(o) are: 0.02, 0.06, 0.07, 0.11 and 0.11. Therefore, these results show that, moving from easy to difficult breathing maneuvers, there are cases where the volunteers are not able to properly perform the considered patterns and need to keep practicing to modify their respiratory function. This is more likely to happen for poor breathers who get stuck and struggle to return to their normal breathing. It is worth mentioning that, during the experimental sessions, subjects were curious to know their average quality to be able to compare it with others. Therefore, it elaborates on this interesting point that our proposed breathing therapy platform motivates people's mentality of competition.

7.4 Summary

In this chapter, a breathing therapy framework have been proposed based on DTW with a fast and simple segmentation technique. With this biofeedback mechanism people are able to check their breathing quality during practicing the prescribed breathing exercises, quantitatively. For this

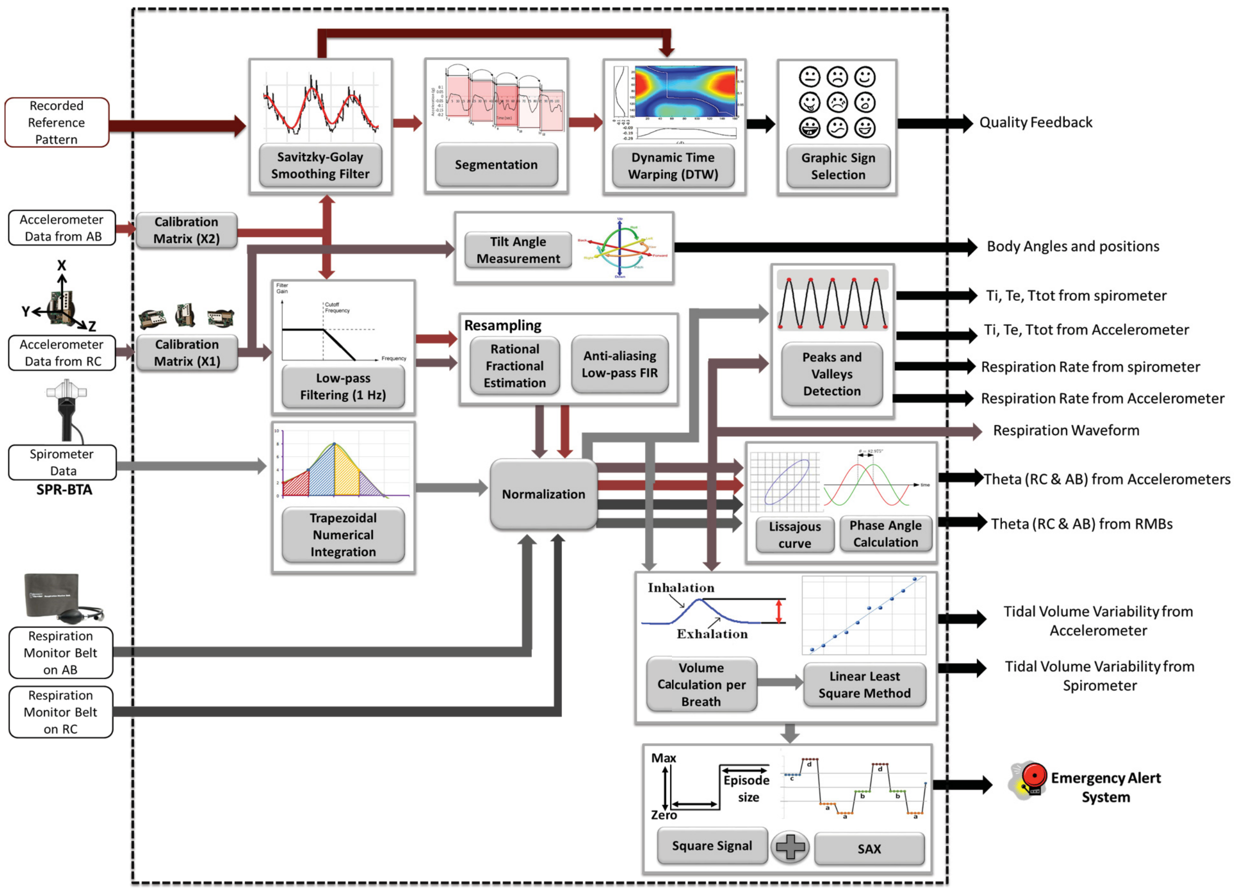

Figure 7-4: The overall view of the proposed system

purpose, different breathing maneuvers were modeled from different medical references. Generally, these exercises are recommended at a frequency of a couple of time per day or week. The proposed algorithm helps patients to follow exact instructions since otherwise it may cause lung problems such as over-expansion. The breathing retraining through such a quality feedback system might be helpful because it can induce relaxation, provide motivations to practice the prescribed exercises when the symptoms occur and promote a sense of mastery, as well. The overall view of the proposed respiration monitoring system is summarized in Figure 7-4.

Chapter 8

CONCLUSIONS AND FUTURE WORK

This chapter summarizes the work that was presented in this thesis, along with some suggested future work.

8.1 Conclusions

In this thesis, we present a remote monitoring system with the capability of different parameters estimations of respiration signal, accurately. Indeed, the proposed system is an integration of cutting-edge technology such as wearable sensors, BLE and backend cloud with prominent benefits of cost, convenience, and quality of service. Therefore, in the first phase, the hardware modules are chosen in a way that addresses issues such as power consumption, safety and privacy, user's comfort, easy setup and affordability. Then the novel algorithms are proposed to thoroughly fulfil the design requirements such as accuracy, fault tolerant, multifunctional, with low complexity.

- We introduced a MMSE self-recalibration algorithm to obtain the best reference model to compensate the systematic bias occurs during decalibration. For this purpose, first the fault-screening algorithm was presented with constant threshold to detect the decalibrated sensors and exclude them from the fusion. Then, the best coefficients were obtained in terms of MMSE to jointly calibrate the faulty sensors. In addition, we make use of linear MMSE to calculate the best threshold value to design the fault-tolerant sensor fusion using convex optimization. Therefore, the screening algorithm can exclude multiple decalibrated sensors in real-time from the fusion. We have also evaluated the precision efficiency of the proposed fault-tolerant algorithm compared to the previous related work.

- A signal processing procedure were proposed to obtain the respiration signal, respiration rate, respiratory time parameters such as inspiration time, expiration time and total time of a breath cycle, as well as the body angles during rest positions with a single accelerometer sensor mounted on the subjects' chest. The use of a tri-axial device allows inclination changes to be measured regardless of the orientation. Additionally, an accelerometer-based approach was developed to accurately estimate the phase shift between chest wall compartments for paradoxical breathing diagnosis. The results were evaluated based on medical references including spirometer and Respiration Monitor Belt.
- A new technique was proposed to estimate the tidal volume variability based on the chest compartments movements obtained from acceleration signal during inhalation and exhalation. As a method of improving patient care systems, hospitals often utilize patient monitoring and alerting systems in which the patient data stream is rapidly analyzed to recognise the emergency situations. Therefore, a new real-time alarm detection technique was proposed to obtain the threshould values dynamically considering each individual's respiration characteristics. This technique is applicabale in an emergency alarm system to trigger an alert based on monitoring the tidal volume variability if the condition of the patients are not suitable to make a call.
- Remote diagnosis as an act of determining a person's illnesses by observation from a distance is an integral and very large part of biomedical education. Therefore, in this dissertation we have developed decision-making algorithms to distinguish among different pathological breathing patterns with high accuracy. For this purpose, two sensor-equipped belts were worn around the subjects' chest and abdomen to record the motions during simulating different breathing patterns derived from definitions in medical researches. First, a hierarchical support vector machine which uses famous time domain features was proposed to differentiate among six different breathing patterns. A feature selection was introduced to reduce the features dimensionality in each level of our proposed tree-structured model. The solution was obtained in $O(p^2)$ time, where we have totally p number of features. Further improvements were achieved by considering our proposed

feature extraction technique based on estimated breathing parameters with our sensory system. An extensive evaluation on 6 well-known classifiers was performed with new time domain features while the number of pathological breathing patterns were also increased into nine. Concluding this, the effects of different window sizes, overlap values, sensor placement, feature selection, and sampling frequencies were assessed with regard to classification accuracy. Furthermore, a new tree-structured model was presented on a 2-D performance measure associated with our multi-class problem. Sensitivity and accuracy measures express two key parameters associated with a recognition system. Different assessments showed that, optimizing these two measures results in obtaining models that combine a high classification level in the dataset with a good classification rate for each class.

- Behind our simple breathing, there exists a process that affects our thoughts and feelings, creativity, and the way we function in our daily life. The therapeutic breathing exercises as well as yoga-based breathing maneuvers were widely used as a means of self-regulation and restoration of physical, mental and emotional balance. In this thesis, we showed the applicability of DTW to invent a biofeedback system based on wearable and wireless technology in "breathing therapy". The reference respiration exercise was recorded under the expert's supervision, and then the users can practice these patterns on their own at home. A new segmentation technique was proposed in DTW for comparing the reference breathing pattern with the test patterns in real-time. The experimental results showed that, such a system can motivates people's mentality of competition to reach to a high degree of treatment.

These contributions has been extensively analyzed and evaluated based on medical references on database of real subjects.

8.2 Future Work

Given the novelty of this work, there is still much room to investigate new methods and approaches. In this section, possible future directions to continue and extend the work presented in this thesis are described.

- One of the major limitations of the accelerometer-derived respiration signal refers to the lack of available datasets to benchmark new models and compare them with prior work. Consequently, a strong effort must be put by the wearable scientific community to collect new datasets that may serve to validate accelerometer-based respiration signals. Future studies to test the validity of these techniques should be performed in a clinical setting on individuals with actual rather than simulated breathing pattern disturbances.
- A user might misplace a sensor during the self-placement process as a consequence of a mistake, therefore, the effect of sensor displacement in diagnosis system is also found very interesting area.
- Applying different types of medical sensors e.g. Oximeters and motion sensors such as gyroscopes and magnetometers to extend the proposed sensor fusion technique is another interesting potential future work specially to extract other vital signs such as heart rate.
- It would also be a promising future work avenue to mainly investigate on the brain wave characteristics (electroencephalogram, EEG) during different breathing patterns to be used as features in breathing disorders classification. In addition, investigating EEG signals during breathing meditation can provide feedback from the minds to enhance the performance of the proposed biofeedback mechanism.

BIBLIOGRAPHY

[1] N. A. Abidoye, N. Azeez, A. Adesina, K. Agbele, and H. Nyongesa, “Using wearable sensors for remote healthcare monitoring system,” J. Sens. Technol., vol. 1, no. 2, pp.22–28, 2011.

[2] F. Koushanfar, S. Slijepcevic, M. Potkonjak, A. Sangiovanni-Vincentelli, “Error-Tolerant Multi-Modal Sensor Fusion”, IEEE CAS Workshop on Wireless Communication and Networking, 2002.

[3] “Challenges in Neonatal Nursing: Providing Evidence-Based Skin Care”, Medscape, 2003.

[4] Ted Rosen, “Allergic Reaction to Conducting Gel Used Under ECG Electrodes”, Rheumatology network, May 2012.

[5] “Technologies for Remote Patient Monitoring in Older Adults”, Center for Technology and Aging, An Initiative of The SCAN Foundation and Public Health Institute, December 2009.

[6] J. Vestbo, S.S. Hurd, A.G. Agusti, P.W. Jones, C. Vogelmeier, A. Anzueto, P.J. Barnes, L.M. Fabbri, F.J. Martinez, M. Nishimura, *et al*. ”Global strategy for the diagnosis, management and prevention of chronic obstructive pulmonary disease,” GOLD executive summary. Am J Respir Crit Care Med, vol.187, pp.347–365, 2013.

[7] National Pressure Ulcer Advisory Panel (NPUAP), “Pressure Ulcer Prevention Points”, Washington, DC, 2014.

[8] Centers of Disease Control and Prevention (CDC), “Sudden Unexpected Infant Death and Sudden Infant Death Syndrome”, September 29, 2014.

[9] R. Gilbert, G. Salanti, M. Harden, and S. See, “Infant sleeping position and the sudden infant death syndrome: systematic review of observational studies and historical review of recommendations from 1940 to 2002,”Int. J. Epidemiol. 34(4):874-87, 2005.

[10] Silva *et al.* “monitoring respiratory device” International application published under the patent cooperation treaty (PCT), WO 2004/043263 A2, 2004.

[11] NHLBI: Health Information for the Public. U.S. Department of Health and Human Services. "Sleep Apnea: What Is Sleep Apnea?" May 2009. Retrieved 2010-08-05.

[12] “Types of Sleep Apnea”, Apnea Treatment Center, Available: http://www.apneatreatmentcenter.com/.

[13] D.A. Hofsøy, J.F. Clauss, B. Wolf, "Monitoring and therapy of sleep-related breathing disorders," Wearable Micro and Nano Technologies for Personalized Health (pHealth), 2009 6th International Workshop on, pp.41-44, June 2009.

[14] Office of Communications and Public Liaison, National Institute of Neurological Disorders and Stroke, National Institutes of Health, Bethesda, MD, “Brain Basics: Understanding Sleep”, NIH Publication No.06-3440-c, July 2014.

[15] B. Staats, H. Bonekat, C.D. Harris, K. Offord, “Chest wall motion in sleep apnea,” Am Rev Respir Dis, 130(1):59-63,1984.

[16] American Sleep Apnea Association, “OSA Treatment Options”, 2014.

[17] Z. Cao, R. Zhu, R. Que, “A wireless portable system with micro sensors for monitoring respiratory diseases,” IEEE Trans Biomed Eng; 59(11):3110–6, 2012.

[18] M. Al-Mardini, F. Aloul, A. Sagahyroon, L. Al-Husseini, “Classifying obstructive sleep apnea using smartphones,” Journal of Biomedical Informatics, 52:251-9, July 2014.

[19] “Stedman's Medical Dictionary” (28th ed.). Philadelphia: Lippincott Williams & Wilkins. pp.250.

[20] H. William, L. Myron, D. Robin, A. Mark, “Current Diagnosis and Treatment in Pediatrics,” 21 Ed., McGraw-Hill Professional: New York City, USA, p. 989.

[21] T. Brack, I. Thüer, C.F. Clarenbach, *et al.* "Daytime Cheyne–Stokes respiration in ambulatory patients with severe congestive heart failure is associated with increased mortality," Chest journal, 132(5):1463-71, 2007.

[22] K. Parveen, C. Michael, “Clinical Medicin”, 6th Ed; Elsevier: Philadelphia, USA, p. 733.

[23] P. Kaufmann, K.H. Smolle, S. Fleck and A. Lueger, “Ketoacidotic diabetic metabolic dysregulation: pathophysiology, clinical aspects, diagnosis and therapy Wien. Klin. Wochenschr., 106(5):119-27, 1994.

[24] R.J. Farney, J.M. Walker, K.M. Boyle, T.V. Cloward, K.C. Shilling, “Adaptive servoventilation (ASV) in patients with sleep disordered breathing associated with chronic opioid medications for non-malignant pain,” J. Clin. Sleep Med., 4:311–319, 2008.

[25] Blausen.com staff. "Blausen gallery 2014". Wikiversity Journal of Medicine.

[26] Respiratory center. (n.d.) The American Heritage® Medical Dictionary. (2007). retrieved October 17 2014.

[27] G. Aljadeff, M. Molho, I. Katz, S. Benzaray, Z. Yemini, & R.J. Shiner, “ Pattern of lung volumes in patients with sighing breathing,” Thorax, 48(8):809-11, 1993.

[28] “SensorTag”, Available: www.ti.com/sensortag-wiki

[29] “OLP425”, Available: http://www.connectblue.com

[30] Technical Information, “The Low Energy Technology Behind Bluetooth Smart” Bluetooth SIG, Inc., 2014.

[31] “DropBox”, Available: https://dropbox.com

[32] “Parse”, Available: https://parse.com

[33] “IBM Bluemix”, Available: https://console.ng.bluemix.net

[34] M. Shoaib, S. Bosch, O. Incel, H. Scholten, and P. Havinga, “A Survey of Online Activity Recognition Using Mobile Phones,” Sensors, vol.15, no. 1, pp.2059–2085, Jan. 2015.

[35] A. Roshan Fekr, M. Janidarmian, O. Sarbishei, B. Nahill, K. Radecka, Z. Zilic, “MSE minimization and fault-tolerant data fusion for multi-sensor systems,” In the IEEE 30th International Conference on Computer Design, pp.445–452, Canada, 2012, © 2012 IEEE.

[36] O. Sarbishei, A. Roshan Fekr, M. Janidarmian, B. Nahill, K. Radecka, "A minimum MSE sensor fusion algorithm with tolerance to multiple faults", 18th IEEE European Test Symposium (ETS), pp. 1, 2013, © 2013 IEEE.

[37] O, Sarbishei, B. Nahill, A. Roshan Fekr, M. Janidarmian, K. Radecka, Z. Zilic, B. Karajica, "An efficient fault-tolerant sensor fusion algorithm for accelerometers," Body Sensor Networks (BSN), pp.1-6, May 2013, © 2013 IEEE.

[38] O. Sarbishei, M. Janidarmian, A. Roshan Fekr, B. Nahill, K. Radecka, Z. Zilic, "Multi-sensory System Integration Dependability", Chapter 18 in Book Technologies for Smart Sensors and Sensor Fusion, edited by K. Yallup and K. Iniewski, pp.319-335, 2013.

[39] A. Roshan Fekr, M. Janidarmian, K. Radecka, "Remote Blind Calibration of Multi-Sensory Systems in Medical Applications", 4th IEEE International Conference on Wireless Health, 1-3 November, Baltimore, USA, 2013, © 2013 IEEE.

[40] A. Roshan Fekr, M. Janidarmian, K. Radecka, Z. Zilic, "Multi-Sensor Blind Recalibration in mHealth Applications", IEEE International Humanitarian Technology Conference (IHTC), pp.1-4, Canada, 2014, © 2014 IEEE.

[41] A. Roshan Fekr, M. Janidarmian, K. Radecka, Z. Zilic, "A medical cloud-based platform for respiration rate measurement and hierarchical classification of breath disorders," Sensors 2014, 14, 11204-11224.

[42] A. Roshan Fekr, M. Janidarmian, K. Radecka, Z. Zilic, "Design of an e-Health Respiration and Body Posture Monitoring System and Its Application for Rib Cage and Abdomen Synchrony Analysis", 2014 IEEE International Conference on Bioinformatics and Bioengineering (BIBE), pp.141-148, Florida, 2014, © 2014 IEEE.

[43] A. Roshan Fekr, K. Radecka, Z. Zilic, "Tidal volume variability and respiration rate estimation using a wearable accelerometer sensor," 4th IEEE Conference on Wireless Mobile Communication and Healthcare (Mobihealth), pp.1-6, Rome, 2014, © 2014 IEEE.

[44] A. Roshan Fekr, K. Radecka, Z. Zilic, "Design and Evaluation of an Intelligent Remote Tidal Volume Variability Monitoring System in e-Health Applications," IEEE Journal of Biomedical and Health Informatics, no.99, pp.1, 2015, © 2015 IEEE.

[45] A. Roshan Fekr, K. Radecka, Z. Zilic, "Development of a Remote Monitoring System for Respiratory Analysis", Lecture Notes of the Institute for Computer Sciences, Social Informatics and Telecommunications Engineering Volume 150, pp.193-202, 2015.

[46] A. Roshan Fekr, Majid Janidarmian, K. Radecka, Z. Zilic, "Respiration Disorders Classification with Informative Features for m-health Applications", IEEE Journal of Biomedical and Health Informatics, vol.PP, no.99, pp., 2015, © 2015 IEEE.

[47] A. Roshan Fekr, Majid Janidarmian, K. Radecka, Z. Zilic, "Sensitivity Versus Accuracy in a Hierarchical Breathing Disorders Classification Using Evolutionary Algorithm," Journal of Biomedical Informatics, 2015 (submitted).

[48] A. Roshan Fekr, M. Janidarmian, K. Radecka, Z. Zilic, "Movement analysis of the chest compartments and a real-time quality feedback during breathing therapy" journal of Network Modeling Analysis in Health Informatics and Bioinformatics, Springer, 2015.

[49] J. Feng, G. Qu, M. Potkonjak, "Sensor calibration using non parametric statistical characterization of error models," Sensors, 2004. Proceedings of IEEE, vol.3, pp.1456-1459, Oct. 2004

[50] T. Beravs, J. Podobnik, M. Munih, "Three-axial accelerometer calibration using Kalman filter covariance matrix for online estimation of optimal sensor orientation," IEEE Trans. On Instrumentation and Measurements, vol. 61, no. 9, pp.2501–2511, 2012.

[51] V. Bychkovskiy, S. Megerian, D. Estrin, and M. Potkonjak "A Collaborative Approach to In-Place Sensor Calibration," 2nd International Workshop on Information Processing in Sensor Networks, pp.301-316, 2003.

[52] M.A.P. Pertijs, A.L. Aita, K.A.A. Makinwa, J.H. Huijsing, "Low-cost calibration techniques for smart temperature sensors," *Sensors Journal, IEEE*, vol.10, no.6, pp.1098-1105, June 2010.

[53] M.A.P. Pertijs, K. A. A. Makinwa, and J. H. Huijsing, "ACMOS smart temperature sensor with a 3σ inaccuracy of ±0.1 ˚C from -55°C to 125°C," IEEE J. Solid-State Circuits, vol.40, pp.2805–2815, Dec. 2005.

[54] Y. Xianjun, L. Cuimei, "Development of high-precision temperature measurement system based on ARM," Electronic Measurement & Instruments, 9th International Conference on, pp.1- 795-1-799, Aug. 2009.

[55] N. Mehranbod, M. Soroush, "Probabilistic model for sensor fault detection and identification," AIChE Journal, vo.49, no.7, pp.1787-1802, July 2003.

[56] H. B. Aradhye, "Sensor fault detection, isolation, and accommodation using neural networks, fuzzy logic, and Bayesian belief networks," M.S. Diss, University of New Mexico, Albuquerque, NM, 1997.

[57] C. Rojas-Guzman, M.A. Kramer, "Comparison of belief networks and rule-based expert systems for fault-diagnosis of chemical", Eng. Applic. Artif. Intell., vol.6, pp.191-202, 1993.

[58] Z. Zilic and K. Radecka, "Fault tolerant glucose sensor readout and recalibration," Proceedings of the 2nd conference on Wireless Health, pp.1-2, 2011.

[59] M.A. Kareem, J. Langari, and R. Langari, "A hybrid real-time system for fault detection and sensor fusion based on conventional fuzzy clustering approach," IEEE International Conference on Fuzzy Systems, FUZZ, Reno, NV, pp.189-194, May 2005.

[60] J. Bezdek, R. Hathaway, M. Sabin, and W. Tucker, "Convergence theory for fuzzy c-means: counterexamples and repairs", IEEE Trans. On Systems, Man and Cybernetics, Volume SMC-17, pp.873-877, 1987.

[61] L. Xiao, S. Boyd, S. Lall, "A scheme for robust distributed sensor fusion based on average consensus," International Conference on Information Processing in Sensor Networks, pp.63-70, Los Angeles, 2005.

[62] F. Chunling, J. Zhihua, J. Zhang; W. Tian, "Application of multi-sensor data fusion based on RBF neural networks for fault diagnosis of SAMS," International Conference on Control, Automation, Robotics and Vision, pp.1557- 1562, Dec. 2002.

[63] G. A. L. Araujo, R. C. S. Freire, J. F. Silva, A. Oliveira, and E. F. Jaguaribe, "Breathing flow measurement with constant temperature hot-wire anemometer for forced oscillations technique," in Proc. 21st IEEE Instrum. Meas. Technol. Conf., pp.730–733, May 2004.

[64] Y. W. Bai, W. T. Li, and Y. W. Chen, "Design and implementation of an embedded monitor system for detection of a patient's breath by double webcams," in Proc. 2010 IEEE Int.Workshop Med. Meas. Appl., p. 93 - 98, 2010.

[65] S. Fouzas, K.N. Priftis, M.B. Anthracopoulos, "Pulse oximetry in pediatric practice, Pediatrics" 128(4):740-752, 2011.

[66] J. R. Feiner, J.W. Severinghaus, P.E. Bickler, "Dark Skin Decreases the Accuracy of Pulse Oximeters at Low Oxygen Saturation: The Effects of Oximeter Probe Type and Gender", Anesthesia and Analgesia; 105(6 Suppl):S18-23, December 2007.

[67] R.D. Branson, D.R. Hess, R.L. Chatburn, "Respiratory care equipment" Philadelphia, PA: Lippincott Williams & Wilkins; 1999.

[68] C. L. Que, C. Kolmaga, L. G. Durand, S. M. Kelly, and P. T. Macklem, "Phonospirometry for noninvasive measurement of ventilation: methodology and preliminary results." J Appl Physiol, vol. 93, no. 4, pp.1515– 1526, Oct 2002.

[69] R. Ciobotariu, F. Adochiei, C. Rotariu, H. Costin, "Wireless Breathing System for Long Term Telemonitoring of Respiratory Activity", Advanced Topics in Electrical Engineering, Proc. of the 7th International Symposium, pp.635-638, May 2011.

[70] O. Kaltiokallio, H. Yigitler, R. J¨antti, and N. Patwari, "Non-invasive respiration rate monitoring using a single COTS TX-RX pair," Proceedings of the 13th International Symposium on Information Processing in Sensor Networks, pp.59-70, 2014.

[71] K. Nepal, E. Biegeleisen, T. Ning, "Apnea detection and respiration rate estimation through parametric modeling," Proceedings of the 28th *IEEE Annual Northeast Bioengineering Conference*, pp.277-278, 2002.

[72] K.S Tan, R. Saatchi, H. Elphick, D. Burke, "Real-time vision based respiration monitoring system," *Communication Systems Networks and Digital Signal Processing* (CSNDSP), 7th International Symposium on , pp.770,-774, July 2010.

[73] D.R. Lowne, M. Tarler, "Designing a low-cost mattress sensor for automated body position classification". *Conf. Proc. IEEE Eng. Med. Biol. Soc*., 6:6437-40, 2005.

[74] H. L. Watson, M.A. Sackner, F. D. Stott, "Method and apparatus for monitoring respiration" US Patent US4815473, Jan. 5 1982.

[75] R. Bailon, L. Sörnmo, and P. Laguna. "ECG-derived respiratory frequency estimation," Advanced Methods and Tools for ECG Data Analysis, Artech House Inc, pp.215-244, 2006.

[76] J. Lazaro, A. Alcaine, D. Romero, E. Gil, P. Laguna, E. Pueyo, and R. Bailón, "Electrocardiogram Derived Respiratory Rate from QRS Slopes and R-wave Angle," Annals Biomedical Engineering, pp.2072-2083, October 2014.

[77] J. Lázaro, A. Alcaine, D. Romero, E. Gil, P. Laguna, L. Sörnmo, and R. Bailón. "Electrocardiogram derived respiration from QRS slopes: evaluation over stress testing recordings," In: Computing in Cardiology, pp.655-658, 2013.

[78] J. Webster, Medical Instrumentation: Application and Design, 4th ed. New York, NY, USA: Wiley, pp. 196-198, 2009.

[79] T. Reinvuo, M. Hannula, H. Sorvoja, E. Alasaarela, R. Myllyla, "Measurement of respiratory rate with high-resolution accelerometer and emfit pressure sensor," *In Proceedings of the IEEE Sensors Applications Symposium*, pp.192-195, 2006.

[80] P.K. Dehkordi, M. Marzencki, K. Tavakolian, M. Kaminska, B. Kaminska, "Validation of respiratory signal derived from suprasternal notch acceleration for sleep apnea detection," *Engineering in Medicine and Biology Society, EMBC, International Conference of the IEEE*, pp. 3824-3827, 2011.

[81] D.S. Morillo, J.L.R. Ojeda, L.F.C. Foix, A.L. Jimenez, "An Accelerometer-Based Device for Sleep Apnea Screening," *IEEE Trans. Inf. Technol. Biomed*. vol.14, pp.491-499, 2010.

[82] M. Jafari Tadi, T. Koivisto, M. Pänkäälä, and A. Paasio, "Accelerometer-Based Method for Extracting Respiratory and Cardiac Gating Information for Dual Gating during Nuclear Medicine Imaging," International Journal of Biomedical Imaging, pp. 1-11, 2014.

[83] A. Bates, M.J. Ling, J. Mann, D. K. Arvind, "Respiratory Rate and Flow Waveform Estimation from Tri-axial Accelerometer Data," Body Sensor Networks (BSN), 2010 International Conference on, pp.144-150, June 2010.

[84] Ja-Woong Yoon, Yeon-Sik Noh, Yi-Suk Kwon, Won-Ki Kim, Yoon Hyung-Ro, " Improvement of Dynamic Respiration Monitoring Through Sensor Fusion of Accelerometer and Gyro-sensor," Journal of electrical engineering & technology vol.9, no.1; pp.334-343, 2014.

[85] L. Fernandes do Prado, X. Li, R. Thompson , C. Marcus, "Body position and obstructive sleep apnea in children," Sleep, 25(1):66-71, 2002.

[86] Floyd R. Livingston Jr., "Sudden Infant Death Syndrome (SIDS)", KidsHealth, April 2014.

[87] R. Jokic, "Positional therapy versus continuous positive airway pressure in patients with positional obstructive sleep apnea," Chest, pp.771-781, 1999.

[88] R. Cartwright, "A comparative study of treatment for positional sleep apnea," Sleep vol.14, pp.456-552, 1991.

[89] R. C. Heinzer, C. Pellaton, V. Rey et al. "Positional therapy for obstructive sleep apnea: an objective measurement of patients' usage and efficacy at home," Sleep Med., 13: 425-428, 2012.

[90] J. B. Lee, Y. H. Park, J. H. Hong, S. H. Lee, "Determining optimal sleep position in patients with positional sleep-disordered breathing using response surface analysis", Sleep Res , vol.18, pp.26-35, 2009.

[91] R. M. Khoury, L. Camacho-Lobato, P. O. Katz, M. A. Mohiuddin, and D. O. Castell, “Influence of spontaneous sleep positions on nighttime recumbent reflux in patients with gastroesophageal reflux disease,” Am J Gastroenterol, vol.94, pp.69-73, 1999.

[92] M. Sackner, H. Gonzalez, M. Rodriguez, A. Belsito, D. Sackner, S. Grenvik, “Assessment of asynchronous and paradoxical motion between rib cage and abdomen in normal subjects and in patients with chronic obstructive pulmonary disease,” Am Rev Respir Dis., pp.88-93, 1984.

[93] M. Tobin, T. Chadha, G. Jenouri, S. Birch, H. Gazeroglu, M. Sackner, “Breathing patterns. 1. Normal subjects,” Chest, 84(2):202-5, 1983.

[94] A. Aliverti, M. Quaranta, B. Chakrabarti, A.L. Albuquerque, P.M. Calverley “Paradoxical movement of the lower ribcage at rest and during exercise in COPD patients,” Eur Respir, pp.49-60, 2009.

[95] J. Sharp, N. Goldberg, W. Druz, H. Fishman, J. Danon, “Thoracoabdominal motion in chronic obstructive pulmonary disease,” Am Rev Respir Dis, pp.47–56, 1977.

[96] V. Parreira , D. Vieira, M. Myrrha, I. Pessoa, S. Lage, R. Britto, “Optoelectronic plethysmography: a review of the literature”, Braz. J. Phys. Ther, vol.16, no.6, pp.439-453, Dec 2012.

[97] D. Wolfson, K. Strohl, A. DiMarco, M. Altose, “Effects of an increase in end-expiratory volume on the pattern of thoracoabdominal movement,” Respiration Physiology 53:273-283, 1983.

[98] L. Bernardi, C. Porta, A. Gabutti, L. Spicuzza, P. Sleight, "Modulatory effects of respiration." Autonomic Neuroscience 90(1-2): 47-56., 2001.

[99] F. Yasuma and J Hayano, "Respiratory Sinuse Arrhythmia. Why does heartbeat syncronize with respiratory rhythm." Chest, pp.683-690, 2004.

[100] B. Lange, S. Flynn, A. Rizzo, M. Bolas, M. Silverman, and A. Huerta, “Breath: A Game to Motivate the Compliance of Postoperative Breathing Exercises,” in Virtual Rehabilitation International Conference, pp.94-97, 2009.

[101] J. S. Ahluwalia, C. J. Morley, H. Wahle, “Volume guarantee new approaches in volume controlled ventilation for neonates,” Lubeck, Germany: Drager Medizintechnick, 1998.

[102] W.S. Fowler "Lung Function studies. II. The respiratory dead space," Am. J. Physiol, vol.154, pp.405-416, 1948.

[103] A.K. Chang, P. Mukherji, “Pneumothorax, Iatrogenic, Spontaneous and Pneumomediastinum,” eMedicine, Dictionary of physiotherapy, 2007.

[104] D. Dreyfuss, G. Saumon, “Role of tidal volume, FRC, and end-expiratory volume in the development of pulmonary edema following mechanical ventilation,” Am Rev Respir Dis, pp.1194 -1203, 1993.

[105] L. A. Hernandez, K. J. Peevy, A. A. Muise,”Chest wall restriction limits high airway pressure-induced injury in young rabbits,” J Appl Physiol; vol.66, pp.2364-2368, 1989.

[106] P. De Chazal, C. Heneghan, E. Sheridan, R. Reilly, P. Nolan, and M. O'Malley, "Automated processing of the single lead electrocardiogram for the detection of obstructive sleep apnoea," IEEE Trans. Biomed. Eng., vol.50, no.6, pp.686-696, Jun 2003.

[107] F. Roche, V. Pichot, E. Sforza, I. Court-Fortune, D. Duverney, F. Costes, M. Garet, and J.-C. Barth´el´emy, "Predicting sleep apnoea syndrome from heart period: A time–frequency wavelet analysis," Eur. Respir. J., vol.22, pp.937-942, 2003.

[108] N. F. Garcia, P. Gomis, A. La Cruz, G. Passeriello, and F. Mora, "Bayesian hierarchical model with wavelet transform coefficients of the ECG in obstructive sleep apnea screening," Comput. Cardiol. vol.27, pp.275-278, 2000.

[109] A. H. Khandoker, M. Palaniswami, C. K. Karmakar, "Support vector machines for automated recognition of obstructive sleep apnea syndrome from ECG recordings," IEEE Trans Inf Tech Biomedicine, vol.13, pp.37-48, 2009.

[110] R. Lin, R. Lee, C. Tseng, H. Zhou, C. Chao, J. Jiang, "A New Approach for Identifying Sleep Apnea Syndrome Using Wavelet Transform and Neural Networks," Biomed. Eng. Appl. Basis Commun. 2006, 18:138–143.

[111] B. Koley and D. Dey, "Adaptive classification system for real-time detection of apnea and hypopnea events," in Proc. IEEE Point-of-Care Healthcare Technol., pp. 42-45, 2013.

[112] S. Jafari, H. Arabalibeik, K. Agin, "Classification of normal and abnormal respiration patterns using flow volume curve and neural network," Health Informatics and Bioinformatics (HIBIT), International Symposium on, pp.110-113, April 2010.

[113] V. Mahesh, S. Ramakrishnan, "Assessment and classification of normal and restrictive respiratory conditions through pulmonary function test and neural network," J. Med. Eng. Techno., vol.31, pp.300-304, 2007.

[114] V. Mahesh, S. Ramakrishnan, "Detection of obstructive respiratory abnormality using flow-volume," J. Med. Syst., vol. 31 (6), pp. 461-465, 2007.

[115] M. J. Baemani, A. Monadjemi, and P. Moallem, "Detection of respiratory abnormalities using artificial neural networks," Journal of Computer Science, vol. 4(8), pp. 663-667, 2008.

[116] R. Palaniappan, K. Sundaraj, "Respiratory sound classification using cepstral features and support vector machine" in Proc. IEEE Recent Advances in Intelligent Computational Systems (RAICS), pp. 132–136, December 2013.

[117] M. Yamashita, M. Himeshima, S. Matsunaga, "Robust classification between normal and abnormal lung sounds using adventitious-sound and heart-sound models," Acoustics, Speech and Signal Processing (ICASSP), IEEE International Conference on, pp.4418-4422, May 2014.

[118] S. Matsunaga, K. Yamauchi, M. Yamashita, S. Miyahara, "Classification between normal and abnormal respiratory sounds based on maximum likelihood approach," Acoustics, Speech and Signal Processing, pp.19-24, April 2009.

[119] T. Okubo, N. Nakamura, M. Yamashita, S. Matsunaga, "Classification of healthy subjects and patients with pulmonary emphysema using continuous respiratory sounds,"

Engineering in Medicine and Biology Society (EMBC), 36th Annual International Conference of the IEEE, pp.70-73, Aug. 2014.

[120] N. Gavriely, M. Nissan, A. H. E. Rubin, and D. W. Cugell, “Spectral characteristics of chest wall breath sounds in normal subjects,” Thorax vol.50, pp.1292–1300, 1995.

[121] D.O. Rosalba Courtney, “DYSFUNCTIONAL BREATHING: ITS PARAMETERS, MEASUREMENT AND RELEVANCE,” Ph.D. Thesis School of Health Sciences Science, Engineering and Technology Portfolio RMIT University, Feb 2011.

[122] Y. Ramacharaka, “Science of breath: the oriental breathing philosophy” Chicago: Yogi Publication Society; 1904.

[123] R. Nagarathna, H. R. Nagendra, “Yoga for bronchial asthma: A controlled study,” Br Med J. 1985; 291:1077–9.

[124] H. Benson, B. A. Rosener, B. Marzetta, K.M. Klemechu, “Decreased blood pressure in pharmacologically treated. Hypertensive patients who regularly elicited the relaxation response,” Lancet., 1:289-92, 1974.

[125] C. Patel, M.G. Marmot, D. J. Terry, M. Carruther, B. Hunt, S. Patel, “Trial of relaxation in reducing coronary risk: Four-year follow-up,” Br Med J. 290:1103–6, 1985.

[126] L. Pomidori, F. Campigotto, T. M. Amatya, L. Bernardi, A. Cogo, “Efficacy and tolerability of yoga breathing in patients with chronic obstructive pulmonary disease: a pilot study,” J Cardiopulm Rehabil Prev., 29:133–7, 2009.

[127] J Dixhoorn and H. Duivenvoorde "Effect of relaxation therapy on cardiac events after myocardial infarction: a 5-year follow up study." J Cardiopulmonary Rehabilitation 19(3): 178-185, 1999.

[128] J Dixhoorn and H. Duivenvoorde et al. "Physical training and relaxation therapy in cardiac rehabilitation assessed through a composite criterion for training outcome." Am Heart J 118(3): 545-552, 1989.

[129] D. Shannahoff-Khalsa, M. D. Sramek Kennel, S. W. Jamieson "Hemodynamic observations on a yogic breathing technique claimed to help eliminate and prevent heart attacks: a pilot study." J Alternative and Complementary Medicine 10(5): 757-766, 2004.

[130] D.O. Rosalba Courtney, “The functions of breathing and its dysfunctions and their relationship to breathing therapy,” Int. J. Orofacial Myology 12, pp.78-85, 2009.

[131] G. Marks, et al. “Asthma and complementary therapies: a guide for health professionals,” Canberra: National Asthma Council Australia & Australian Department of Health and Ageing; 2005.

[132] G. Z. Yang, “Body Sensor Networks,” London, U.K.: Springer-Verlag, 2006.

[133] J. Feng, S. Megerian, M. Potkonjak, "Model-based calibration for sensor networks," Sensors, 2003. Proceedings of IEEE, vol.2, pp.737- 742, Oct. 2003.

[134] L. Balzano, “Addressing fault and calibration in wireless sensor networks”, Master’s thesis, University of California, Los Angeles, California, 2007.

[135] E. Waltz, “Data fusion for C3I: A tutorial,” in Command, Control, Communications Intelligence (C3I) Handbook. Palo Alto, CA: EW Communications, pp. 217–226, 1986.

[136] J. Llinas and E. Waltz, “Multisensor Data Fusion,” Boston, MA: Artech House, 1990.

[137] D. Hall, “Mathematical Techniques in Multisensor Data Fusion,” Boston, MA: Artech House, 1992.

[138] L. A. Klein, “Sensor and Data Fusion Concepts and Applications,” SPIE Opt. Engineering Press, Tutorial Texts, vol.14, 1993.

[139] D.L. Hall, J. Llinas, "An introduction to multisensor data fusion," Proceedings of the IEEE, vol.85, no.1, pp.6-23, Jan 1997.

[140] T. Clouqueur, K. K. Saluja, and P. Ramanathan, “Fault tolerance in collaborative sensor networks for target detection,” IEEE Trans. Comput., pp. 320–333, March 2004.

[141] Todd K. Moon, Wynn C. Stirling, “Mathematical Methods and Algorithms for Signal Processing”, Aug 1999.

[142] “TP4500”, Available: http://www.temptronic.com/Products/TP4500.htm

[143] M.R. Neuman, H. Watson, et al. “Cardiopulmonary monitoring at home: The CHIME monitor,” Physiol. Meas., 22, 267–286, 2001.

[144] L. G. Lindberg, H. Ugnell, P. A. Oberg, “Monitoring of respiratory and heart rates using a fibre-optic sensor,” Med. Biol. Eng. Comput., 30, 533–537, 1992.

[145] G. B. Moody, R. G. Mark, A. Zoccola, S. Mantero, “Derivation of respiratory signals from multi-lead ECGs,” In Proceedings of the Computers in Cardiology, vol.12, pp.113-116, September 1985.

[146] P. de Chazal, C. Heneghan, E. Sheridan, R. Reilly, P. Nolan, M. O’Malley, “Automated processing of the single-lead electrocardiogram for the detection of obstructive sleep apnoea,” IEEE Trans. Biomed. Eng., 50, 686-696, 2003.

[147] D. Dobrev, I. Daskalov, “Two-electrode telemetric instrument for infant heart rate and apnea monitoring,” Med. Eng. Phys. 20, 729–734, 1998.

[148] G. Matthews, B. Sudduth, M. Burrow, “A noncontact vital signs monitor,” Crit. Rev. Biomed. Eng., 28, 173–178, 2000.

[149] R. Ichapurapu, S. Jain, G. John, T. Monday, D.Y.C. Lie, R. Banister, J. Griswold, "A 2.4 GHz Non-Contact Biosensor System For Continuous Vital-Signs Monitoring," Wireless And Microwave Technology Conference, IEEE 10th Annual, pp1-3, 20-21 April 2009.

[150] A. Hooker, D. J. O’Brien, D. F. Danzl, J. A. Barefoot, and J. E. Brown, “Respiratory rates in emergency department patients,” J. Emerg. Med., vol.7, no.2, pp.129–32, Jan 1989.

[151] STMicroelectronics group of companies, “Tilt measurement using a low-g 3-axis accelerometer”, Application note, Canada, 2010.

[152] O. Banos, “Robust Expert Systems for more Flexible Real-World Activity Recognition”, Ph.D. Thesis, University of Granada, April 2014.

[153] J. Bergmann, V. Chandaria, and A. McGregor, “Wearable and Implantable Sensors: The Patient’s Perspective,” *Sensors*, vol. 12, no.12, pp.16695–16709, Dec. 2012.

[154] Craig L. Scanlan, Albert J. Heuer, “Certified Respiratory Therapist Exam Review Guide”, 2d edition, Sep 2013.

[155] Joseph E. Parrillo, R. Phillip Dellinger, "Critical Care Medicine: Principles of Diagnosis and Management in the Adult" Elsevier Health Sciences, 4th edition, Oct 2013.

[156] G. Strauss-Blasche, M. Moser, M. Voica, D. R. McLeod, N. Klammer, W. Marktl, "Relative timing of inspiration and expiration affects respiratory sinus arrhythmia, " Clin Exp Pharmacol Physiol., vol.27(8), pp.601-606, Aug 2000.

[157] M. Janidarmian, A. Roshan Fekr, K. Radecka, Z. Zilic, "Affordable eRehabilitation Monitoring Platform", IEEE International Humanitarian Technology Conference (IHTC), *014 IEEE Canada International* , pp.1-6, June 2014.

[158] J. Allen, M. Wolfson, K. McDowell, T. Shaffer, "Thoracoabdominal asynchrony in infants with airflow obstruction," Am Rev Respir Dis, 1990.

[159] N. Kiciman, B. Andreásson, G. Bernstein, F. Mannino, W. Rich, C. Henderson, "Thoracoabdominal motion in newborns during ventilation delivered by endotracheal tube or nasal prongs," Pediatr Pulmonol. pp. 175-81, 1998.

[160] E. Agostoni, P. Mognoni, "Deformation of the chest wall during breathing efforts," J Appl Physiol, 21(6):1827-32, 1966.

[161] "Spirometer", Available: http://www.vernier.com/products/sensors/spr-bta/

[162] "Gas Pressure Sensor", Available: http://www.vernier.com/products/sensors/gps-bta/

[163] "Go!Link", Available: http://www.vernier.com/products/interfaces/go-link/

[164] "Respiration Monitor Belt", Available: http://www.vernier.com/products/sensors/rmb/

[165] D. Wallach, B. Goffinet, "Mean squared error of prediction as a criterion for evaluating and comparing system models," Ecological Modelling 44, 299–306, 1989.

[166] R. Priori, A. Aliverti, A. Albuquerque, M. Quaranta, P. Albert, "The effect of posture on asynchronous chest wall movement in COPD," J Appl Physiol, 2013.

[167] R. Gilbert, J. H. Jr. Auchincloss, J. Brodsky, and W. Boden. "Changes in tidal volume, frequency, and ventilation induced by their measurement" J. Appl. Physiol. 33: 252–254, 1972.

[168] S. J. Barbour, C. A. Vandebeek, J. M. Ansermino, "Increased tidal volume variability in children is a better marker of opioid-induced respiratory depression than decreased respiratory rate," J Clin Monit Comput., 18:171–8, 2004.

[169] J. Mark Ansermino, Kirk Shelley, "When Monitoring Analgesia in Pediatric Patients Tidal Volume Variability Can Predict Respiratory Depression" annual meeting of the Society for Technology in Anesthesia and interviews, vol. 30:09, 2004.

[170] N. Hart, M. I. Polkey, A. Clement, M. Boule, J. Moxham, F. Lofaso, B. Fauroux, "Changes in pulmonary mechanics with increasing disease severity in children and young adults with cystic fibrosis," Am J Respir Crit Care Med, pp-61–66, 2002.

[171] J. Lin, E. Keogh, S. Lonardi, and B. Chiu. "A Symbolic Representation of Time Series, with Implications for Streaming Algorithms," In proceedings of the 8th ACM SIGMOD Workshop on Research Issues in Data Mining and Knowledge Discovery, pp.2-11, June 2003.

[172] E. Keogh, J. Lin, A. Fu, “HOT SAX: efficiently finding the most unusual time series subsequence,” In: Proceedings of the Fifth IEEE International Conference on Data Mining, pp. 226–233, 2005.

[173] J. Gama, “Knowledge Discovery from Data Streams” CRC Press, Boca Raton (2010).

[174] A. Apostolico, M.E. Bock, and S. Lonardi, “Monotony of Surprise and Large-Scale Quest for Unusual Words” In proceedings of the 6th Int’l Conference on Research in Computational Molecular Biology, pp.22-31, April 18-21.

[175] Y. Huang, P. S. Yu, “Adaptive Query Processing for Time- Series Data” In proceedings of the 5th Int'l Conference on Knowledge Discovery and Data Mining, pp.282-286, Aug 15-18.

[176] R. J. Larsen, and M. L. Marx, “An Introduction to Mathematical Statistics and Its Applications” Prentice Hall, Englewood, Cliffs, N.J. 2nd Edition.

[177] Statistical Tests in Medical Research, Jacques Jamar t, book, 1992.

[178] Noam Gavriely, “Breath Sounds Methodology,” CRC Press: Florida, 1995.

[179] “mHealth Market Analysis And Segment Forecasts To 2020,” Grand View Research, ISBN Code: 978-1-68038-076-7, Feb. 2014.

[180] Susan Rovezzi Carroll, David J. Carroll, “Statistics Made Simple for School Leaders” Rowman & Littlefield, December 2002.

[181] “Windows Azure.” [Online]. Available: http://www.windowsazure.com/en- us/

[182] E. Keogh, P. Smyth, “A Probabilistic Approach to Fast Pattern Matching in Time Series Databases,” In Proceedings of the 3rd International Conference on Knowledge Discovery and Data Mining, pp. 20–24, August 1997.

[183] S.M. Pincus, “Approximate entropy as a measure of system complexity,” Proceedings of the National Academy of Sciences of the United States of America, 88(6):2297–301, 1991.

[184] W. Chen, J. Zhuang, W. Yu, Z. Wang, “Measuring complexity using FuzzyEn, ApEn, and SampEn,” Medical Engineering & Physics, vol.31, no.1, pp.61-68 , 2009.

[185] J. M. Yentes, N. Hunt, K. K. Schmid, J. P. Kaipust, D. McGrath, N. Stergiou, “The appropriate use of approximate entropy and sample entropy with short data sets,” Annals of biomedical engineering, 41:349–365, 2013.

[186] M. Dash, H. Liu, “Feature Selection for Classification,” Intelligent Data Analysis 1, pp.131–156, 1997.

[187] J. C. Schlimmer, “Efficiently inducing determinations: A complete and systematic search algorithm that uses optimal pruning,” In: Proceedings of Tenth International Conference on Machine Learning, pp.284–290, 1993.

[188] O. Chapelle, P. Haffner, and V. N. Vapnik, “Support vector machines for histogram-based classification,” IEEE Trans. Neural Netw., vol. 10, no.5, pp.1055–1064, Sep. 1999.

[189] F.F. Chamasemani, Y.P. Singh, "Multi-class Support Vector Machine (SVM) Classifiers --An Application in Hypothyroid Detection and Classification," Bio-Inspired Computing: Theories and Applications, Sixth International Conference on, pp.351-356, 2011.

[190] L. Bao, S.S. Intille, “Activity recognition from user-annotated acceleration data,” Pervasive Comput., vol.23, pp.1–17, 2004.
[191] N. Ravi, P. Mysore, M. L. Littman, “Activity recognition from accelerometer data,” In Proceedings of the 17th Conference on Innovative Applications of Artificial Intelligence, pp.1541–1546, 2005.
[192] N. Kern, B. Schiele, A. Schmidt, “Multi-sensor activity context detection for wearable computing,” In Proceedings of the European Symposium on Ambient Intelligence, pp.220–232, Nov. 2003.
[193] M. Hall, “Correlation-based feature selection for machine learning,” PhD Thesis., Department of Computer Science, Waikato University, New Zealand, 1999.
[194] J. Abellán and A. R. Masegosa, “Bagging decision trees on data sets with classification noise,” in Proc. 6th Int. Conf. Found. Inf. Knowl. Syst., pp. 248–265, Feb. 2010.
[195] Kateryna Kon, “Discriminant analysis,” BIOMEDICSL STATISTICS, Methods of prognosis, 2015.
[196] M. Akhil jabbar, B. L Deekshatulu, P. Chandra, “Classification of Heart Disease Using K- Nearest Neighbor and Genetic Algorithm,” International Conference on Computational Intelligence: Modeling Techniques and Applications (CIMTA), pp.85- 94, 2013.
[197] T. G. Dietterich and G. Bakiri, “Solving multiclass learning problem via error-correcting output codes,” Journal of Artificial Intelligence Research, pp. 263–286, 1995.
[198] Y. Liu, “Using SVM and error-correcting codes for multiclass dialog act classification in meeting corpus,” in Proc. Interspeech-ICSLP, pp.1938-1941, Sep. 2006.
[199] Y. K. Irfan, P. H. Zope, and S. R. Suralkar, “Importance of Artificial Neural Network in Medical Diagnosis disease like acute nephritis disease and heart disease,” International Journal of Engineering Science and Innovative Technology (IJESIT), vol.2(2), pp.210-217, 2013.
[200] K. Kumar and B. Abhishek, “Artificial Neural Networks for Diagnosis of Kidney stone Disease”, I.J. Information technology and computer science, vol.7, pp. 20-25, July 2012.
[201] J. C. Fernandez, F. J. Martinez, C. Hervas, P. A. Gutierrez, "Sensitivity Versus Accuracy in Multiclass Problems Using Memetic Pareto Evolutionary Neural Networks," Neural Networks, IEEE Transactions on, vol.21, no.5, pp.750-770, May 2010.
[202] Deb, Kalyanmoy. Multi-Objective Optimization Using Evolutionary Algorithms. John Wiley & Sons, 2001.
[203] S. Arlot, A. Celisse, “A survey of cross-validation procedures for model selection,” Stat. Surv., vol.4, pp.40–79, 2010.
[204] R. Kohavi, “A study of cross-validation and bootstrap for accuracy estimation and model selection,” In Proceedings of the 14th International Joint Conference on Artificial Intelligence (IJCAI’95), vol.2, pp.1137-1143, 1995.
[205] M. Thomas, R. K. McKinley, E. Freeman, C. Foy, “Prevalence of dysfunctional breathing in patients treated for asthma in primary care: cross sectional survey,” BMJ, 322:1098–100, 2001.

[206] J. V. Dixhoorn, “Whole-Body breathing: a systems perspective on respiratory retraining,” Principles and practice of stress management. P. M. Lehrer, R. L. Woolfolk and W. E. Sime. New York, Guilford Press: 291-332, 2007.

[207] D.O. Rosalba Courtney, “Strengths, Weaknesses, and Possibilities of the Buteyko Breathing Method,” AAPB Journal, pp.59-63, 2008.

[208] D. H. Johnson, “Breath, Bone and Gesture”. San Francisco, North Atlantic Books, 1995.

[209] R. Ley, "The modification of breathing behavior. Pavlovian and operant control in emotion and cognition," Behav Modif 23(3): 441-479, 1999.

[210] S. G. Mijares, “The Revelation of the Breath: a tribute to its wisdom, power and beauty,” Albany, State University of New York Press, 2009.

[211] I. Mahmood, "Speech Recognition using Dynamic Time Warping," IEEE International Conference on Advances in Space Technologies, pp.74-79, 2008.

[212] Xiaoyu Xu, “Large Scale Human Activity Monitoring for Diverse Subjects,” Ph.D. Thesis in Electrical Engineering, UNIVERSITY OF CALIFORNIA, 2013.

[213] M. Muller, “Information Retrieval for Music and Motio”, book series Database Management & Information Retrieval, Springer publisher, XVI, 318 p, 2007.

[214] K. H. Chang, M. Y. Chen, and J. Canny, “Tracking free-weight exercises” Proceedings of the 9th international conference on Ubiquitous computing, UbiComp ’07, pp.19–37, 2007.

[215] S. Khalsa, "Treatment of insommnia with yoga: a preliminary study with sleep-wake diaries." Applied Psychophysiology and Biofeedback 29(4): 269-278, 2004.

[216] L. Spicuzza, A. Gabutti, C. Porta, N. Montano, L. Bernardi "Yoga and chemoreflex response to hypoxia and hypercapnia." The Lancet 356(9240): 1495-1496, 2000.

[217] K. R. Murthy, B. K. Sahaj, P. Silaramaraju, "Effect of pranayama (rechaka, puraka & khumbaka) on bronchial asthma-an open study." Lung India 5: 187-191, 1983.

[218] R. N. Nagarathna, "Yoga for Bronchial Asthma: a controlled study." British Medical Journal 291: 1077-1079, 1985.

[219] V. Singh, A. Wisniewski, J. Britton, A. Tattersfield, "Effect of yoga breathing exercises (pranayama) on airway reactivity in subjects with asthma." The Lancet 335: 1381-1383, 1990.

[220] P. Vedanthan, N. Lakshmyya, B. Kesavalu, M. Murthy, "Clinical Study of Yoga Techniques in University Students with Asthma: A control study." Allergy and Asthma Proc. 19(1): 3-9, 1998.

[221] R. Monroe, J. Power, A. kumar, R. Nagarathna, P. Dandona, "Yoga therapy for NIDDM; a controlled trial." Journal of Complementary Medicine 6(2): 66-68, 1992.

[222] N. Janakiramaiah, B. N. Gangadhar, P. J. Naga Venkatesha Murthy, M. G. Harish, D. K. Subbakrishna, A. Vedamurthachar, "Therapeutic Efficacy of Sudarshan Kriya Yoga (SKY) in Dysthmic Disorder." Nimhans Journal (January): 21-28, 1998.

[223] P. J.Murthy, N. Janakiramaiah, B. N. Gangadhar, D. K. Subbakrishna, "P300 amplitude & antidepressant response to Sudarshan Kriya Yoga (SKY)." Journal of Affective Disorders 50: 45-48, 1998.

[224] A. Vedamurthachar, N. Janakiramaiah, J. M. Hegde, T. K. Shetty, D. K. Subbakrishna, S. V. Sureshbabu, B. N. Gangadhar, "Antidepressant efficacy and hormonal effects of Sudarshana Kriya Yoga (SKY) in alcohol dependent individuals." J Affect Disord 94(1-3): 249-253, 2006.

[225] A. Bruton, G. T. Lewith, "The Buteyko breathing technique for asthma: a review", Complement Ther Med, 13:41–6, 2005.